The Dissertation Committee for Kenan Isik

certifies that this is the approved version of the following dissertation:

# Performance and Manufacturing Considerations for Series Elastic Actuators

Committee:

Luis Sentis, Supervisor

Benito R. Fernandez

Dongmei Chen

Ronald Barr

Aloysius K. Mok

# Performance and Manufacturing Considerations for Series Elastic Actuators

by

**Kenan Isik, B.M.E.; M.S.**

**Dissertation**

Presented to the Faculty of the Graduate School of

The University of Texas at Austin

in Partial Fulfillment

of the Requirements

for the Degree of

**Doctor of Philosophy**

**The University of Texas at Austin**

May 2017

Dedicated to my caring parents, loving wife, and cheerful daughter.

# Acknowledgments

A good friend of mine once told me that doing a PhD is like being left in the middle of the ocean and then trying to find the shores. I did not reflect deeply on this sentence back then when I was a first year PhD student. As the years passed by, I came to understand the true meaning of it. It is hard for anyone to survive this challenge, and finding the shores is definitely not a one-person job. One needs guidance to figure out the right direction. With this point of view, I would like to express my gratitude to my advisor Dr. Luis Sentis for his tremendous support in my academic endeavors and personal development as a researcher. His never-ending energy and enthusiasm on coaching us to ask the right questions on our research and guiding us to formalize and solve those questions will be a life-long inspiration during my future academic life. I would like to thank also to the members of my dissertation committee: Dr. Benito Fernandez, Dr. Dongmei Chen, Dr. Ronald Barr and Dr. Aloysius Mok for their time and support in the development and improvement of my research and this dissertation. Their advice and support in finding solutions to the difficulties in my research have been invaluable.

Just like any other journey, the journey of doctoral education requires many resources, both financially and intellectually. I would like to share my

appreciation to the Ministry of National Education of the Republic of Turkey and The University of Texas at Austin for their financial support, intellectual contribution and resourceful facilities that I have enjoyed throughout my PhD life. I would like to also thank Joseph Ho from PI Electronics Ltd. for his financial and intellectual support on my low-cost series elastic actuator design project, Shunde He for his great contribution on the development of this actuator and Dr. Aloysius Mok for initiating this collaborative work.

Whether to pursue a PhD education or not is a life changing decision. I would like thank my beloved father Fahri Isik, and my uncle Macit Isik who have always believed in me, and who encouraged me to follow my desire to learn more and to contribute to science and education while everyone else was focusing on the hardship of this endeavor. There are no words to express my gratitude to my beloved mother Zeliha Isik, who has always respected and supported my life decisions unconditionally. I have always felt her love and have heard her prayers for my well-being, even as I was thousands of miles away from her for many years.

My most important companion, my beloved wife Sueda Isik joined me during my journey and supported me from the first day we met in the best possible way I could ever ask for. Her company gave me the strength to work hard and motivated me to push forward on this journey. She gave me the most beautiful gift in my life, my daughter Zeliha Sare Isik, who has been the greatest joy in our lives ever since we have had her.

I would like to thank to Nicholas Paine, who has provided me with great support in my research directions, in hardware implementations of my research and in PhD life in general. His suggestions helped me avoid many pitfalls in my research.

I consider myself very lucky to have had the opportunity to work in such a great research laboratory with wonderful colleagues. I would like to thank Kwan Suk Kim and Donghyun Kim who have been an important resource of knowledge and inspiration. I have always appreciated their patient help with my software-related questions, especially on using Linux. Ye Zhao has been and will be a model for me of hard work and productivity. His input to my research has always been helpful in sparkling new ideas. Chien-Liang Fok has been a constant source of new ideas on creating methodologies on analyzing the research problems and solving them. His organized research skills will always be a frame of reference during my future research.

I had the privilege of working closely with two great researchers in my laboratory, Rachel Schlossman and Gray C. Thomas. I have always enjoyed our long meetings with inspiring conversations. With her keen attitude on our research and with his boldness in tackling the hardest problems, Rachel and Gray has been important sources of motivation for me.

I am grateful to my colleagues Rachel Schlossman, Gray C. Thomas and Steven J. Jorgensen for their help on improving the quality of this dissertation with their valuable suggestions and revisions.

Binghan He, Mike Slovich, Dr. Seung Kyu Park, Alan Kwok, Pius Wong, Travis Llado, Dorothy Lua Jorgensen, Joshua James, Gwen Johnson, Cory Crean, Kunye Chen, Orion Campbell, Minkyu Kim, Junhyeok Ahn, Jaemin Lee, Jake Hall, Tunc Akbas and many more friends have made my PhD life enjoyable and memorable. I would like to thank all of them for their friendship. As I look toward the shores, where my PhD journey ends, I am both excited and saddened at the same time. I am excited to start my academic life as a professional but saddened to leave such a great research

atmosphere and good friends behind.

Kenan Isik

*The University of Texas at Austin*

*May 2017*

# Performance and Manufacturing Considerations for Series Elastic Actuators

Publication No. _____

Kenan Isik, Ph.D.
The University of Texas at Austin, 2017

Supervisor: Luis Sentis

Robots are becoming an integral part of our lives. We are already physically connected with them through many robotic applications such as exoskeletons in military, orthosis devices in health care, collaborative robots in industry, etc. While the integration of robots improves the quality of human life, it still poses a safety concern during the physical human-robot interaction. Series Elastic Actuators (SEAs) play an important role in improving the safety of human-robot interaction and collaboration. Considering the fast expansion of robotic applications in our lives and the safety benefits of SEAs, it is conceivable that SEAs are going to play an important role in robotic applications in every aspect

of human life. This dissertation focuses on reducing the cost, simplifying the use and improving the performance of SEAs.

The first research focus in this dissertation is to reduce the cost of SEAs. Robots are successful in reducing production and service costs when used but the capital cost of robot installations are very high. As robotics research shifts to safe robotic applications, reducing the cost of SEAs will greatly help to deploy this technology in more robotic applications and to increase their accessibility to a broader range of researchers and educators. With this motivation, I present a case study on reducing the cost of a SEA while maintaining high force and position control performance and industrial grade service life.

The second research focus in this dissertation is to simplify the laborious gain selection process of the cascaded controllers of SEAs. In order to simplify the gain selection process of the impedance controllers of SEAs, an optimal feedback gain selection methodology was developed. Using this method, the feedback gains of the cascaded PD-type impedance controllers of SEAs can easily be calibrated. The developed method allows the users to find the highest feedback gains for a desired phase-margin.

Beyond the low-cost realization and simple controller tuning of SEAs, performance improvements on SEAs are possible utilizing the series elasticity in these actuators. As the third research focus in this dissertation, a sequential convex optimization-based motion planning technique is developed in order to improve the joint velocity capabilities of SEAs with nonlinearities. By using this method, higher joint velocities, that are not achievable with the rigid counterparts of SEAs can be achieved.

# Contents

# List of Tables

# List of Figures

# Chapter 1

# Introduction

## 1.1 Motivation and Goals

We, as humans, have a long history of using the objects around us and developing techniques and technologies in order to ease our struggle against nature and to improve the quality of our life. Throughout history, there have been disruptive developments in technology such as the printing press, the industrial revolution, semiconductors, the development of computers, etc. As we go through the era of information technologies and see its major effects on the socioeconomic life around the globe, another big change in our lives is slowly happening by the development of safe and smart robots. We already use robotic systems for augmenting human capabilities, healing stroke patients, educating students, entertaining crowds and many more applications. However, the integration of the robots into our lives is nowhere near complete.

Robots are becoming an important part of human life through physical

human-robot interaction (pHRI) based applications. Even though many applications involving human-robot interaction have already been developed, close collaborations between the human and robots have not been achieved due to safety concerns. Safety is a critical consideration in pHRI and therefore, it is becoming a key design requirement for collaborative robots and automation systems. Conventional robots mainly rely on force and position control with stiff joints. Rigid actuators play an important role in industrial applications. However, as robots spread into every aspect of our lives, rigid robots with stiff joints will need to be replaced with safe and smart robots. We can create an analogy between robots and cars: Using robots without series elasticity is similar to using cars without suspensions. Now it is time to add "suspension" to robots to make them safer and more reliable.

### 1.1.1 Series Elastic Actuation

There are multiple ways of improving the safety of human-robot interaction such as designing safe robotics hardware, developing collision avoidance methods, collision detection algorithms, and reaction methods in case a collision occurs. Series elastic actuators (SEAs) (G. A. Pratt & Williamson (1995)) play a key role in preparing safe robotics hardware while contributing to the development of collision detection methods. SEAs are new type of actuators which have an intentional elasticity between the load and actuation system. Figure 1.1 shows a simplified model of a SEA.

In typical industrial manipulators, there is the traditional premise that

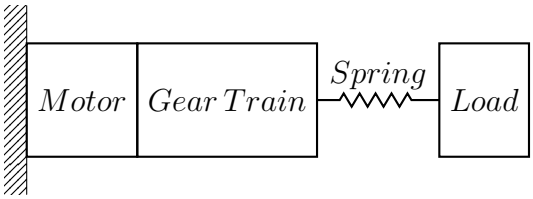


Figure 1.1: Simplified model of a typical SEA.

the stiffer the mechanical interface between the actuator and the load, the better which was contended by (G. A. Pratt & Williamson (1995)). Although this premise has made industrial robots hugely successful due to their position control performance, it leads to humans and robots being physically separated as a safety precaution. Stiff actuators are best suited for position control applications where the robot environment is almost perfectly known. On the other hand, environments where humans work are dynamic and unstructured and therefore, require the use of force sensing and control techniques for safe pHRI. SEAs have several key benefits such as reducing the effect of the reflected inertia, higher tolerance to impact loads, passive mechanical energy storage, low mechanical output impedance, and increased peak power output (G. A. Pratt & Williamson (1995); Arumugom et al. (2009); Paluska & Herr (2006b)).

Safety is only one example of the many benefits that series elastic actuation provide. Another major impact of SEAs on robotics is in legged locomotion. Two major performance improvements have been achieved by using SEAs. The first major benefit of using SEAs on robot legs is energy efficiency. SEAs store and release mechanical energy during locomotion. Using this energy during the cyclic motion of the robot locomotion reduces the en-

ergy consumption and improves the energy efficiency of the robot locomotion. The second major benefit comes from SEAs' capability of reducing the effects of impacts which occur when the robot leg contacts the ground. SEAs add robustness to robot locomotion by softening the contacts.

Reliable force feedback is another important property of SEAs. Along with low impedance interface, force feedback reliability of SEAs made a great impact on rehabilitation robotics. Post-stroke rehabilitation of patients is being done by using robot exoskeletons for legs, arms, fingers, etc. SEA-based exoskeletons are also being used in industry and military for augmenting physical human capabilities such as carrying heavy loads, walking and running longer distances, muscle fatigue prevention, etc.

The list of current applications of SEA-based robots as well as their possible applications in the future can be extended with many more examples. As this technology matures, their use in our daily life will be prevalent in many aspects from education to entertainment, from service robotics to smart house applications, from health care to transportation, etc. Figure 1.2 shows examples of SEA-based applications from aforementioned areas.

Even though series elastic actuation has many benefits, cost is a significant drawback of SEAs. Although the main idea is simply adding an elastic element between the load and the actuation mechanism, this modification adds complexity to the mechanical designs of the actuator as well as to the design of controllers.

Cost is an important consideration when transferring a technology from

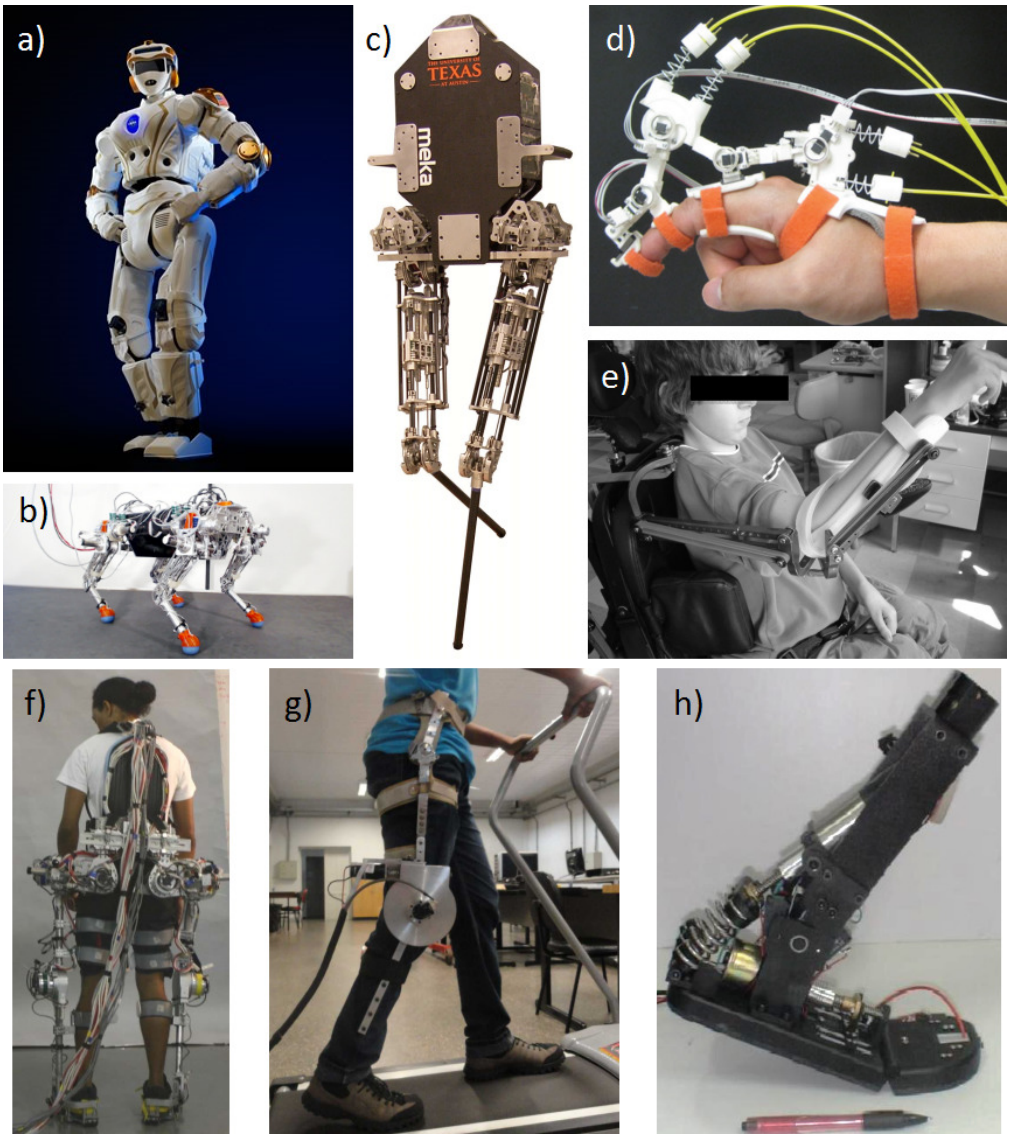


Figure 1.2: Examples of SEA-based robotic applications. a) Valkyrie of NASA-JSC (Kisliuk (2015)), b) StarlETH (Hutter (2013)), c) Hume (Slovich et al. (2012)), d) Finger exoskeleton for rehabilitation (Agarwal et al. (2015)), e) Orthosis-based arm exoskeleton (Ragonesi et al. (2011)), f) Exoskeleton for strength augmentation (Kwa et al. (2009)), g) Knee orthosis for rehabilitation (dos Santos et al. (2013)), h) PANTOE 1 for ankle-foot prosthesis (Zhu et al. (2010)).

research laboratories to daily use of masses. Robotics, in general, is an expensive area of research. The multidisciplinary nature of robotic applications requires detailed work on system integration and careful design for performance and safety. Even though the utilization of robots in manufacturing and other areas greatly help to reduce the production and service costs, the capital cost of robot installation is an important obstacle.

The design of these safe robotics hardware and human-centered safe collaboration methods are still under development. Reducing the cost of SEAs, and mechatronic hardware in general, for low-volume production is crucial for increasing the availability of these hardware for research and educational institutions. The increased availability of robotic research hardware will boost the development of safe and smart robots and therefore, greatly contribute to improving the quality of human life.

### 1.1.2 Control of Human-Robot Interaction

Another major drawback of SEAs is the reduced impedance and position control bandwidth. Rigid actuators have high position control bandwidth which makes them very successful on position control tasks that require precise positioning of the end effector. On the other hand, the passive elastic element on SEAs limits the position control capability of SEAs and reduces the range of impedance that they can render.

Impedance control is a widely used control approach which regulates the dynamic interaction between the robot and the environment (Hogan (1985)).

In this control approach, instead of the force or the position of the interaction port, the relationship between the force and velocity of the output is controlled. More information about impedance control is provided in Section 2.2.

As mentioned previously, simply adding an elastic element between the load and the actuation mechanism increases not only the complexity of the mechanical hardware but also the complexity of controllers of these actuators. The order of the system model, obviously, increases with the added spring. Therefore, designing controllers and tuning feedback gains for these actuators require more effort than for the rigid actuators. Proportional-derivative (PD) control is one of the most common control types for impedance control of SEAs. Feedback gain selection for PD-type controllers for first and second order systems is well established and straightforward. However, when the order of the system becomes three or more, the effect of proportional and derivative gains becomes less intuitive and the system output behavior is harder to predict for gain changes. Therefore, empirical tuning of the feedback gains for the high order systems requires laborious work. This hard work becomes even harder when the desired output is a function of frequency. Gain tuning for position output of a system is much easier than gain tuning for position or impedance control bandwidth.

There exists a counter-intuitive relationship between the inner force and outer impedance control loops of SEAs with time-delay and derivative filters. Following the common practice and tuning the feedback gains of inner force control loop for a high bandwidth drastically affects the range of stable

feedback gains of outer impedance controller. It becomes necessary to reduce the force controller's feedback gains in order to stably increase the impedance control bandwidth. This phenomenon was observed during the controller development for StoneAge-SEA (Isik et al. (2017)) and it was also reported by other researchers in the literature (Focchi et al. (2016)). Although a feedback gain selection for the fourth order impedance controllers of SEAs was proposed (Zhao et al. (2014)), an optimal feedback gain selection method for the impedance controllers which considers the aforementioned phenomenon and maximizes the impedance control bandwidth has not been established in the literature. In order to simplify the gain selection process and to maximize the bandwidth of the impedance controllers of SEAs, an intuitive gain selection methodology needs to be developed.

### 1.1.3 Performance Enhancements for Series Elastic Actuators

Beyond pushing the limits of low-level controllers of SEAs, the task-level capabilities of SEAs have promising characteristics to be explored. Currently, SEAs use conventional control methods to control the force and position of the actuator output. The boundaries of actuator capabilities are calculated using the static properties of the system components. This approach bounds the maximum output force and velocity of SEAs to the maximum torque and velocity of the motors and to the efficiency limitations of drivetrain components. SEAs have the capability of storing mechanical energy in the series elastic

element. This property is being used for increasing the energy efficiency of walking robots by passively storing and releasing energy. While most of the current applications use the energy storage capability of SEA in an uncontrolled manner, it is possible to release the stored energy at a desired time and output position. This can be done by optimizing the desired position and velocity profile of the actuator. By doing so, the task-level capabilities of SEAs can be further improved. Optimization for SEA performance enhancement is scarcely explored in the literature and these studies are presented in Section 2.3. These studies mostly focus on optimizing a hardware parameter of SEAs or variable stiffness actuators (VSAs) such as the stiffness of the elastic element. On control aspects, joint velocity enhancement studies focus on switching times for bang-bang type of controllers. The trajectory optimization studies for increasing the joint velocity are limited on scalability due to their customization to a specific hardware type. Considering these limitations, I propose a new method to improve the joint velocity performance of SEA-based single-DOF and multi-DOF actuators.

### 1.1.4 The Goal

By studying the aforementioned shortcomings and advantages of SEAs, it is possible to contribute to the development of safe and smart robotic applications. My goal in this dissertation is to explore and devise methods to reduce the cost and improve the performance and capabilities of SEAs. By doing so, I aim to contribute to the robotics community and future safe robot users by

increasing the availability of SEAs and simplify their use. A summary of the research goals of this dissertation is as follows:

- Raise awareness in academia of the possibility of the low-cost realization of low-volume research and education SEAs without (or with minimal) compromise on the control performance. By doing so, I aim to contribute to the availability of this hardware to a broader range of users.

- Simplify the tedious gain selection process for the PD-based impedance controllers of SEAs with cascaded architectures while maintaining a desired system behavior. My goal in developing a gain selection method is to explore the upper limits of impedance gains and to improve the position/impedance control bandwidth of SEAs.

- Exploring the possible improvements on the task-level control capabilities of SEAs by exploiting their passive energy storage property. By designing optimal trajectories, I aim to achieve joint velocities which are impossible to reach using these actuators' rigid counterparts.

## 1.2 Approach and Contribution

### 1.2.1 A Case Study on Reducing the Cost

Hardware design is an iterative process. In order to match the desired physical properties, to reduce the cost and to improve the control performance, multiple changes in the design and component selection have to be done during the

hardware design process. Due to possible unforeseeable hardware and software integration issues, simply doing custom part designs and finding low-cost off-the-shelf components would not give a reliable result on low-cost hardware design. Therefore, the best method to prove the possibility of low-cost realization of a mechatronic hardware is building the actual hardware and performing performance analysis on it. Having this in mind, I performed a case study on reducing the cost of a SEA.

There are multiple ways of reducing the cost of a piece of mechatronic hardware. Some of these methods can be categorized as follows:

- Mechanical Design: Increasing the number of off-the-shelf parts, designing custom parts for easy manufacturability, designing the mechanical hardware by starting with the component which has the highest potential to contribute to the cost reduction, and selecting low-cost components even with undesired properties if there are solutions available to overcome their shortcomings.

- Purchasing and Machining: Finding the lowest quote for the selected components and taking advantage of globalization of trade around the world. Machining costs can be reduced drastically by off-shoring production.

- Control Methods: Overcoming some of the shortcomings of the low-cost components using controller design methods. For example, designing a nonlinear controller instead of looking for a high-cost perfectly lin-

ear springs, or designing a position-based torque controller for low-cost motors with high torque ripples.

There are other methods of cost reduction which can be applied to high-volume production of a piece of hardware, but these are out of the scope of this dissertation.

For the design and manufacturing of the low-cost SEA, we partnered with an industrial company in China. I had the opportunity to go to the Shenzen region in China to work closely with experienced engineers during my design process and to take advantage of the low-cost labor and production habitat of this area. By reducing the number of custom parts, increasing the number of off-the-shelf components, and exploiting the low-cost labor and off-the-shelf component opportunities in Shenzhen, I was able to reduce the manufacturing cost to one-third of the reference SEA, the UT-SEA (Paine et al. (2014)) and build the low cost SEA, the SA-SEA (Isik et al. (2017)) shown in Figure 1.3. Considering the possibility of non-ideal characteristics in the low-cost components, I performed characterization and control methods to overcome the shortcomings of the low-cost components.

The importance of this project is that the design process was performed with performance in mind. As it will be shown in the literature review in Chapter 2, the low-cost mechatronic hardware designs are made by having "low-cost" as the sole design goal. The achieved performance is reported as an uncontrolled output of the study. Control performance as a high priority design goal is missing in the literature for low-cost hardware design studies.

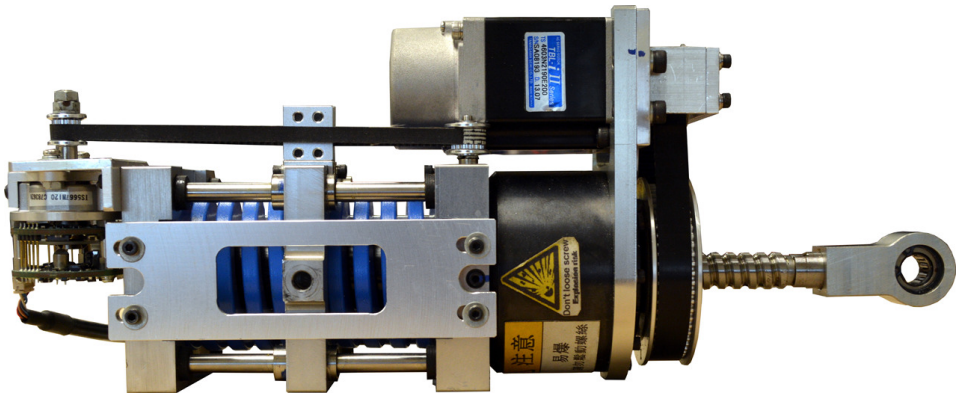

Figure 1.3: The low-cost SEA, StoneAge-SEA.

### 1.2.2 A Search-Based Gain Selection

During the development of force and impedance controllers for the low-cost SEA, I observed that there is a counter-intuitive relationship between the inner control loop (force) and the outer control loop (impedance). It is a common practice to tune the feedback gains of the inner control loop targeting a high control bandwidth and then tuning the feedback gains of the outer loop by assuming that the inner loop behaves like an ideal component in the outer control loop structure. I observed that when working on the outer control loop after the tuning of the inner loop, it is necessary to reduce the inner control loop's feedback gains in order to achieve a high control bandwidth for the outer impedance controller. A search in the literature revealed that this phenomenon has been observed by other researchers and has been reported in the literature (Focchi et al. (2016); Zhao et al. (2014)). Nevertheless, a complete solution for feedback gain selection of impedance controllers which incorporates the possible advantage of independent gain scaling for inner and

outer loops has not been developed.

The aforementioned relationship between the inner and outer loops of the impedance controller raises two questions: Firstly, if reducing the feedback gains of inner force controller increases the stability of the overall system and allows to increase the feedback gains of outer loop, is there an ideal set of inner and outer feedback gains which gives the highest impedance phase-margin? More importantly, for a desired phase-margin, what are the highest feedback gains for the inner and outer control loops which would give the highest bandwidth for the impedance controller?

I decided to find the ideal set of inner and outer controller feedback gains by developing a search-based algorithm. However, there are multiple parameters affecting the phase-margin of the impedance controller (at least four, namely inner and outer damping and stiffness gains) and therefore, the search algorithm would be computationally heavy. Also, it is necessary to select a certain stability criterion because one can increase the feedback gains arbitrarily if the stability level is not a concern. I used the phase-margin stability criterion as a measure of stability and critically damped system output as the desired system behavior and developed an algorithm which automatically calculates the highest stable gains for the desired phase-margin while maintaining a critically damped impedance controller behavior. The proposed methodology significantly reduces the time and effort spent on empirically tuning the force and impedance controller feedback gains. It also allows the user to have more control over the overall system behavior.

### 1.2.3 Optimal Motion Planning for Improving Joint Velocity

The fundamental difference between SEAs and rigid actuators is the elastic element between the load and the actuation mechanism. Some of the most important benefits of this elastic element are the elimination of reflected inertia of the rotor of the electrical motors, low impedance actuator interface capabilities and reliable force feedback. These properties are utilized by the fundamental control approaches such as Proportional-Integral-Derivative (PID) based force, position and impedance controllers, optimal controllers, robust controllers, etc. The passive energy storage capability of SEAs has promising performance extensions by utilizing the stored energy in the elastic element and achieving higher joint velocities. The research on improving the joint agility of SEA in the literature are scarce and either focus on optimizing one parameter of the actuator/controller or on utilizing different types of controllers which are applicable to certain types of SEA designs. In this dissertation, we utilize a sequential convex optimization-based motion planning algorithm for SEAs with nonlinear system properties in order to create optimal trajectories which allow the actuator joint velocities to reach states in state-space that are not accessible for rigid actuators with the same source of power. This approach is advantageous to improve the agility of SEAs because the optimization is done on the spring deflection and joint trajectory which does not require hardware changes. Also, since it is possible to achieve higher instantaneous power output values, the mechanical designs targeting high instantaneous power outputs

can be realized by utilizing smaller motors which contributes to reduction of the hardware cost. The advantage of using sequential convex optimization is that it can be implemented in the low-level embedded controllers and it can be used both for single and multi-DOF system with nonlinearities. Another important benefit of using sequential convex optimization on this problem is that the output of the optimization process is the desired control input which can be controlled with any desired control approach.

For this study, I used the physical properties of the P170 Orion SEA from Apptronik Systems Inc., and maximized the joint velocity by considering the physical limitations of the real hardware such as maximum spring deflection, maximum motor current, etc. This performance improvement reduces the necessary maximum motor torque for a given joint task which requires instantaneous burst of power on the joint. The maximum motor torque is usually proportional to the cost of the motors. Utilizing sequential convex optimization-based motion planning can greatly improve the joint velocity performance of SEAs and reduce the cost of future actuator designs if considered during the mechanical design process. With this point of view, this achievement contributes to my goal of reducing the manufacturing costs of SEAs.

## 1.3 Dissertation Outline

In Chapter 2, a comprehensive literature review is provided on the different designs of SEAs from a cost perspective, on controller designs with the focus

on impedance controllers and gain selection methods and on the state of the art methodologies for expanding the capabilities of SEAs. In Chapter 3, the low-cost mechanical design, simple controller development and performance analysis of the SA-SEA is provided in detail. A simple safety check method was proposed in this section which distinguishes physical user interactions from undesired impacts. In Chapter 4, a simple methodology for optimal gain selection for the PD-type cascaded impedance controllers of SEAs with time-delay and derivative filtering was provided. This method significantly reduces the time and effort spent on gain tuning of cascaded PD-type impedance controllers. Chapter 5 presents the performance improvements achieved by utilizing sequential convex optimization-based motion planning algorithm. This study was performed in the MATLAB environment and simulation results showing the proof of concept are included. Finally, in Chapter 6, conclusions on the studies of this dissertation are given and possible improvements are offered as the future work.

# Chapter 2

# Literature Review

Series elastic actuation is a relatively new type of actuation method with many advantages and some shortcomings. There has been massive research on the mechanical design and control of SEAs. Many researches created new SEA-based designs and applications exploiting the advantages of SEAs and further improving the capabilities of them. The shortcomings of SEAs forced researchers to explore hardware and control design space to overcome some of those shortcomings. In the following sections of this chapter, a literature review on the different mechanical designs (Section 2.1), control approaches (Section 2.2) and performance improvement methods (Section 2.3) are provided. The literature review on the design of SEAs mainly focuses on the cost aspect. The wide range of control approaches is given with a focus on cascaded impedance control and feedback gain selection methods for this type of controllers. Compared to mechanical design and control approaches of SEAs, performance enhancement studies in the literature are scarce. Recent publi-

cations on joint power and velocity enhancement studies are presented. The focus on the literature review of performance enhancement of SEAs is on exploiting the passive energy storage capability of SEAs.

## 2.1 Series Elastic Actuator Designs

SEA hardware typically consists of three main components: an electric, hydraulic or pneumatic motor to deliver mechanical power, a drivetrain to amplify the motor torque, and an elastic element for both sensing the output force and providing passive compliance to the output. The majority of the SEA designs in the literature are alterations and enhancements of these three components for the desired applications. Besides these main components, additional components such as clutches, dampers, etc. have been used in order to expand the design space, to add additional features, and to improve control capabilities of SEAs.

With regards to the source of mechanical power, the main choices are hydraulic, pneumatic and electric motors. Among these choices, electric motors dominate the literature on SEA designs. Hydraulic actuation provides an excellent power-to-weight ratio and it is suitable for high force, low speed applications. Due to their high power density, a gear train is usually not necessary. Therefore, these actuators have been used in many successful mobile platforms such as legged robots (M. Raibert et al. (2008); Semini et al. (2010)). Figure 2.1 shows examples of hydraulic actuator-based mobile robots. The main drawback of hydraulic actuation is low efficiency. Also, hydraulic

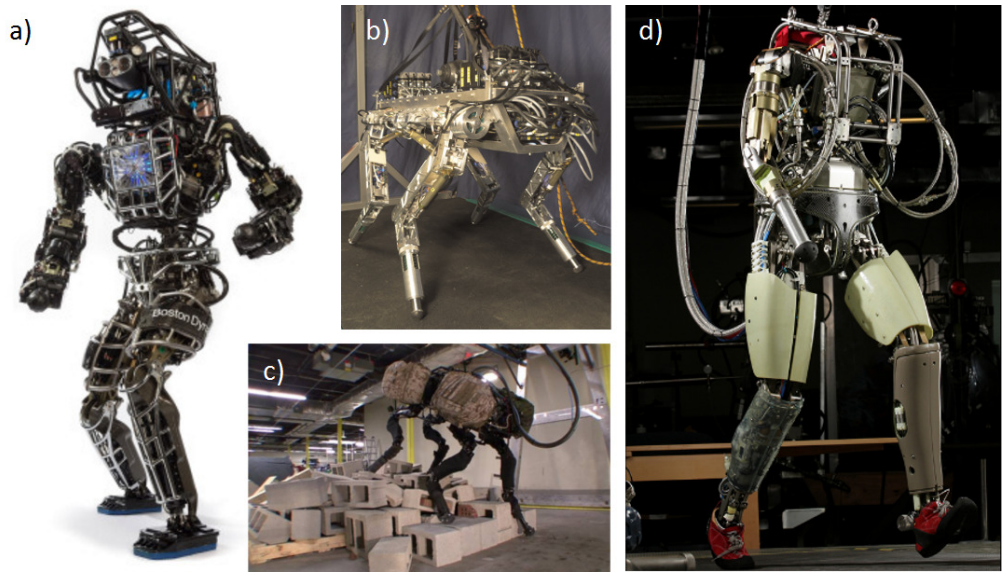


Figure 2.1: Examples of hydraulic-based mobile robots. a) Atlas[1]robot from Boston Dynamics, b) HyQ (Semini et al. (2011)), c) BigDog (M. Raibert et al. (2008)), d) Petman[2]robot from Boston Dynamics.

motors require pumps, which adds extra weight to the robot if an untethered platform is desired and makes the robot noisy if an internal combustion engine is used.

Pneumatic actuators (Niiyama et al. (2007, 2010)) have less power density compared to hydraulic system and are difficult to control due to the compressibility of the air. Similar to hydraulic actuation, a source of pressure is needed which adds weight and noise. In (Zheng et al. (2016)) and (Ortlieb et al. (2016)), the authors exploit the inherent compressibility of air and model the pneumatic actuator as a variable stiffness actuator. Figure 2.2 shows examples of pneumatic actuator-based mobile robots.

[1]http://www.bostondynamics.com/robot_Atlas.html
[2]http://www.bostondynamics.com/robot_petman.html

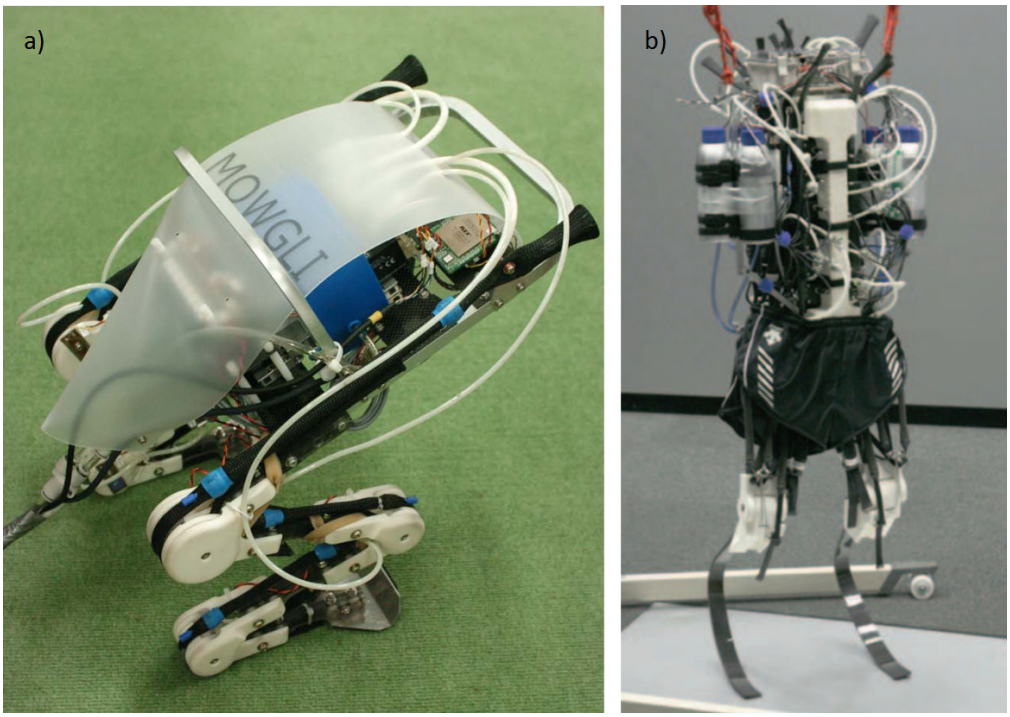


Figure 2.2: Examples of pneumatic-based mobile robots. a) MOWGLI (Niiyama et al. (2007)), b) Musculoskeletal Athlete Robot (Niiyama et al. (2010)).

Compared to hydraulic and pneumatic actuators, electric motors have a lower power density. However, electric motors are more energy efficient, clean and less noisy. These advantages make electric motors the primary choice for mobile robots, exoskeletons, prosthetic and orthosis devices and collaboration robots (CoBots). On the source of mechanical power, this literature review focuses on the SEA designs with electric motors. Figure 1.2 shows examples of SEA-based robotic applications which use electric motors as the source of mechanical power.

Due to the relatively low torque output capability of electric motors, a drivetrain is usually necessary in order to increase the torque and to reduce

the speed. When electric motors are used, the drivetrain becomes the key component for overall system efficiency. The drivetrain also dictates the actuator's overall shape, output type (rotational or prismatic), range of motion and backdrivability.

The vast variety of drivetrain components has allowed researchers to explore the design space for SEAs on compactness, lightweightness, backdrivability, efficiency, etc.

Compact and lightweight designs are important for legged robots and human assistive systems. In (Lagoda et al. (2010); Diftler et al. (2011); Sergi et al. (2012); Parmiggiani et al. (2012)), the authors use harmonic drives for speed reduction and custom-made high-stiffness planar springs as elastic elements. Harmonic drives are good for reducing backlash and keeping the actuator compact and lightweight. However, they suffer from poor backdrivability, high cost, low efficiency (25-80%) and torque ripple. The efficiency of harmonic drives heavily depend on the proper alignment, gear ratio, ambient temperature and proper lubrication. Since the number of engaged gear teeth is low, harmonic drives are prone to ratcheting and buckling under high loads. Custom designed planar springs are beneficial for compact, rotational SEA designs but are harder to manufacture and therefore lead to cost increases. The stiffness of planar springs are usually very high which reduces the amount of passive energy storage but increases the force bandwidth.

One of the first designs of SEAs (Torres-Jara & Banks (2005)), the authors present a simple and compact design based on linear die springs coupled

to a rotary shaft. This design approach has been adopted in (Hutter et al. (2011)) and (Hutter et al. (2013)).

In (Lu et al. (2015); Veneman et al. (2006)), compactness is achieved by using bowden-cable-based design and separating the actuators from the output joints. The main drawback of bowden-cable systems is their hard-to-model nonlinearities, which make them difficult for precision control.

In (Kong et al. (2012); Taylor (2011)), the spring is located within the speed reduction mechanism. Such designs allow for lighter springs since the torque on the spring is lower than at the output. The effect of the collocation of the spring was analyzed in (Sensinger et al. (2013)). In (Mathijssen et al. (2013)), elasticity is created via parallel linear springs of different stiffness. This design significantly reduces the required motor torque and increases the efficiency. In (Kong et al. (2012); dos Santos et al. (2015)), the authors use a worm-gear mechanism for speed reduction which allows the motor to be orthogonal to the joint axis. These designs are more suitable for knee orthosis. However, worm-gear systems suffer from poor efficiency and non-backdrivability.

A novel, rotary spring design for a compact SEA was presented in (Tsagarakis et al. (2009)). The rotary elastic component of this SEA is created by using a novel arrangement of linear springs. While this design is a low-cost alternative to high-priced custom planar springs, it suffers from nonlinear stiffness.

By using variable stiffness and nonlinear springs, the range of appli-

cations and control capabilities of SEAs can be extended. There has been major research on the benefits of adjustable (Hurst et al. (2010); Grebenstein et al. (2011); Jafari et al. (2013); Tonietti et al. (2005); Van Ham et al. (2007); Wolf & Hirzinger (2008)) and nonlinear (Thorson & Caldwell (2011)) stiffness springs. Also, a novel spring mechanism with an infinite range of stiffness was proposed in (Groothuis et al. (2014)) for SEAs. Like the effect of variable stiffness, the effect of variable physical damping (Laffranchi et al. (2014)) and continuously-variable transmission (Mooney & Herr (2013)) has been studied.

Also, a theoretical study on the benefits of clutch-able SEAs is presented in (Rouse et al. (2014)).

In (Gregorio et al. (1997); J. Pratt & Pratt (1998); J. E. Pratt & Krupp (2004); Edsinger-Gonzales & Weber (2004); Paine et al. (2014)), the authors use a ball-screw mechanism for speed reduction for prismatic SEA designs. Ball-screw mechanisms are highly efficient (90%), highly backdrivable, have a high tolerance for impact loads, and do not introduce torque ripples. Therefore, ball-screw mechanisms are good candidates for high-efficiency actuator designs. An important drawback of using a ball-screw mechanism is the fact that an output mechanism is needed for converting the prismatic output to rotation when necessary.

In (Curran & Orin (2008); Kong et al. (2009); Hutter et al. (2009); Kong et al. (2009); Ragonesi et al. (2011); Grün et al. (2012); Pott et al. (2013); Hasankola et al. (2013)), the authors use off-the-shelf components for designing SEAs, which is an important strategy to keep the costs low. The authors use

a planetary gearbox for speed reduction in their designs. Planetary gearboxes have low efficiency and poor impact tolerance due to their low backdrivability. Torque ripple and backlash are other drawbacks of planetary gearboxes.

A low-cost robotic arm with SEAs was presented in (Quigley et al. (2011)). In order to reduce the total cost, stepper motors, which are relatively cheaper and provide high torque at low speeds, were used. High motor torque eliminates the necessity of a high gear ratio speed reduction mechanism and, thus, reduces the cost and weight of the robot arm, while low motor speed limits the maximum joint velocity. The pHRI safety was achieved by using SEAs, but only the proximal four joints have SEAs in order to keep the total cost low. The series elasticity and force sensing of the SEAs were achieved by using polyurethane tubes, which is another important step to reduce the cost. The main drawback of polyurethane tubes is their nonlinear stiffness behavior with significant hysteresis. In (Campbell et al. (2011)), the authors propose a low-cost SEA for multi-robot manipulation applications. The authors use a planetary gearbox along with a capstan drive. The angular position at the joint is measured with a potentiometer. The compliance is achieved with a thin strip of spring steel. The overall cost is kept low by designing the custom parts with simple geometries. In (Catalano et al. (2011)), a modular and low-cost variable stiffness actuator was proposed which is designed to serve as a building block for low-cost multi-degree-of-freedom robot designs.

In (Kumpf (2007)), low-cost alternatives of SEA components as well as proof-of-concept designs are provided. The results of performance experiments

are also included in this study. The main focus of this work is reducing the cost of SEAs.

Although many different design configurations of SEAs have been investigated, low-cost realization of SEAs with a focus on high-performance and industrial grade strength have not been studied. Reducing the cost of SEAs without compromising too much on the performance is necessary for the industrial and educational SEA designs. The low-cost studies in the literature take the low-cost design aspect as the sole goal and report the performance of the designed hardware. High performance oriented low-cost designs are missing in the literature.

## 2.2 Control Approaches

The mechanical design of a piece of mechatronic hardware defines the upper bound of the efficiency of that hardware. Performing useful tasks in an efficient manner and achieving desired performance merits heavily depend on the applied control method and the success on implementing the selected control approach. The selection of the control approach, on the other hand, depends on the designed hardware and desired application. For instance, nonlinearities on the hardware specifications dictate nonlinear control approaches in order to stably control the system. On the other hand, an application which requires very high velocities at a given time or position (e.g. pitching a baseball with a robotic arm (Katsumata et al. (2009)) or hammering a nail with a SEA or VSA-based electric hammer (Garabini et al. (2011)) requires optimal control

approaches in order to find the optimal stiffness (Paluska & Herr (2006b)), optimal joint trajectory (Haddadin et al. (2012)) or optimal task time (Okada et al. (2002)).

The number of applications that use SEAs is increasing rapidly. The variety of applications leads to a variety of hardware designs as shown in Section 2.1 and, therefore, a variety in control approaches. In (Bae et al. (2010); Calanca et al. (2014); Wang et al. (2015); Sariyildiz et al. (2016)), the authors exploit the robustness of sliding mode control. A quadratic programming-based embedded nonlinear optimal control is used in (Ames & Holley (2014)). An adaptive control approach is used in (Calanca & Fiorini (2014)) for online adaptation to a changing environment. The optimal control approaches are mostly used for enhancing the performance of SEAs. These studies are reviewed in Section 2.3. The most common control approach used for SEAs is PID-based controllers and its derivatives. PID is a simple and intuitive control approach which provides great immunity to the external disturbances. The most common PID-based controller architecture used for SEAs consists of an inner torque and outer position or impedance control loops. In (Zinn et al. (2004); Kwa et al. (2009); Lagoda et al. (2010); Accoto et al. (2013); dos Santos & Siqueira (2014); Focchi et al. (2016)), the authors use a cascaded PID-based control approach. The bandwidth of the inner torque/force control is improved by using a disturbance observer in (Paine et al. (2014); Mehling et al. (2015)).

As stated previously, the control approach is selected according to the

desired application. Safe pHRI is one of the most common applications where SEAs are being used. The dynamic interaction between the robot and its environment can be controlled in multiple ways (M. H. Raibert & Craig (1981); Hogan (1985); Khatib (1987)). Among these methods, the most common and adopted approach is impedance control (Hogan (1985)).

Conventional controllers used on rigid robotic applications rely on regulating either the output force or the output position, as regulating both of these output parameters independently is physically impossible. However, these control approaches are not successful at achieving a stable interaction with the environment. For instance, a small position output error on contact with the environment results in very high torques on the joint, making the robot prone to instability.

In (Hogan (1985)), Hogan introduces the impedance control which regulates the dynamic relationship between the output force and output velocity. The mechanical impedance is defined as the mapping of a velocity input to a force output at the interaction port of a system with its environment:

$$Z(s) = \frac{F(s)}{sX(s)} \tag{2.1}$$

Figure 2.3 shows a depiction of the mechanical impedance of a SEA.

If a feedback controller is applied to this system according to the position error relative to a virtual reference point $x_0$, the impedance control law can be written as:

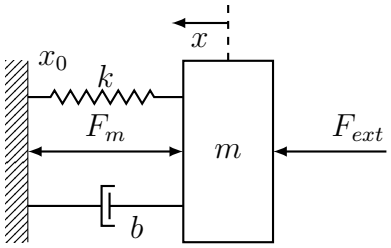


Figure 2.3: Representation of impedance for a single-DOF SEA. $m$ is the total sprung mass of the actuator, $k$ is the effective spring stiffness, $b$ is viscous friction, $F_m$ is the motor force, and $F_{ext}$ is the external force.

$$F_m = -k(x - x_0) - b(\dot{x} - \dot{x_0}). \tag{2.2}$$

This control law yields a PD control (Hogan & Buerger (2005)) where the equivalent damping is the summation of the physical damping, $b$, and the virtual damping defined by the derivative gain in a PD-type controller (Paine & Sentis (2015)). Similarly, the equivalent stiffness becomes the summation of physical spring stiffness, $k$, and the virtual stiffness defined by the proportional gain of the PD-type controller. This approach gives an intuitive understanding of the relationship between each feedback gain parameter and its physical interpretation. Other control approaches such as full state feedback control on impedance (Loughlin et al. (2007); Ott (2008); Albu-Schäffer et al. (2007)) and adaptive state feedback control on torque (Kaya & Çetin (2017)) have been implemented. However, as the number of feedback parameters increase, the physical meaning of these parameters become hard to grasp in these approaches.

Impedance control with an inner force/torque control loop is widely

adopted (Sensinger et al. (2006); Isik et al. (2017) because, by definition, the impedance is the dynamic relationship between the force/torque and velocity/position[3] and in a cascaded impedance controller with an inner torque loop, the impedance controller generates the reference torque input for the torque controller (Holmberg et al. (1993)).

The main drawback of the cascaded impedance controller is that the performance of the outer control loop heavily depends on the behavior of inner control loop. In order to improve the overall system's performance, the authors in (G. A. Pratt et al. (2004); Sensinger & Weir (2006); Vallery et al. (2007); Wyeth (2008); Hutter et al. (2013)) used an innermost motor velocity/position control loop which improves the robustness by eliminating the negative effects of drivetrain imperfections such as backlash and nonlinear friction. In (Kong et al. (2012); Paine et al. (2014)), the authors use a disturbance observer in order to improve the force control bandwidth. In (Mosadeghzad et al. (2012)), the authors provide a comparison of various impedance control approaches.

As stated previously, the PD-type controllers provide an intuitive understanding of the expected effect of the feedback gains on the system. However, as the order of the system gets higher than two and the controller architecture consists of multiple loops, gain selection for PD-type feedback controllers becomes difficult, and intuitive understanding of the feedback gains' effects on the system can be missed. Therefore, gain selection for complex systems is mostly done empirically. Ziegler & Nichols proposed an empirical gain tuning

[3]Even though the conventional representation of impedance is $Z = F/\dot{x}$, $Z = F/x$ is also a used and accepted representation of impedance in the literature. (Paine & Sentis (2015))

method in (Ziegler & Nichols (1942)) which is widely known as "Ziegler-Nichols gain tuning method" and used in many industrial control applications.

Empirical gain tuning methods are time-consuming and do not provide the user with sufficient information about the system behavior on non-tested cases and, more importantly, the stability margins of the system. A common practice for gain tuning of the cascaded controllers is tuning the gains for the inner control loop for maximizing its bandwidth and then selecting the feedback gains of the outer controller for the desired overall system behavior (Ellis (2012)). However, this method limits the bandwidth of the outer control loop (Focchi et al. (2016)). In a recent study, Zhao et al. proposed a gain selection method for fourth order PD-type impedance controllers for a critically damped output behavior (Zhao et al. (2014)). This method, however, does not exploit the potential benefit of independent scaling of the inner and outer control loops' natural frequencies. In this dissertation, an ideal feedback gain selection method for the fourth order PD-type cascaded impedance controllers with time-delay and derivative filtering is provided in Chapter 4. The proposed method allows the user to select the highest feedback gains which satisfies the desired phase-margin constraint and provides a critically damped system behavior.

## 2.3 Performance Enhancements through Series Elasticity

Robots are mainly built to perform the tasks that normally humans do. Therefore, the majority of the robotic systems either partially or completely mimic human body in a morphologic sense. More specifically, as the most common robotic system used today, the industrial robots are built to match and even outperform the capabilities of the human arm, since we handle our daily tasks mostly using our arms and hands. In biomimetic robotics, the physical properties and capabilities of not only the humans but also animals are the sources of inspiration for robotic application development.

Beyond the kinematic structure, mimicking the biomechanic properties of the muscular system of humans and animals offer great possibilities of performance improvements for robotic applications. Tendons in the human body provide elasticity to the joints. We use our tendons to temporarily store and release mechanical energy for the tasks which require bursts of power output on our limbs, such as jumping, pitching a baseball or kicking a soccer ball. The research on properties and effects of tendons in the human body is abundant in the biomechanics literature. The effect of tendons on locomotion is analyzed in (Roberts (2002)). Jumping is another example where the elasticity of tendons is being used. The effect of tendons on the jumping performance of humans was analyzed in (Kubo et al. (1999)). The stretch and release motion of horses' biceps during galloping and the effect of elasticity in their muscles

is analyzed in (Wilson et al. (2003)). The mechanical energy efficiency as a result of series elasticity in the muscle-tendon system during stretch-shorten cycles of locomotion was analyzed in (Ettema (1996)).

With the capability of storing and releasing mechanical energy, SEAs are great candidates for mimicking the tendons in human body and exploiting the performance improvements that series elasticity provides. By controllably charging the elastic element with potential energy and then converting this potential energy to kinetic energy, the velocity output of the actuator can be improved beyond the limits of rigid actuators.

Performance enhancements of SEAs require the use of optimality principles when the goal is to achieve the maximum possible joint velocity. Optimality principles can be applied on the system hardware parameters, control approaches or task-level motion planning. In one of the early studies on the skill of compliance, the authors use an experimental iterative method to find the swing motion that maximizes the hand velocity of a 2-DOF under-actuated robotic arm (Okada et al. (2002)). In order to find the motion trajectory that maximizes the hand velocity, the total task time allowed for winding up and swing is changed. Although this method offers a solution for the hardware that the authors used, it does not provide a general solution for different robotic applications.

In (Paluska & Herr (2006b)), the authors analyze the effect of spring stiffness on joint velocity improvement, i.e. actuator power output over a limited stroke. The authors show that an appropriate spring constant can

increase the peak power by a factor of 2 for single shot motions (windup and throw).

The physical capabilities of the human body are pushed to their limits during sport activities. Soccer is a competitive game where the tendons in a soccer player's legs play an important role on achieving high velocities when kicking the soccer ball. In (Haddadin et al. (2009)), the authors experimentally show a velocity increase by a factor of 2.45 by using a VSA-based robot leg as opposed to the maximum velocity provided by the KUKA KR500, one of the world's largest industrial robots with 500 kg payload capacity. Also, a theoretical analysis on the maximum achievable joint velocity with a constant stiffness elastic actuator was provided in this study. The geometrical constraints and nonlinear elasticity were ignored in order not to overly complicate the theoretical study. However, these assumptions limit the applicability of this analysis to different type of applications.

The maximum attainable joint velocity in a SEA depends on the physical properties and limitations of the system components and designed hardware. The dependency of the joint velocity increase on joint limits and optimum stiffness selection have been analyzed in (Hondo & Mizuuchi (2011)). In this study, the authors also show that the inertia balance between the motor and the load affects the resulting joint velocity increase.

Aside from the optimality on the hardware components, optimal control principles are used to achieve higher joint velocities. In (Haddadin et al. (2011)), the authors use bang-bang control in multiple scenarios such as

the use of constant stiffness (SEA) and variable stiffness (Variable Impedance Actuator, VIA) as actuator type and realistic constraints on the system hardware, such as joint limits and constrained deflection on the elastic element. A similar approach was used in (Garabini et al. (2011)) in order to maximize the velocity of a VSA-based hammer, thus maximizing the impact force on the nail. In this study, an optimal control approach is used to maximize the joint velocity at the desired joint position. The joint velocity improvement study in (Haddadin et al. (2011)) was extended for the case with adjustable nonlinear springs in (Özparpucu & Albu-Schäffer (2014)).

In a recent study, a bioinspired robotics leg with series elastic actuation was introduced in (Haldane et al. (2016)). In this study, the main goal is to achieve high vertical jumping agility. The authors use a power modulation approach in order to improve the joint velocity of the robotic leg and compare the result with the vertical jumping performance of the galago (*Galago senegalensis*) which is the animal with highest vertical jumping agility (Haldane et al. (2016)). Using this approach, 78% of of vertical jumping agility of galago was achieved by the authors, whereas the previous highest performance value was 55%.

Increasing the joint velocity using series elasticity depends on controllably storing and releasing potential energy in the elastic element. Using clutches on the actuators adds extra control on timely releasing the stored energy. In (Chen et al. (2013)), the authors use a clutched SEA which acts as a rigid actuator when the clutch is in the ON mode. In this study, the

ON-OFF switch times are optimized in order to achieve high joint velocities. Two linear models are used for the states in which the clutch is in ON or OFF mode, and the input profiles for these linear modes are optimized using convex optimization. Using a clutch parallel to the elastic element improves the performance of the joint velocity maximization. However, similarly to variable elasticity, clutches add extra weight to the actuator, which is undesirable for multi-DOF systems.

In the literature, the authors take different approaches in order to improve the joint velocity utilizing the series elasticity of SEAs and VSAs. In some of the proposed approaches, the authors focus on optimizing the hardware properties such as the spring stiffness or the inertia balance between the motor and the load. In this dissertation, I propose an optimization approach which handles the nonlinearities which are introduced by gravitational forces and nonlinear kinematic structures in the actuator. The proposed optimization method is simulated for a nonlinear single-DOF system and the results are presented in Chapter 5.

# Chapter 3

# Design of a Low-Cost, Industrial Grade Series Elastic Actuator

## 3.1 The Importance of Low-Cost Hardware

Several benefits of using SEAs were mentioned in the previous chapters. Considering their safety benefits, the trend in the robotics community to employ more SEAs in their robotic applications and the potential expansion of task space application capabilities offered by SEAs, it is clear that the research on SEAs in academia and the usage of them in the industry will increase. Therefore, the low-cost realization of SEA designs requires more exploration. The utilization of the safe robots can greatly help the economy, but the capital cost of robot installation currently stands as an obstacle. For example, one of the biggest electronics suppliers of the world, Foxconn Inc., plans to replace 60,000 of its workers with robots (Wakefield (2016)). This example alone shows how

much impact that cost reduction of robots and robotic hardware can make for even a single company. The same situation holds for medical companies that design orthotic devices; military companies that design human skill augmentation devices such as exoskeletons; and many safety-centered robotics research laboratories around the world.

The increasing usage of SEAs in industry, education, rehabilitation, and service robotics makes it important to educate future generations on the design and control of SEAs. The costs of SEAs and SEA-based robotic arms are still limiting to many audiences. Even the SEA-based industrial robots that are known to be low-cost such as Baxter (Fitzgerald (2013)) are still not economically accessible for many laboratories, especially in developing countries. As a researcher and future educator, I believe that the ways of reducing the cost of low-volume mechatronics research hardware require further exploration in order to increase their accessibility to a wider range of laboratories and institutions. This endeavor will allow research laboratories and universities to build their own robotic hardware, conduct quality research, and provide better education.

Lower cost alone is not a sufficient target goal for a mechatronics hardware design because one can reduce the cost of the hardware as much as he/she desires by compromising other design and control aspects. Industrial and educational hardware should have structural sturdiness, considerably high service life, and high performance on desired functionalities. Therefore, the necessary performance limits should be set before the design process, and cost reduc-

tion methods should be applied while matching those performance goals. The low-cost SEA designs in the literature either do not possess these qualities or do not address them at all. Therefore, it is necessary to study the cost aspect of low-volume research and educational SEAs and to raise awareness on this design aspect.

## 3.2 A Case Study on Low-Cost Series Elastic Actuator Design

### 3.2.1 Mechanical Design

Setting the design goals for the desired application is a crucial step for keeping the costs low. Only the necessary properties of the system should be taken into consideration and their priorities should be properly sorted. For example, the energy density is an important design aspect for the SEAs which are designed to be used for humanoid robots or orthosis systems while it has a lower priority for industrial setups since they are usually rigidly grounded. For this case study, maximum output speed, continuous output force, cost, backlash, control bandwidth, mechanical strength, service life and human safety are the important considerations. For the sake of mechanical strength and long service life, the weight of the actuator is considered as low priority.

Target output speed and force values are taken from the re-engineered model, the UT-SEA (Paine et al. (2014)). While keeping the force and position control performance comparable to the UT-SEA, we targeted half of the cost

for the new SEA. Table 3.1 shows the available properties of the UT-SEA and targeted and achieved values of the new SA-SEA.

Table 3.1: Properties of the UT-SEA (Paine et al. (2014)), design goals and achieved properties of the SA-SEA.

| **Design Aspect** | **UT-SEA** | **Target Value** | **SA-SEA** |
|---|---|---|---|
| Cont. Output Force | 848 N | 848 N | 829.96 N |
| Peak Output Force | 2800 N | 2800 N | 2355.47 N |
| Peak Output Speed | 32.5 cm/s | 32.5 cm/s | 28.8 cm/s |
| Cost | $5100 | <$2550 | $1750 |
| Force Bandwidth | 18 Hz | 10 Hz | 8.5 Hz |
| Expected Service Life | N/A | 40,000 h | >60,000 h |
| Force Sensitivity | 0.31 N | 0.31 N | 0.06 N |
| Stroke | 6 cm | 6 cm | 7.1 cm |
| Weight | 1168 g | N/A | 3280 g |

After setting the force and speed goals, the selection of the speed reduction mechanism is a critical step for the overall performance of the system. The system's mechanical efficiency and backlash are mainly affected by the speed reduction mechanism. Backlash is an undesired property for most of the engineering systems and the existence of backlash adversely affects system stability and repeatability. Harmonic drives and ball-screw mechanisms are the best solutions for backlash problems. Between the two, ball-screw mechanisms are more durable against excessive forces and impact loads. The typical efficiency of the ball-screw mechanisms is in the order of 90% whereas the typical efficiency of harmonic drives is in the order of 80%. Ball-screw mechanisms are also cost effective solutions for prismatic motions and are therefore a good candidate for a low-cost SEA.

There are two stages of speed reduction in the SA-SEA which are the ball-screw mechanism and the pulley system. Since the ball-screw mechanism is a more expensive component than the pulley system and has a greater possibility of cost reduction, I selected the ball-screw mechanism first and then selected the pulley ratio accordingly in order to meet the design requirements. It was kept in mind that having a high pulley ratio will affect the overall actuator size. By using Equation (3.1) and using a maximum pulley ratio of 3:1, the BSHR01205-3.5 model ball-screw mechanism from TBI Motion (New Taipei City, Taiwan) was selected which requires less than 0.5 Nm input torque for the desired force output. This maximum torque value was set in order to keep the cost and size of the motor under reasonable values. In the following equation, ($T$) is motor torque, ($F$) is force output, ($l$) is ball-screw lead, ($N$) is pulley ratio, and ($\eta$) is ball-screw mechanism's efficiency.

$$T = \frac{F\,l}{N\,2\pi\,\eta} \tag{3.1}$$

The selected ball-screw mechanism requires 0.25 Nm of motor torque if we choose the 3:1 pulley ratio in order to match the continuous force output target. For cost reasons, I decided to use an AC servo motor and selected the TS4603 model from Tamagawa Seiki Co., LTD (Iida, Japan) with 0.318 Nm continuous torque output. The selected motor driver is compatible with Programmable Logic Controllers (PLCs) and has its own PID controller both of which are widely used in industrial control applications. The price for the torque was the main consideration for motor selection.

Solving the Equation (3.1) for $N$ with the given rated torque and specifications of the selected ball-screw mechanism gives a pulley ratio of 2.36. Considering the available pulley teeth numbers, the desired mechanical strength of the pulleys and the suitable timing belts, a 60:26 timing pulley ratio was selected, which gives slightly lower output values than the desired ones.

The peak output force with the selected motor and assumed drivetrain efficiency (95% for the pulley system and 90% for the ball-screw mechanism) was calculated to be 2355 N for the chosen system parameters. The spring should reach this force value before reaching its shut length. Using soft springs allows higher force sensing resolution since the distance traveled for the same force will be longer. On the other hand, softer springs reduce the bandwidth of the system. Having these in mind, I selected the TL50-060 from Tohatsu Springs (Tokyo, Japan) which has 137.96 N/mm stiffness. Since two springs are used in series, the effective spring stiffness is expected to be 275.8 N/mm. With 10 mm allowed working distance after pre-compression, this stiffness is high enough to hold the maximum peak force created by the motor.

For force sensing, the linear motion of the spring is converted to rotational motion by using a pulley system. After setting the allowed working distance of the spring, there are two variables affecting the force resolution. These are the sensor resolution and the diameter of the pulley used at the sensor shaft. By considering the minimum number of teeth available for the timing pulley, I selected the 17-bit TS5667N120 from Tamagawa Seiki Co., LTD. (Iida, Japan) which provides 0.06 N force resolution. This is a low-cost

absolute encoder with RS-485 Non-Return-to-Zero (NRZ) communication protocol which has great immunity to the noise in industrial environments and has fast data transfer rates as high as 50 MBaud.

The force sensing mechanism was also re-engineered to be more durable and easily calibrated. The number of encoders was reduced to one from two which contributes to cost reduction. The selected encoder significantly increases the force sensing resolution. Figure 3.1 shows the force sensing mechanism of the SA-SEA.

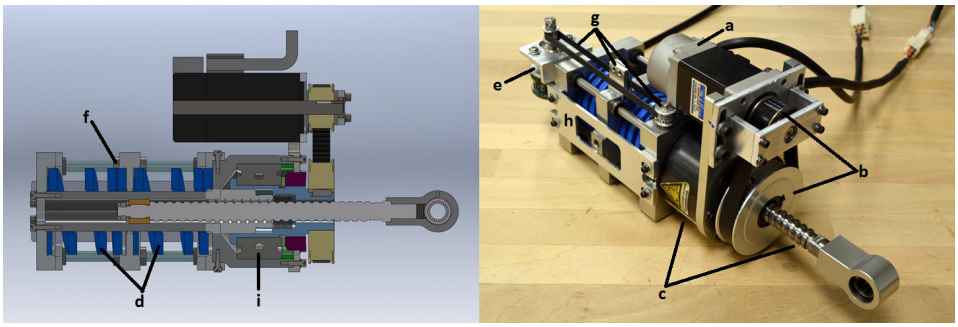


Figure 3.1: The SA-SEA and its cross section showing (**a**) Tamagawa Seiki Co., LTD TS4603 motor; (**b**) 60:26 pulley system; (**c**) TBI Motion BSHR01205-3.5 ball-screw mechanism; (**d**) Tohatsu Springs TL50-060; (**e**) Tamagawa Seiki Co., LTD TS5667N120 17-bit absolute encoder; (**f**) Misumi BGSTZ6-90 miniature ball bearing guides; (**g**) Force sensing mechanism; (**h**) Side bracket for easy assembly and torsional stiffness; (**i**) Misumi B7006-DB angular ball bearings.

The expected service life of the actuator heavily depends on the ball-screw mechanism which is the component that is the most prone to deterioration over time. There are many aspects affecting the service life of the ball-screw mechanism. For instance, proper lubrication, assembly, and operation as well as environmental variables such as dust are factors affecting service

life.

I calculated the service life of the ball-screw mechanism by assuming that the actuator output is making a sinusoidal motion with the highest continuous actuator output speed. I also assumed that a sinusoidal axial load with an amplitude matching the maximum continuous force output of the actuator will be applied. By using Equation (3.2), the expected service life is calculated to be 60,894 h. Since SEAs increase the lifetime of drivetrain components, the expected service life of the ball-screw mechanism is higher than the calculated value. In Equation (3.2), $L_t$ is the expected life of the ball-screw mechanism, $C_a$ is the basic dynamic load rating which is taken from the component datasheet, $P_e$ is the average axial load (65% of the maximum load for sinusoidal motion), $f_w$ is the load factor (1 for very low vibration and impact conditions), and $n$ is the average rotational speed (65% of the maximum speed for sinusoidal motion).

$$L_t = (\frac{C_a}{P_e\, f_w})^3\, 10^6\, \frac{1}{60\, n} \tag{3.2}$$

All other off-the-shelf components such as bearings and timing belts are selected by considering the targeted service life of the actuator and its cost-effectiveness. The custom parts are designed to minimize the machining time of the aluminum plates and ease the assembly of parts. In order to make the assembly process easier and to add torsional stiffness to the actuator body, side plates are added to the design (h in Figure 3.1).

### 3.2.2 The Testbed and Control Hardware

The SA-SEA was designed to be low-cost and industrial grade. Therefore, the motor driver is selected to be compatible with common industrial controllers and control approaches. The selected motor driver is able to perform simple PID-based control loops on the motor and also compatible with Programmable Logic Controllers (PLCs). However, in order to perform relatively complicated performance tests and safety experiments on the developed actuator, it is necessary to design an actuator testbed with a more capable control hardware.

In order to run high-performance real-time control routines, I used a PC-104 type embedded PC (ADLS15PC, ADL Embedded Solutions) which runs Linux with RTAI patch. The control loop runs with 1 kHz frequency while the sensor data is updated at 2 kHz on a separate control thread. The communication between the control PC and the sensors on the actuator handled with a serial communication board (SuperFSCC-104-02, Commtech, Inc.) which uses RS-485 NRZ communication protocol. Torque commands are sent to the motor driver using a DAC board (104-AIO12-8, ADL Embedded Solutions) stacked with the control PC. Figure 3.2 show the control PC stack.

The SA-SEA is a linear actuator and it requires either a slider mechanism in order to create a linear motion or a rotational joint mechanism in order to create a rotational motion. Similar to the UT-SEA (Paine et al. (2014)), I created a rotational motion mechanism with a rotational encoder attached to it. Figure 3.3 shows the SA-SEA in its testbed with motor driver.

The overall system structure can be seen in Figure 3.4.

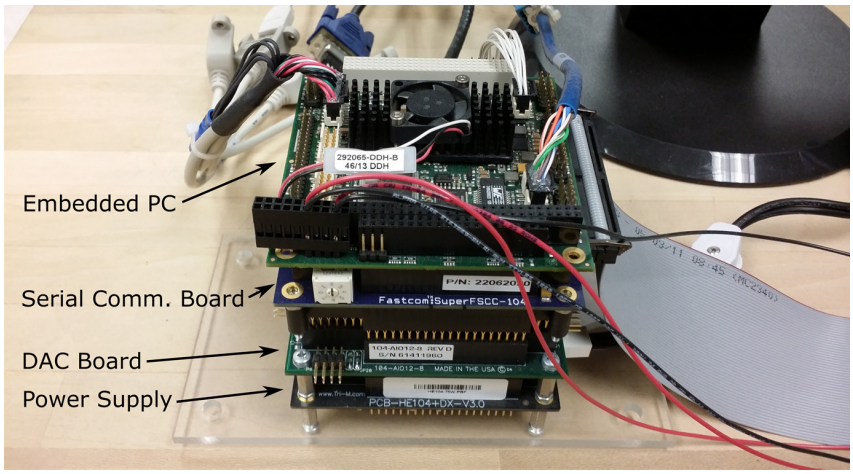


Figure 3.2: Embedded control stack of the SA-SEA.

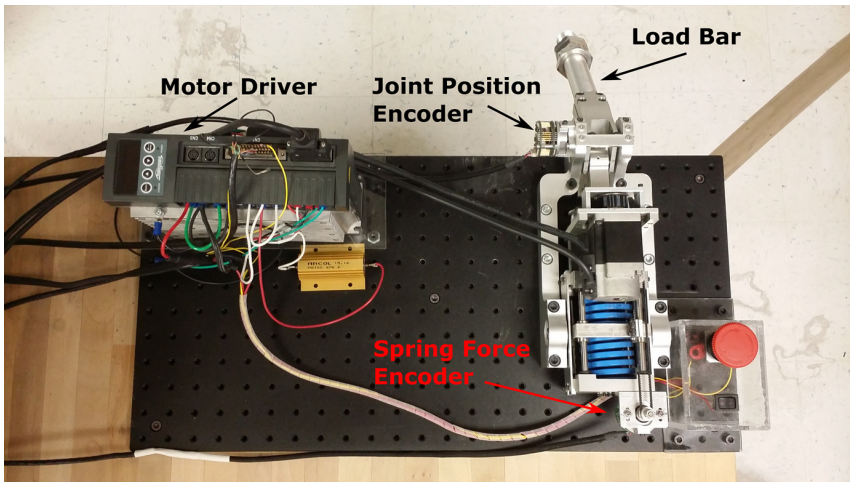


Figure 3.3: Top view of the actuator testbed.

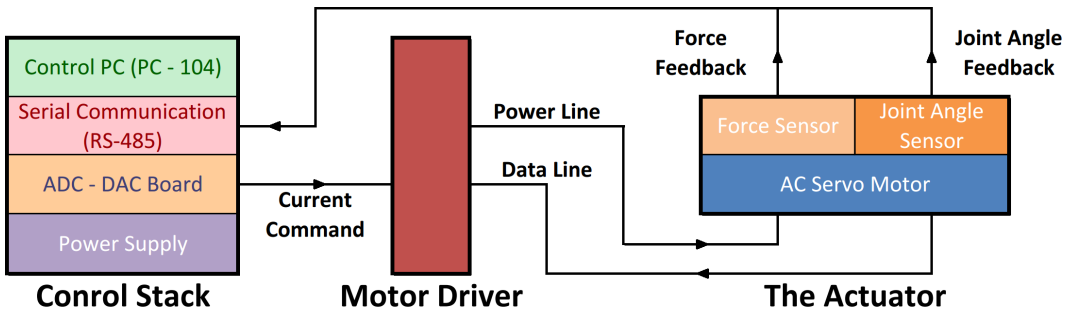


Figure 3.4: Control hardware structure of the testbed.

### 3.2.3 Modeling

In order to achieve high performance from the controller, it is important to build a good model of the system and characterize the system components. In this section, the modeling of the SA-SEA and characterization of the spring are presented.

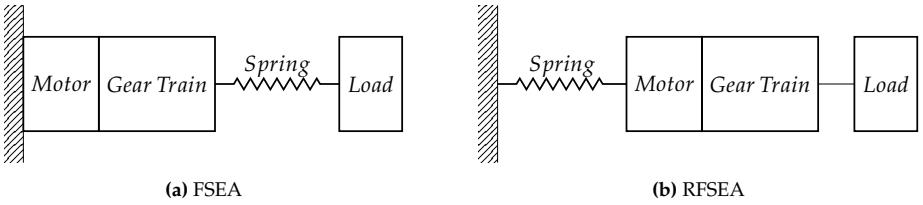


**(a)** FSEA **(b)** RFSEA

Figure 3.5: Simplified models of FSEA (**a**) and RFSEA (**b**).

There are two fundamental SEA structures. These are referred to as Force Sensing Series Elastic Actuator (FSEA) and Reaction Force Sensing Series Elastic Actuator (RFSEA) (Paine et al. (2014)). Figure 3.5 shows the simplified models of FSEA and RFSEA. The re-engineered SEA in this study has the RFSEA structure. Compared to prismatic FSEAs, RFSEAs are more compact and have a larger range of motion. In RFSEA designs, the spring is located between the motor and the ground. Therefore, the load is directly connected to the gear train. While this reduces the impact tolerance, compensation is provided by the high impact tolerance of the ball-screw mechanism. Another drawback of RFSEA is the larger sprung mass which includes the mass of the motor, inertia of the rotor and the gear train. This results in a more complex force calculation for the RFSEAs. For FSEAs, the output

force can be calculated directly from spring deflection whereas for RFSEAs, the force seen at the output is the sum of the inertial force of the sprung mass of the actuator, the force due to the effective friction in the system, and the spring force. Figure 3.6 shows the general model of the SA-SEA which shows the system components affecting output force.

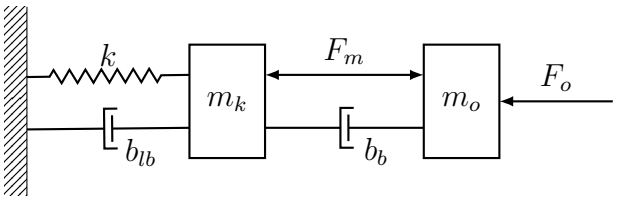


Figure 3.6: The lumped model of the SA-SEA. Here, $k$ is the effective spring stiffness, $b_{lb}$ is viscous friction at the linear ball bearings supporting the spring cage, $m_k$ is the total sprung mass of the actuator, $F_m$ is the motor force, $b_b$ is the viscous back-drive friction of the ball-screw mechanism, $m_o$ is the output mass and $F_o$ is the output force.

Characterization of the components is important for creating an accurate model of the system. It is especially important for low-cost components since there is a greater chance of having different performance values than the ones given in the datasheets. The characterization process begins with the calibration of the force sensor in order to find the zero force position of the encoder. To to this, I disconnected the actuator from the joint and mounted it horizontally to the table. After calibrating the force sensor, I started spring characterization process. I kept the output shaft of the joint parallel to the ground, locked the gear train, applied known forces in both directions from 0.3 m distance and recorded the sensor readings. The effect of the output bar's weight has been taken into account. The Figure 3.7 shows the normalized

applied force v.s. sensor readings. As the figure shows, the spring is perfectly linear in the testing range but there is a slight shift on the force readings on $y$-axis. This shift is introduced by the force bias due to the motor mass sliding on the ball bearings because of its sloped position.

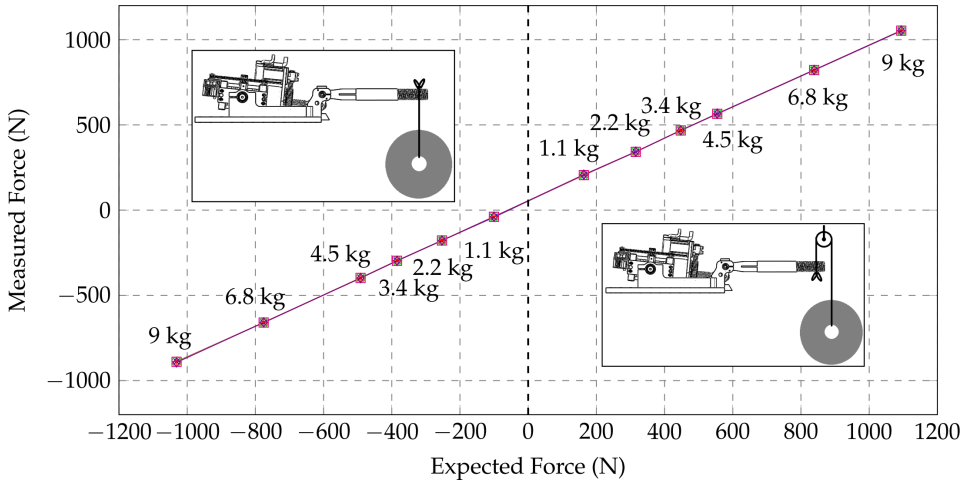


Figure 3.7: Spring characterization graph. Each experiment was performed 6 times. The graph shows the consistency of the experiment results. The approximate values of the dumbbell weights used in these experiments are: 1.1, 2.2, 3.4, 4.5, 6.8 and 9 kg.

The motor used in this project is an industrial AC servo motor which is designed to be used at relatively high speeds. When the motor is used at high speeds, the rotor inertia acts like a low-pass filter and cancels out the torque ripples seen at the motor output. In force control applications such as gravity compensation, the motor rotates at lower speeds. This makes the torque ripples seen at the output of the low-cost AC servo motors more observable. Figure 3.8 shows the torque ripples seen at the actuator for a ramp input. These ripples were canceled out by using the PID-based force control

explained in Section 3.2.4.

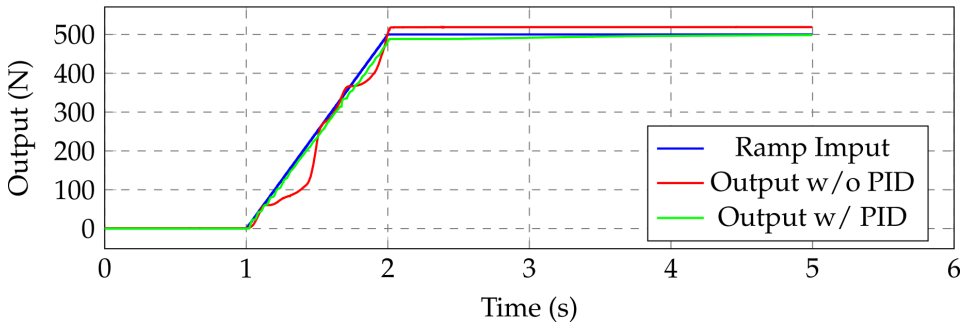


Figure 3.8: Torque ripple cancellation with PID-based force controller.

At this point, it is important to point out that I made sure that the ripples seen at spring force originated from the motor. I checked this by observing the torque ripples when the motor was disconnected from the drivetrain.

Some of the system parameters such as the sprung mass of the actuator and the effective viscous friction in the system are hard to calculate. System identification is a useful tool for having an accurate system model. Unfortunately, the high torque ripples prevent a successful open-loop system identification. Therefore, I performed closed-loop system identification by using the proposed force controller in Section 3.2.4.

### 3.2.4 Controller Design

There are two types of control mode discussed in this section. These are force control and joint position control. The goal in force control mode is to achieve a near ideal force source behavior from the SA-SEA and accurately track dynamically changing desired forces in the targeted bandwidth. For the

joint position control, the goal is to follow the rapidly changing desired joint positions accurately. The position controller was built on top of the force controller by using it as a building block. In this section, development of the control architectures are presented.

### Force Controller

In order to simplify the force control architecture, I used a high impedance output setup. Figure 3.9 shows the model of the high impedance setup created by grounding the actuator output. In this configuration, $F_o = F_m + F_{b_b} = F_{m_k} + F_{b_{eff}} + F_k$. As a result, the output force equation can be written as

$$F_o = m_a\ddot{x} + b_{eff}\dot{x} + kx \tag{3.3}$$

where $b_{eff}$ is the effective viscous friction in the actuator.

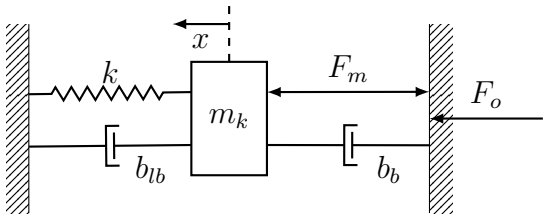


Figure 3.9: Model of RFSEA for force control with high impedance load.

Equation (3.3) requires derivation of both $\ddot{x}$ and $\dot{x}$ for an accurate force feedback, especially at high frequencies. Considering the mechanical failure possibility of RFSEA design near resonant frequency (Paine et al. (2014)), the spring force was controlled by using Hooke's Law:

$$F_k = kx \tag{3.4}$$

This approach sacrifices the accuracy of force feedback at high frequencies but guarantees stable control for a wide range of frequencies. The transfer function between the motor force and the spring force can be written as

$$\frac{F_k(s)}{F_m(s)} = \frac{k}{s^2 m_k + s b_{eff} + k} \tag{3.5}$$

Equation (3.5) yields a second order mass-spring-damper system. In this equation, $m_k$ represents the sprung mass of the actuator which includes the inertial elements of the actuator such as the motor mass, the partial mass of the ball-screw mechanism and the springs, as well as the rotational inertia of the rotor. Finding $m_k$ and $b_{eff}$ requires extensive study of the system. In order to find the unknown system parameters, I performed closed-loop system identification by using the force controller shown in Figure 3.10. I used an exponential chirp signal as $F_d$ and fitted the experimentally found model to Equation (3.5). By using the known gains and system parameters, I found that $m_k \approx 64$ kg and $b_{eff} \approx 921.6 Ns/m$.

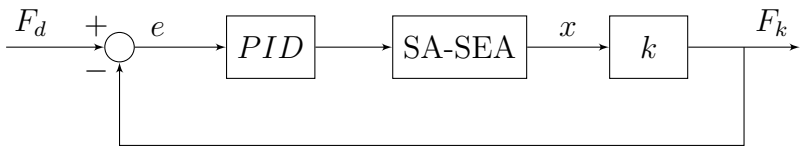


Figure 3.10: Force controller for high impedance RFSEA setup.

Since the SA-SEA was designed for industrial and educational appli-

cations, I only used a PID controller. PID control is a simple and effective control approach used for more than 90% of the industrial control applications. It is also one of the most fundamental control method taught in control education. PID control can be realized by using a PLC which is a common controller selection in industry. Figure 3.10 shows the force controller used in this study. As it can be seen on the controller diagram, there is no filter applied to the feedback signal. Low noise level on the feedback was achieved by taking advantage of the high noise immunity of the RS-485 communication and the high data update rate of the encoder. This enables multiple sensor readings to be done in one control cycle, eliminating any inconsistent feedback data. The only filter used in this controller is a first order low-pass derivative filter. In this control approach, the required motor torque command is calculated from the desired spring force by using the system parameters and is sent to the motor driver.

**Position Controller**

The second controller designed for the SA-SEA is a joint position controller. In joint position control, the goal is to accurately follow the rapidly changing desired joint positions. After achieving an accurate force control performance, I used the designed force controller as a building block for the position controller. The force created at the actuator output is converted to joint torque using the mechanism shown in Figure 3.11. The joint torque ($\tau_a$) which is created with the force output of the actuator ($F$) can be calculated as follows:

$$\tau_a = FL(\theta_a) = F\frac{bc\ sin\ \theta_a}{\sqrt{b^2 + c^2 - 2bc\ cos\ \theta_a}}. \tag{3.6}$$

Also, the relationship between the joint torque and the load dynamics can be calculated as,

$$\tau_a = J_a\ddot{\varphi} + B\dot{\varphi} + \tau_g(\varphi). \tag{3.7}$$

In this equation, $J_a$ represents the load inertia, $B$ represents the joint friction and $\tau_g(\varphi)$ represents the torque created by gravity and can be calculated as,

$$\tau_g(\varphi) = m_a g l_{m_a}\ cos\ \varphi \tag{3.8}$$

where $m_a$ is load mass and $l_{m_a}$ is the distance of the center of the load mass to the joint. The joint angle $\varphi$ is determined by the joint position sensor and $\theta_a$ used in Equation (3.6) is dependent on joint angle.

Using equations (3.6)–(3.8), the nonlinear equation governing the load dynamics can be written as,

$$F = \frac{\sqrt{b^2 + c^2 - 2bc\ cos\ \theta_a}}{bc\ sin\ \theta_a}[J_a\ddot{\varphi} + B\dot{\varphi} + m_a g l_{m_a}\ cos\ \varphi]. \tag{3.9}$$

As Figure 3.12 shows, the required joint torque is derived using the desired joint trajectory plus the gravity effect based on the joint position. The inertial and friction force terms are included as a feed-forward term. The desired actuator force output is calculated by using the inverse of $L(\theta_a)$ and

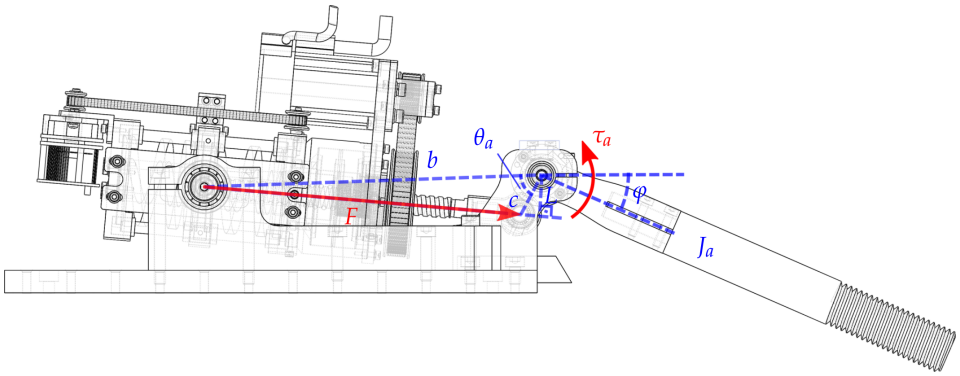


Figure 3.11: Kinematic structure of the joint link mechanism.

is sent to the force controller.

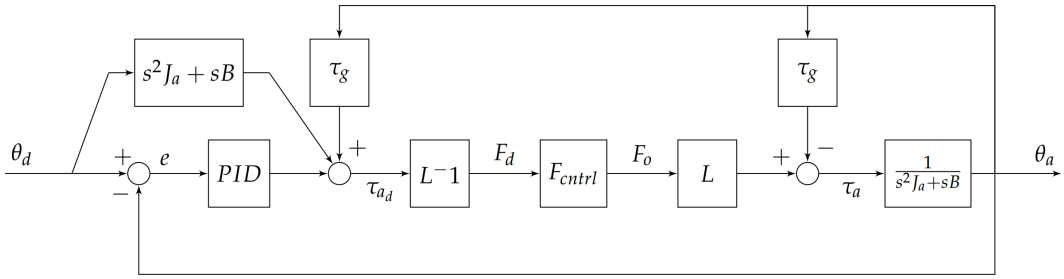


Figure 3.12: Joint position controller.

### 3.2.5 Performance Tests

The main goal of this study is to achieve high performance from a low-cost SEA. Fundamentally, we aim for comparable performance to the UT-SEA in terms of its force and position tracking capability. These are building blocks for any higher level controllers and directly affect the system's overall performance.

I also performed an impact recognition test in order to analyze the system's mechanical robustness and responsiveness. The performance of the

SA-SEA on these tests is critical for its use in industrial applications. The results of the experiments are presented in this section.

### Force Control

For force input tracking, the actuator output was rigidly grounded as modeled in Figure 3.9 and a PID-based force controller, which is shown in Figure 3.10, was used. In order to see the system's response for rapid changes in desired force, I applied an exponential chirp signal with an amplitude of 100 N and a frequency range of 0.1–100 Hz for a 30 s duration. This experiment is necessary in order to see the system's frequency response at high frequencies and to see the force bandwidth of the system.

Figure 3.13 shows the Bode plot of this experiment. As it can be seen, the SA-SEA shows good force tracking performance at lower frequencies and the actuator output degrades at higher frequencies. The Bode plot shows that the force tracking bandwidth is 8.5 Hz, which is lower than the targeted bandwidth of 10 Hz. The Bode plot also shows that the magnitude values increase at high frequencies instead of decrease, which is due to the high frequency noise on the recorded output data.

The bandwidth of force tracking can be improved by using model-based controllers. For simplicity, I used a PID-based controller only. A higher bandwidth can be achieved by testing the force controller with a smaller amplitude reference signal.

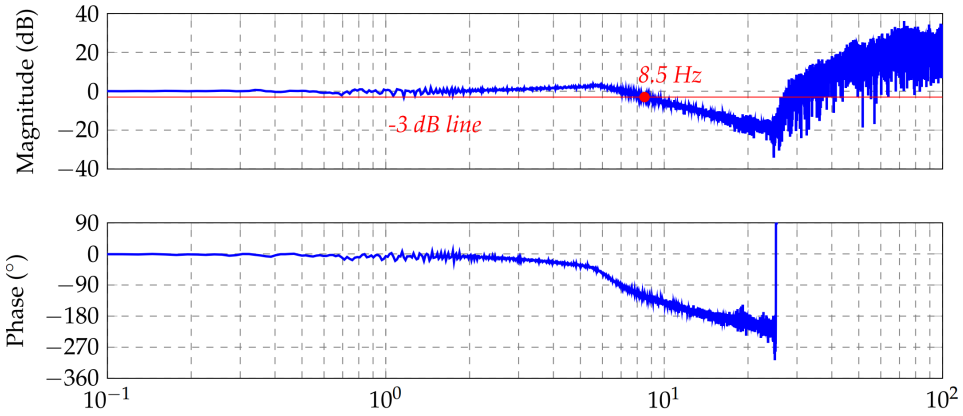


Figure 3.13: Bode plot of the force tracking test with chirp input ($f = 0.1$–$100$ Hz).

### Position Control

Another important performance metric for SEAs is the joint position control performance. It is necessary to precisely follow dynamically changing desired positions with a small overshoot, short settling time, and low steady-state error values. In order to test the system performance on joint position control, I used the position controller presented in Section 3.2.4 with a smooth step input featuring a 0.5 rad step height. I attached a 2.268 kg weight at a 20 cm distance from the joint. Figure 3.14 shows the result of the position control experiment. The system output shows 10% overshoot and 0.35 s settling time for 2% band.

### Impact Detection

SEAs are inherently safer actuators than the rigid actuators due to the elastic element added between the actuator and the output. The elastic element

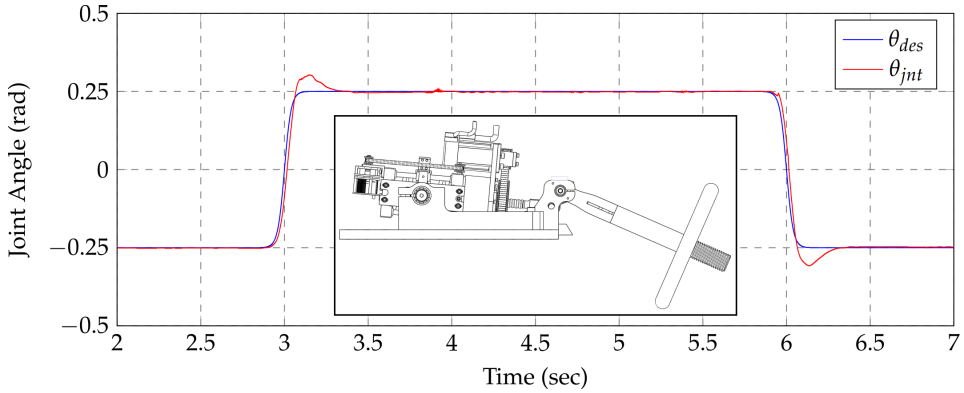


Figure 3.14: High speed joint position tracking with 2.26 kg load located at 0.2 m from the joint.

attenuates the reflected inertia of the rotor and improves safety for the actuator environment while marginally reducing the safety with the possibility of increasing the upper bound of the joint velocity due to the built up kinetic energy on the spring. On the other hand, high-frequency load changes and impact forces are filtered by the elastic element which improves the safety of the actuator itself against mechanical failures in the drivetrain.

The safety level of SEAs can be further improved by using sensing and control approaches. SEAs are very good on providing reliable force feedback. This allows us to quickly recognize unexpected force changes at the output and create reactive control approaches in order to improve safety. Haddadin et al. studied different impact detection and reaction methods in (Haddadin et al. (2008)). The impact detection methods proposed in this study are model-based methods and, thus, require extra measures to cope with possible modeling errors. There are many design aspects affecting the safety of a robot such as joint mass, joint speed, joint stiffness, to name a few. In (De Luca & Flacco

(2012)), the authors further improve the safety of the robot by avoiding the collision in the first place, then use collision detection and reaction methods if the collision is unavoidable. While taking a proper reaction to the impacts is important, the robot or the actuator should be able to distinguish the user collaboration from an impact. In (De Luca & Flacco (2012)), the collaboration phase starts if a collaboration request comes from the user or the robot.

In this study, I used a simple method for distinguishing the collision from collaboration. The controller always monitors the joint angle error and the spring force error and uses a force error threshold for detecting the impact. When the user pushes or holds the output link, the joint angle error increases but since the desired force is regulated according to the joint angle error, the spring force error does not increase. However, when there is an impact, an instantaneous jump on the spring force error level occurs. This method allows the user to safely collaborate with the actuator while monitoring impacts. Figure 3.15 shows the joint angle of the SA-SEA actuator under normal operation, during collaboration, and under impact. The actuator starts with the normal operation and after the first cycle, the user holds the output link and pushes it around. In this phase, the actuator tries to follow the desired joint trajectory. After letting go of the output link, the user holds his hand in the desired joint trajectory. When the impact occurs, the actuator recognizes the impact and responds to it by moving back to the furthest opposite direction possible. I believe that the safest reaction method is to take all the energy out of the output link as quickly as possible. The proper way to do this is by applying

the highest possible torque to the joint in the opposite direction of the motion when the impact occurs. By doing so, all the kinetic energy of the joint link is removed. After this point, switching to gravity compensation mode cancels out the potential energy of the output link and allows it to fully comply to the user's motion. For the sake of demonstrating the quick response of the actuator, I chose to move the output link in the opposite direction in this experiment. The analysis of the experiment result showed that the detection of the impact took 11 ms and the total time from the occurrence of the impact to completely stopping the joint link's motion in the impact direction is 55 ms. The joint rotated 4.29° during this time period.

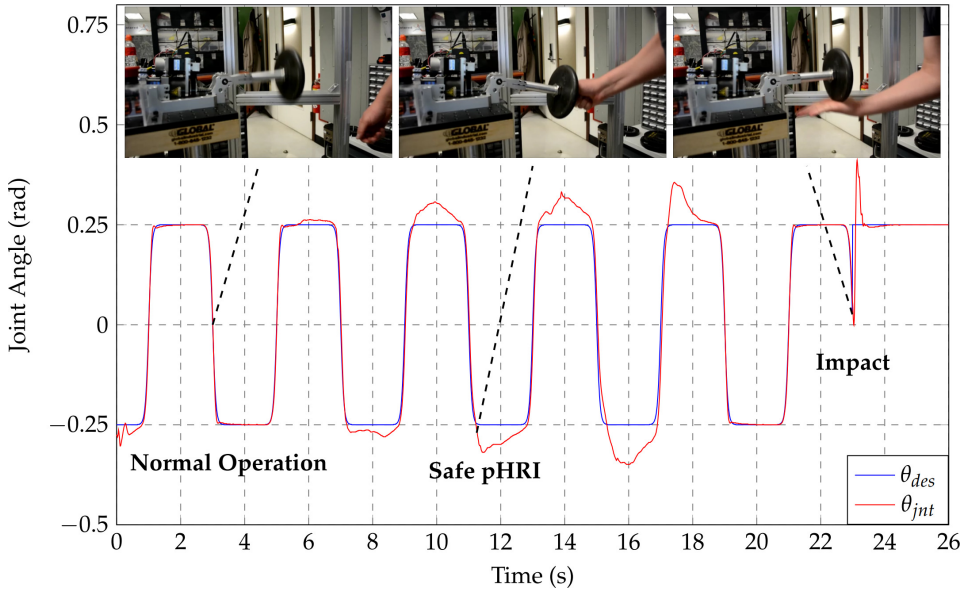


Figure 3.15: Physical human-robot interaction (pHRI) and impact recognition. The experiment starts with position control. The user interacts with the actuator safely and then causes impact at around $t = 23$ s. The actuator quickly moves to safe position in the reverse direction.

The main drawback of this impact detection method is its dependency

on the performance of the force and position control loops. A low-performance controller can easily trigger a safety flag in the system. This can be avoided by setting the threshold values according to the maximum expected force and position errors when there is no impact or user input as long as these values do not pose any danger to the user when impact occurs. It is important to note that this safety check should start after the initial errors at the system startup are phased out.

# Chapter 4

# Optimal Feedback Gain Selection for Series Elastic Actuators

## 4.1 Problem Statement

Gain selection for PID-based SEA controllers is usually difficult. Especially for systems with multiple cascaded control loops, finding the ideal feedback gains to achieve a high control bandwidth requires laborious empirical gain tuning.

SEA controllers, in general, have higher order than rigid actuator's controllers. Therefore, the effect of proportional and derivative gains on the system is less intuitive. It is a common practice to tune the gains of the inner

torque loop for highest bandwidth and use the inner torque loop as a building block for the outer impedance controller. Figure 4.1 shows the cascaded impedance controller of the UT-SEA (Paine et al. (2014)). This impedance controller architecture is used for the development of the gain selection method presented in this chapter.

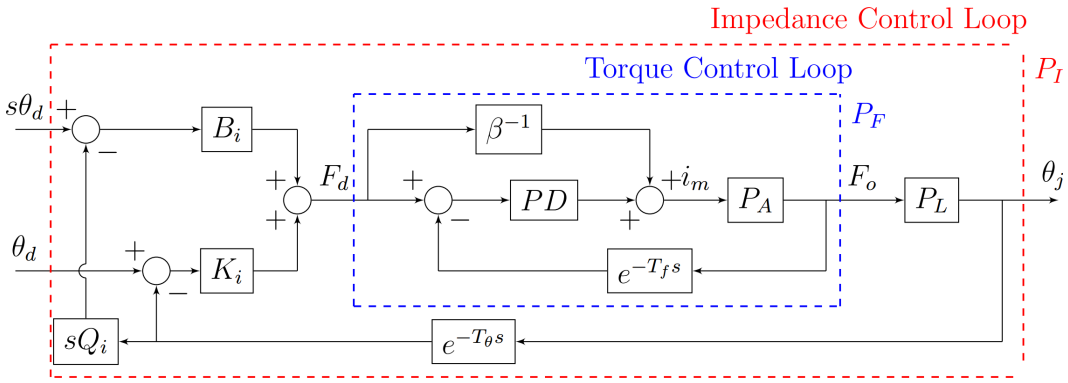


Figure 4.1: The cascaded impedance controller of the UT-SEA.

As was mentioned previously, setting the feedback gains of the torque control loop for highest torque control bandwidth is not the best approach for a high bandwidth impedance controller. Any small change on the torque control gains drastically affects the impedance control behavior. Figure 4.2 shows that while keeping the impedance control feedback gains fixed, increasing the bandwidth of the torque controller increases the impedance controller bandwidth until a certain point but then reduces it. This graph clearly shows that there is an ideal set of feedback gains for the inner and outer control loops which maximize the bandwidth of the impedance controller. The feedback gains for the system used for bandwidth plot in Figure 4.2 are selected according to the critically damped system behavior constraint. More detail on

gain selection procedure is given in Section 4.3.

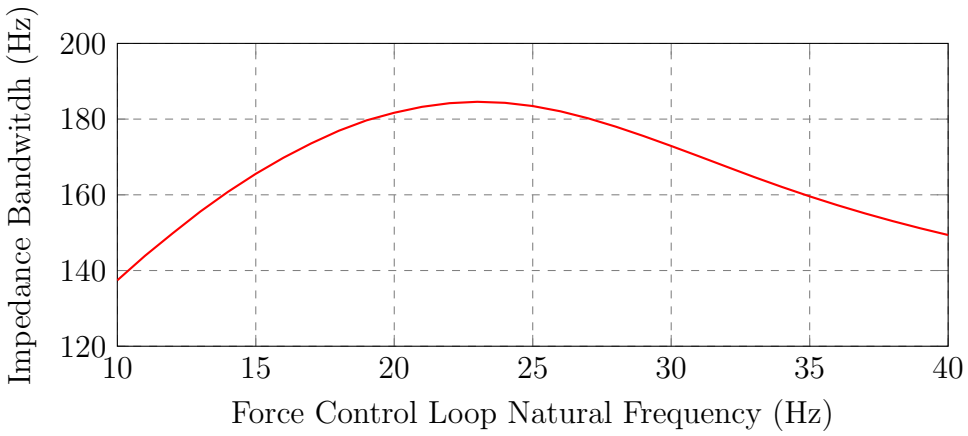


Figure 4.2: The effect of the force controller's bandwidth on the impedance controller's bandwidth.

In this study, the main goal is to find the highest stable feedback gains for time-delayed impedance control for a given desired phase-margin value subject to the constraint that each loop will have gains that produce critically damped behavior.

## 4.2 Modeling of the Actuator

In this section, the model of the nested impedance controller of the UT-SEA with an inner force controller is presented. In order to simplify gain selection for the force controller, I used a high impedance load setup shown in Figure 4.3. Using this model, the relationship between the motor torque acting on the ball-screw mechanism $\tau_m$ and the actuator output force $F_o$ can be written

as,

$$\frac{F_o(s)}{\tau_m(s)} = \frac{k}{m_k s^2 + bs + k} \tag{4.1}$$

where $b$ is the effective viscous friction of the actuator. The motor current $i_m$ and the motor torque are related by,

$$\frac{\tau_m(s)}{i_m(s)} = \beta = \eta N k_\tau \tag{4.2}$$

where $\eta$ is the drivetrain efficiency, $N$ is the speed reduction and $k_\tau$ is the motor torque constant. Combining the equations (4.1) and (4.2), the open-loop force control plant $P_A$ can be written as,

$$P_A = \frac{F_o(s)}{i_m(s)} = \frac{\beta k}{m_k s^2 + bs + k}. \tag{4.3}$$

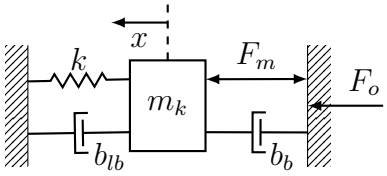


Figure 4.3: Simplified model of the SEA with high impedance load setup. $m_k$ is the total sprung mass of the actuator, $k$ is the effective spring stiffness, $b_{lb}$ is viscous friction at the linear ball bearings supporting the spring cage, $F_m$ is the motor force, $b_b$ is the viscous back-drive friction of the ball-screw mechanism and $F_o$ is the output force.

The closed-loop force control plant $P_F$ is

$$P_F = \frac{F_o(s)}{F_d(s)} = \frac{P_A(C + \beta^{-1})}{1 + P_A C e^{-T_f s}} \tag{4.4}$$

where $C = B_f Q_f s + K_f$ is the PD-type controller plant with damping ($B_f$) and stiffness ($K_f$) gains, $e^{-T_i s}$ is the force feedback time-delay and $Q_f$ is a first order derivative filter in following form,

$$Q_f = \frac{2\pi f_f}{s + 2\pi f_f} \tag{4.5}$$

where $f_f$ is the filter cut-off frequency.

The expanded closed-loop force control plant transfer function is

$$\frac{F_o(s)}{F_d(s)} = \frac{(k/m)(B_f Q_f \beta s + K_f \beta + 1)}{s^2 + ((B_f Q_f \beta k e^{-T_f s} + b)/m)s + (K_f \beta k e^{-T_f s} + k)/m}. \tag{4.6}$$

The load plant $P_L$ can be modeled as,

$$P_L = \frac{\theta_j(s)}{F_o(s)} = \frac{1}{I_j s^2 + b_j s} \tag{4.7}$$

where $I_j$ is the load inertia and $b_j$ is the viscous joint friction.

Combining equations (4.4) and (4.7) and considering the impedance control architecture given in Figure 4.1, the closed-loop transfer function of the impedance control system can be written as,

$$P_I = \frac{\theta_j(s)}{\theta_d(s)} = \frac{P_F P_L (B_i s + K_i)}{1 + P_F P_L (B Q_i s + K) e^{-T_i s}} \tag{4.8}$$

where $B_i$ is the impedance damping gain, $K_i$ is the impedance stiffness gain, $Q_i$ is a first order derivative filter similar to $Q_f$ and $e^{-T_i s}$ is the impedance loop feedback time-delay.

The expanded closed-loop impedance control transfer function is

$$P_I = \frac{\theta_j(s)}{\theta_d(s)} = \frac{(k/mI_j)(B_f Q_f \beta s + K_f \beta + 1)(B_i s + K_i)}{\sum_{i=0}^{4} D_i s^i} \tag{4.9}$$

with denominator coefficients:

$$D_4 = 1$$
$$D_3 = (B_f Q_f I_j \beta k e^{-T_f s} + b_j m + I_j b)/(mI_j)$$
$$D_2 = (B_f B_i Q_f Q_i \beta k e^{-T_i s} + B_f Q_f b_j \beta k e^{-T_f s} + K_f I_j \beta k e^{-T_f s} + b_j b + I_j k)/(mI_j)$$
$$D_1 = (F_f Q_f K_i \beta k e^{-T_i s} + K_f B_i Q_i \beta k e^{-T_i s} + K_f b_j \beta k e^{-T_f s} + B_i Q_i k e^{-T_i s} + b_j k)/(mI_j)$$
$$D_0 = (K_f K_i \beta k e^{-T_i s} + K_i k e^{-T_i s})/(mI_j)$$

Each derivative filter in equations (4.6) and (4.9) increase the order of these systems by one. They are not expanded in the equations as they are going to be ignored during the process of creating gain selection equations. This way, the order of the force and impedance control systems are limited to be second and fourth order, respectively. The equations also possess zeros in the numerators. The zeros are going to shorten the rise time of the systems and cause overshoot. Since they do not affect the stability of the system, we will mainly focus on the characteristic equations during the gain selection process.

## 4.3 Methodology

In this section, the feedback gain selection method for a critically damped fourth order impedance controller is presented. Using this method, the highest stable feedback gains for a desired phase-margin can be selected in order to achieve a high impedance control bandwidth. The proposed method can also be used to find the set of force and impedance control feedback gains to achieve the highest possible phase-margin. There are two key aspects of the gain selection method which are the critically-damped output constraints for the idealized (no time-delay and no derivative filter) inner and outer control loops and the phase-margin criterion for the non-idealized (with time-delay and derivative filter) outer loop. We construct the gain selection method using these important tools.

### 4.3.1 Critically Damped System Response Constraint

The critically damped response constraint is used for two main reasons. In terms of performance, a critically damped system response is desirable because it gives a near-minimum settling time with no overshoot, both of which are important criteria for robotic applications. Another important benefit of a critically damped system response criterion is that it reduces the gain search dimensions from two to one by relating the damping and stiffness gains via the system's natural frequency.

There exists a well-established gain selection method for a critically damped second order system. I use this method and find the force control

feedback gains by comparing the characteristic equation of Equation (4.6) and the characteristic equation of a typical second order system transfer function,

$$s^2 + 2\zeta\omega_n s + \omega_n^2. \tag{4.10}$$

Note that the time-delay and derivative signal filtering are ignored during the gain selection for force and impedance controllers. Therefore, the pole locations of the non-idealized system are not necessarily critically damped. This approach will be justified in Section 4.4.

Gain selection for high order systems is challenging. Therefore, high order systems are usually represented as multiplication of first and second order systems. Using this approach, we represent the fourth order impedance control system as multiplication of two second order systems (Petit & Albu-Schäffer (2011)),

$$(s^2 + 2\zeta_1\omega_{n_1} s + \omega_{n_1}^2)(s^2 + 2\zeta_2\omega_{n_2} s + \omega_{n_2}^2). \tag{4.11}$$

By using the same damping ratio $\zeta$ and natural frequency $\omega_n$ values in Equation (4.11), the number of necessary parameters for gain selection can be reduced to two.

By comparing the coefficients of the denominator of equations (4.9) and (4.11), we have following set of equations,

$$
\begin{aligned}
\frac{B_f I_j \beta k + b_j m + I_j b}{m I_j} &= 4\zeta\omega_n, \\
\frac{B_f B_i \beta k + B_f b_j \beta k + K_f I_j \beta k + b_j b + I_j k}{m I_j} &= 4\zeta^2\omega_n^2 + 2\omega_n^2, \\
\frac{B_f K_i \beta k + K_f B_i \beta k + K_f b_j \beta k + B_i k + b_j k}{m I_j} &= 4\zeta\omega_n^3, \\
\frac{K_f K_i \beta k + K_i k}{m I_j} &= \omega_n^4.
\end{aligned}
\tag{4.12}
$$

Force control damping gain $B_f$ and stiffness gain $K_f$ have been selected by using the equations (4.4) and (4.10). In Equation (4.12), impedance control damping gain $B_i$ and stiffness gain $K_i$ can be selected for desired $\zeta$ and $\omega_n$ values by using the second and third equations. In this study, we set $\zeta$ equal to one for a critically damped response.

In (Zhao et al. (2014)), the author uses two multiplied second order system method for selecting both inner torque and outer impedance gains at the same time for a critically damped impedance response. Even though this method allows users to find feedback gains for a critically damped impedance response, it does not employ the potential benefit of independent gain scaling of inner and outer loops and does not provide information about the stability level of the inner force control loop.

### 4.3.2 Phase-Margin Criterion

Stability is an important concern when selecting the feedback gains for a control system. The stability of the system can be checked or measured by using

methods such as passivity, phase-margin and Routh-Hurwitz stability criterion. In this study, I use phase-margin stability criterion which provides a good balance between the passivity method which guarantees stability but compromises on the performance and Routh-Hurwitz method which tells whether the system is stable or not without providing any information on how stable the system is. The gain selection method proposed in this dissertation is developed to find the highest feedback gains for a desired phase-margin value.

### 4.3.3 The Algorithm

The gain selection process starts with constructing the second order transfer function of the inner force control loop by ignoring the time-delay and derivative filtering and preparing the damping and stiffness gain equations for a critically damped force control. The next step is to construct the fourth order transfer function of the impedance control loop by ignoring the time-delay and derivative filtering and solve for the impedance PD controller gains which produce (very close to) critically damped behavior. The feedback gains for force and impedance control loops will depend on the nominal natural frequency of the inner loop, and the nominal natural frequency of the outer loop. The damping ratio mentioned before as the second parameter necessary to find the outer loop gains is taken to be unity, and thus reflects a critically damped desired behavior.

After constructing the feedback gain selection equations, the next step is running a natural frequency sweep in a range of natural frequencies both for

force and impedance control loops. During this sweep, the open-loop transfer function of the impedance controller with time-delay and derivative filtering is used and the phase-margins are calculated using the `margin` function of MATLAB. As a result, a phase-margin surface is created similar to Figure 4.4.

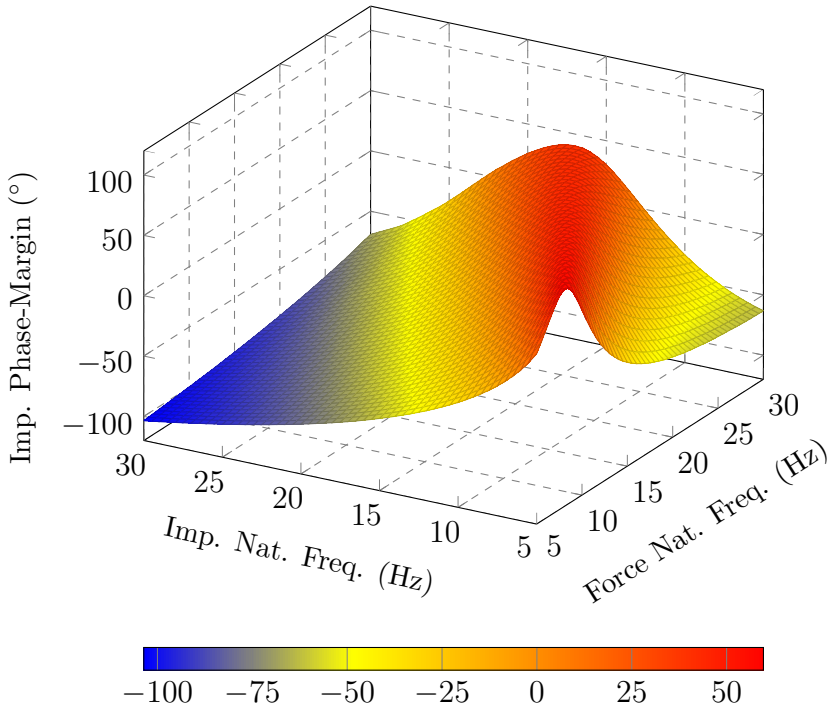


Figure 4.4: Phase-margin surface.

Figure 4.4 shows the phase-margin values of the impedance controller for force and impedance control natural frequencies ranging from 5 to 30 Hz.

The next step is selecting the points where the phase-margin is higher than the desired value. Among these points, the one with the highest natural frequency pair will give the highest feedback gains for the desired phase-margin while maintaining a critically damped system output. The selection can be

visualized as shown in Fig. 4.5

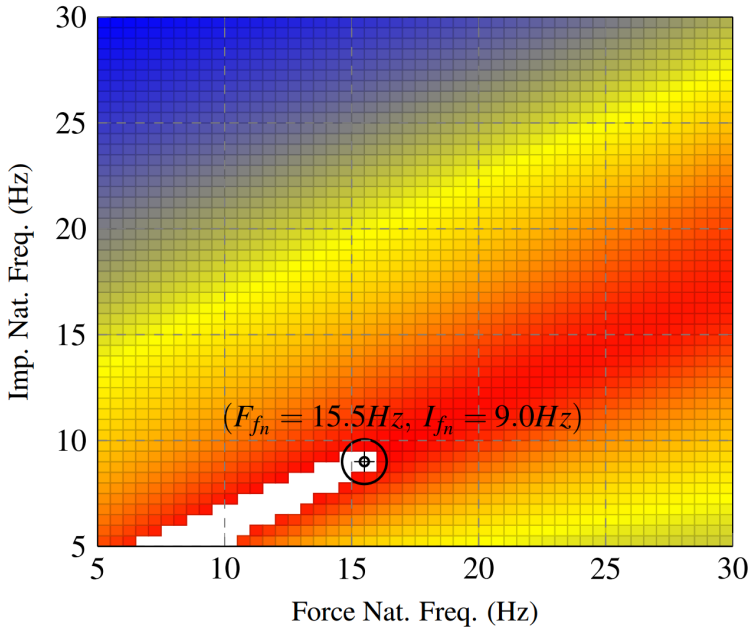


Figure 4.5: Phase-margin surface (top view).

The white area on Figure 4.5 shows the points where the phase-margin of the impedance controller is above 50° . For this particular example, the highest natural frequency pair in the white area are $\omega_{n_f} = 15.5$ Hz and $\omega_{n_i} = 9$ Hz. It should be noted that a higher resolution frequency sweep can be performed in the vicinity of target area shown in Figure 4.5 to refine this coarse estimate. The corresponding feedback gains for the selected natural frequencies can be calculated by using the gain selection equations which are constructed in previous steps. Figure 4.6 shows the step response of the impedance controller for the feedback gains selected by using the proposed method.

A slight overshoot (1.2%) is observed on the output which is caused by the zeros in the transfer function. This overshoot can be further reduced

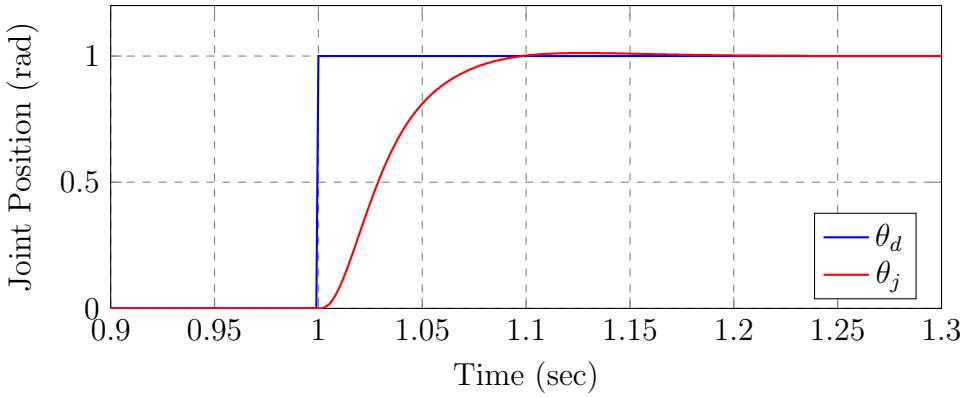


Figure 4.6: Impedance controller step response for selected feedback gains.

by increasing the damping ratio of the impedance controller $\zeta$ or completely eliminated by using zero cancellation methods.

The gain selection procedure can be summarized as in Algorithm 1. This algorithm automates this procedure and selects the highest natural frequencies, thus the highest feedback gains, without visual observation.

## 4.4 Justification of the Method

In the proposed method, the equations of feedback gains are constructed by ignoring the time-delay and derivative filters in the transfer functions and these equations are used to find the feedback gains for the system with time-delay and derivative filters. This approach raises the question of whether it indeed allows the user to find the highest gains. This question can be addressed using the Figure 4.7.

In this figure, the upper surface is the phase-margin surface for the system with no time-delay and derivative filters, and the lower surface is the

**Algorithm 1** Gain Selection Algorithm

initializations
**for** $i$ in range $N_f$ **do**
  **for** $j$ in range $N_i$ **do**
    $\omega_{n_F} = \text{linspace}(\omega_{n_{F_{min}}}, \omega_{n_{F_{max}}}, N_f)(i)$
    $\omega_{n_I} = \text{linspace}(\omega_{n_{I_{min}}}, \omega_{n_{I_{max}}}, N_i)(j)$
    Calculate $B_f(\omega_{n_F})$ and $K_f(\omega_{n_F})$
    Calculate $B_i(\omega_{n_I})$ and $K_i(\omega_{n_I})$
    $PM[i,j] = margin(P_I(B_f, K_f, B_i, K_i))$
    **if** $PM(i,j) \geq PM_{des}$ **then**
      **if** $\omega_{n_F} \cdot \omega_{n_I} > max_{\omega_{n_F} \cdot \omega_{n_I}}$ **then**
        $max_{\omega_{n_F} \cdot \omega_{n_I}} = \omega_{n_F} \cdot \omega_{n_I}$
        $\omega_{n_{F_{select}}} = \omega_{n_F}$
        $\omega_{n_{I_{select}}} = \omega_{n_I}$
      **end if**
    **end if**
  **end for**
**end for**
Calculate $B_f(\omega_{n_{F_{select}}})$ and $K_f(\omega_{n_{F_{select}}})$
Calculate $B_i(\omega_{n_{I_{select}}})$ and $K_i(\omega_{n_{I_{select}}})$

phase-margin surface for the system with time-delay and derivative filters. If we draw imaginary lines at the ridges of these surfaces, we find the highest phase-margins for given force control loop or impedance control loop frequency. Figure 4.8 shows the top view of the Figure 4.7. The fact that these lines are close to each other shows that the gains which give the highest phase-margin for the system with no time-delay and derivative filtering indeed give the highest or near highest phase-margin for the system with time-delay and derivative filters.

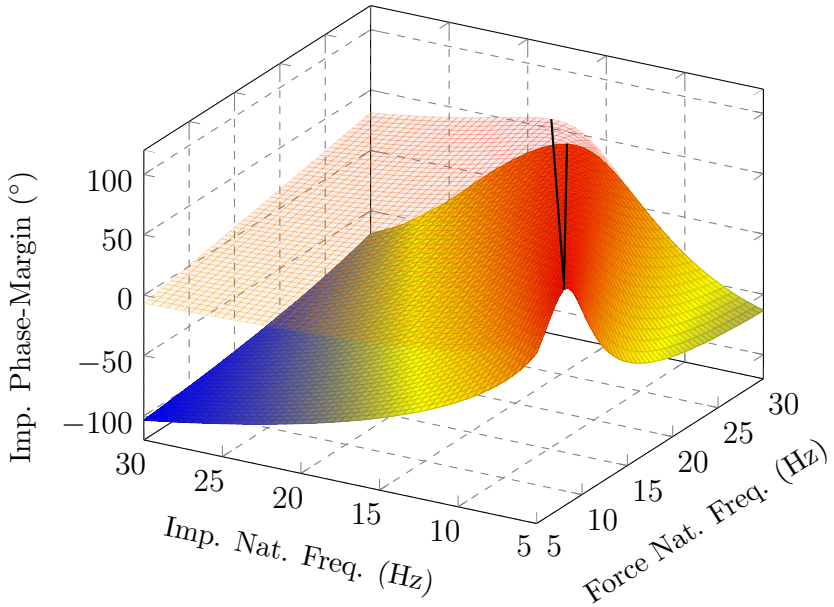


Figure 4.7: Phase margin surfaces for system with time-delay and derivative filters (lower) and without time-delay and derivative filters (upper).

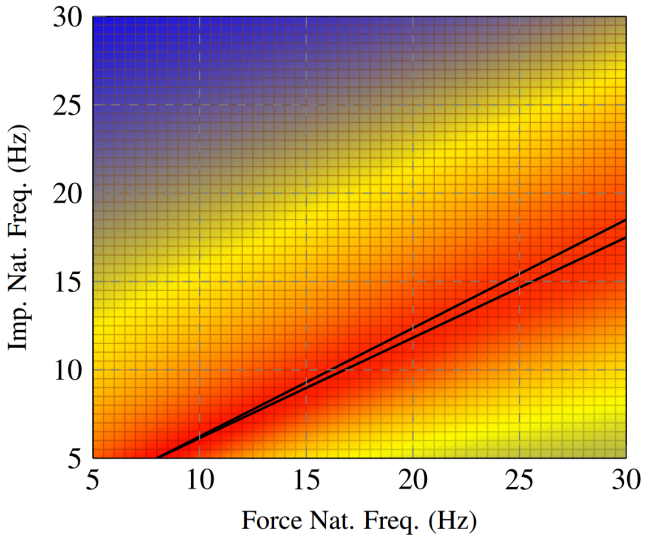


Figure 4.8: Method justification plot (top view).

## 4.5 The Effect of System Parameters on Impedance Bandwidth

Time-delay and derivative signal filtering have major effect on the bandwidth of impedance controllers (Colgate & Brown (1994)). In this section, we analyze the effects of these real life performance limiting factors on impedance control bandwidth. We also analyze the effect of load mass on the impedance behavior.

### 4.5.1 Time-Delay and Derivative Filtering Effect

Impedance control regulates the dynamic interaction between the robot and its environment. Conventionally, the mechanical impedance is defined as the mapping of a velocity input to a force output at the interaction port of a system with its environment: $Z(s) = F(s)/sX(s)$. If we use the conventional definition of the impedance, the transfer function between the joint velocity and joint torque can be written as,

$$Z_I = -\frac{F_o(s)}{s\theta_j(s)} = \frac{\sum_{i=0}^{2} N_i s^i}{\sum_{j=0}^{3} D_j s^j} \tag{4.13}$$

where

$N_2 = \beta k B_f B_i Q_f Q_i e^{-T_i s}$,
$N_1 = k(\beta B_f K_i Q_f + B_i(1 + \beta K_f)Q_i)e^{-T_i s}$,
$N_0 = k(1 + \beta K_f)K_i e^{-T_i s}$,

and

$$D_3 = m,$$
$$D_2 = b + \beta k B_f Q_f e^{-T_f s},$$
$$D_1 = k + \beta k K_f e^{-T_f s}$$
$$D_0 = 0.$$

The numerator and the denominator of the Equation (4.13) are second and third order, respectively. When the derivative filters $Q_f$ and $Q_i$ are expanded, the denominator of the impedance transfer function becomes five. This is due to the selected impedance control architecture.

It is beneficial to analyze the frequency response of the time-delay and derivative filters in order to understand how the overall system behaves under their influence. At low frequencies, both the filter and the time-delay transfer functions approach to unity:

$$\lim_{\omega \to 0} \; e^{-t_d j\omega} = 1 \tag{4.14}$$

$$\lim_{\omega \to 0} \; \frac{2\pi f_{c.o.}}{j\omega + 2\pi f_{c.o.}} = 1 \tag{4.15}$$

where $t_d$ is time-delay constant in seconds and $f_{c.o.}$ is the cut-off frequency of the first order derivative filter. Therefore, derivative filter and time-delay does

not affect the system impedance as the frequency approaches to zero. In this region of frequency, the impedance transfer function given in the Equation (4.13) can be analyzed with:

$$\lim_{\omega \to 0} \frac{N_0}{j\omega \ D_1} = \frac{k(1+\beta K_f)K_i}{j\omega(k+\beta k K_f)} = \frac{K_i}{j\omega} \tag{4.16}$$

As expected, the Bode plot on Figure 4.9 shows the convergence to virtual stiffness line ($K_i/j\omega$). The Bode plots of the systems with and without time-delay and derivative filters converge to different virtual stiffness lines because the proposed method selects the impedance stiffness feedback gain (along with other gains) according to the given properties of the system and the desired phase-margin. All of the systems shown on Figure 4.9 satisfy a 60° phase-margin requirement.

At high frequencies, the time-delay and and derivative filter terms approach to zero. The impedance behavior of the system as the frequency approaches to infinity will depend on each terms speed on approaching their asymptotes. The expected slope of the magnitude is -60 dB/decade since the order of the denominator of the impedance transfer function becomes 5 when the filter terms are expanded whereas the order of the numerator stays at 2. When the filters are disregarded, both the order of the numerator and the denominator stays the same and therefore, the expected slope is -20 dB/decade. Figure 4.9 shows the effect of the time-delay and derivative filtering on the frequency response of the impedance controller.

Impedance controllers are more sensitive to time-delay in the position

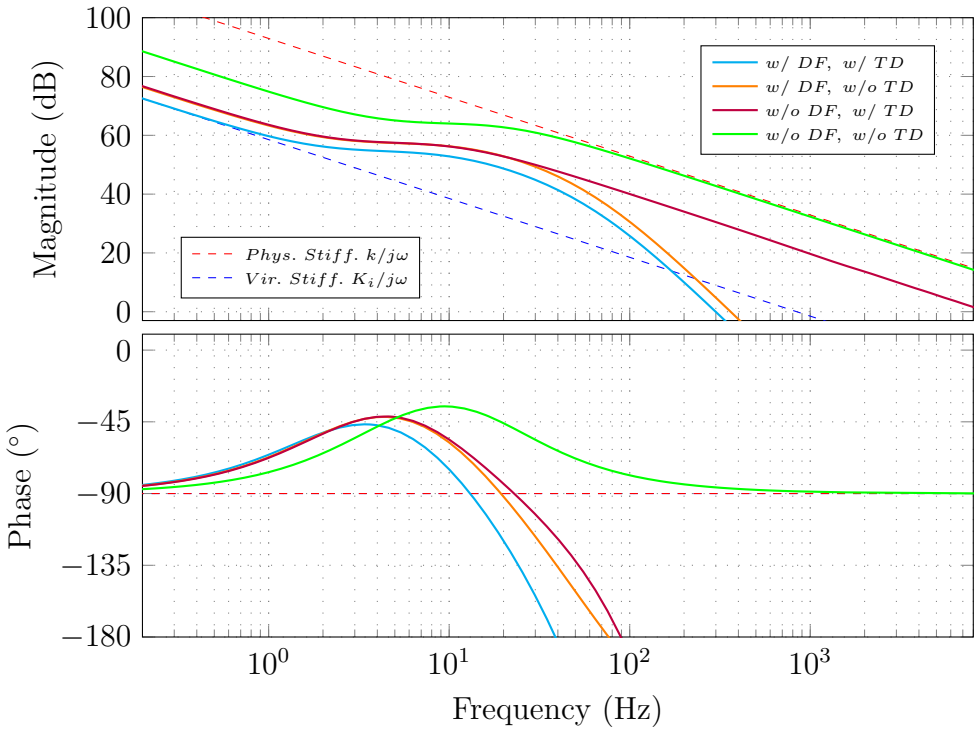


Figure 4.9: Comparison of various cases on impedance behavior of the system.

feedback path than in the force feedback path (Zhao et al. (2014)). It is more likely to have longer time-delays on the impedance control loops than the force controller since the force control is usually performed at embedded level whereas the impedance control mainly performed at high level controllers. Figure 4.10 shows the dependency of position control bandwidth on the position feedback path time-delay while keeping the force control loop time-delay fixed at $T_i = 0.5\ ms$.

Previous work on time-delay sensitivity shows that increasing the time-delay reduces the stability region of the impedance controllers (Colgate & Brown (1994); Zhao et al. (2014); Focchi et al. (2016)). (Zhao et al. (2014))

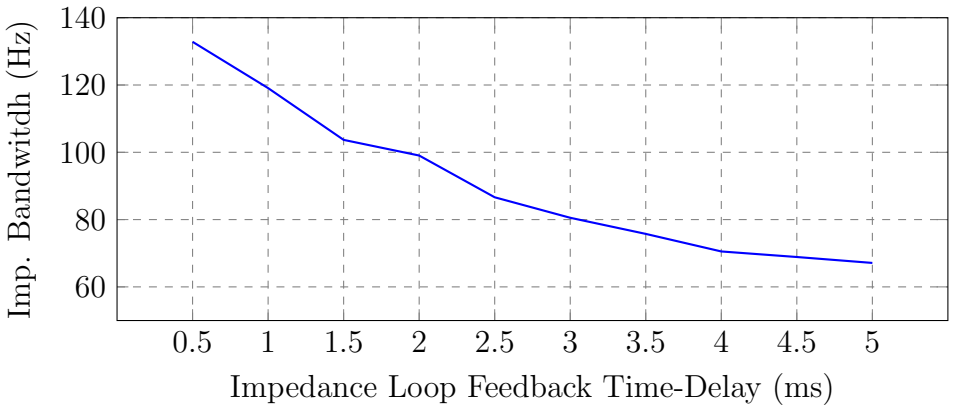


Figure 4.10: The effect of impedance control feedback time-delay on the impedance controller's bandwidth.

show that the overshoot in the system response increases when the time-delay values are increased. The proposed method in this dissertation automatically selects the feedback gains for the desired phase-margin. Therefore, increasing the time-delay in the system does not increase the overshoot. As the time-delay increases, the stable gains for the desired phase-margin are automatically decreased. Figure 4.11 shows the impedance control time-delay effect on the step response. As the time-delay increases, the automatically selected feedback gains decrease and undesirable overshoot is prevented. However, the settling time of the system increases.

Figure 4.12 shows how increasing impedance control feedback time-delay affects the impedance bandwidth. At low frequencies, the system behaves like a virtual spring and converges to the virtual stiffness asymptote of its respective impedance stiffness feedback gain. At high frequencies, the system still behaves like the physical spring but with a scaling factor.

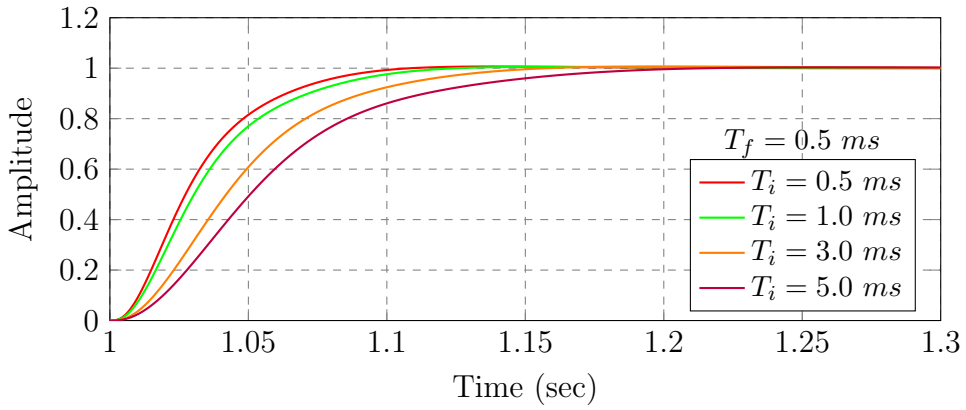


Figure 4.11: The effect of impedance control feedback time-delay on step response.

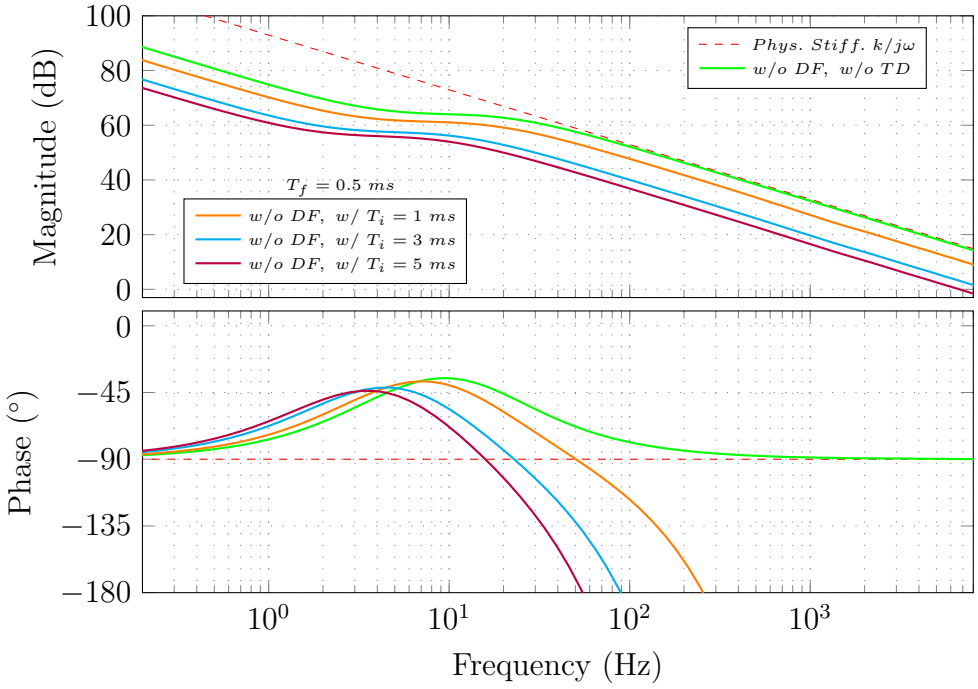


Figure 4.12: Time-delay effect on impedance response.

Derivative filtering has a more drastic effect on the impedance response of the system at high frequencies. Figure 4.13 shows that as the cut-off fre-

quencies of the force and impedance control loop derivative filters reduced, the bandwidth of the system impedance drastically reduces. The selected system architecture also contributes to this result. During the simulations of different impedance control architectures, I observed that using the classical PD control architecture for both the inner and outer loops improves the impedance bandwidth. However, the selected control architecture gives a much better result on position control which is a crucial control aspect for actuators and robotic applications.

All the examples given in the impedance Bode plots were created by selecting the appropriate gains for a 60° phase margin. The impedance bandwidth can be increased by compromising on the stability level. Lower desired phase-margin value will allow the algorithm to select higher feedback gains.

The results shown on the Bode plots of this study may seem surprising in the robotics community. Previous studies on the impedance response of SEAs show that at high frequencies, SEAs behave as physical springs. The main reason why our results show different behavior is the fact that this study was made on the model of a reaction force sensing series elastic actuator (RF-SEA) where the spring is located between the ground and the actuator body. This structure makes the actuator behave like a mass-spring-damper at high frequencies.

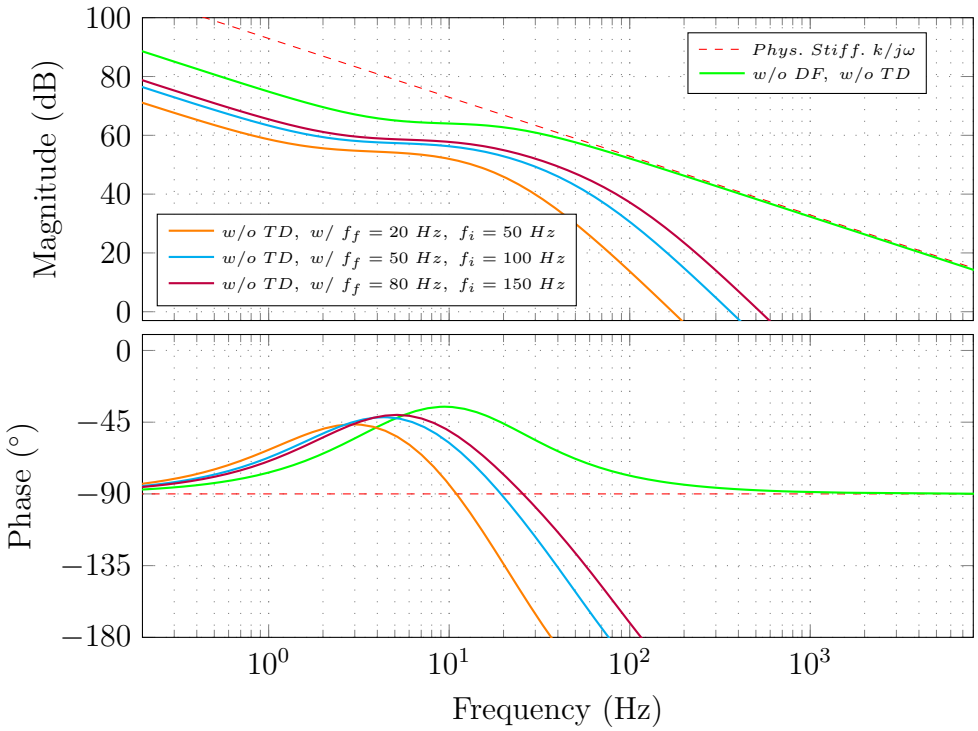


Figure 4.13: Derivative filtering effect on impedance response.

### 4.5.2 The Effect of Load Mass

The impedance transfer function given with the Equation (4.13) shows the relationship between the velocity input from the load side and force output of the actuator. It defines how much force we would feel if we move the actuator output with a certain velocity. In robotic systems, there always exists a load at the actuator output. For a single motor, the minimum load is the inertia of the rotor, for a single-DOF actuator, the mass of the linkage and for an actuator on a robotic arm, the mass of all the distal joints and the links define the minimum load.

When the actuator output is moved, the impedance felt by the envi-

ronment depends on multiple parameters. The effect of the time-delay and derivative filtering on the impedance behavior were analyzed in the previous section. The load mass attached to the output of the actuator also affects the actuator impedance behavior and this behavior depends on the frequency of the applied input velocity at the output. The impedance transfer function including the load mass can be written as,

$$Z_L = Z_I + I_j s \tag{4.17}$$

where $Z_I$ is given with the Equation (4.13).

It was shown that $Z_I(j\omega)$ converges to the virtual stiffness at low frequencies in Section 4.5.1. The added load mass does not affect this convergence at low frequencies. However, at high frequencies, the load mass has a major effect on the impedance behavior. Analysis of the Equation (4.17) at high frequencies,

$$\lim_{\omega \to +\infty} \left(Z_I(j\omega) + I_j \cdot j\omega\right) = I_j \cdot j\omega \tag{4.18}$$

shows that the actuator impedance seen from the environment converges to a pure mass at high frequencies. Figure 4.14 shows the Bode plot of the impedance behavior of the actuator with different load masses.

In Figure 4.14, the effect of load mass is shown on a system with no time-delay and no derivative filtering. Figure 4.15 shows the effect of added load mass on a system with time-delay and derivative filtering. As expected, at high frequencies, the system behaves as a pure mass. However, the negative effect

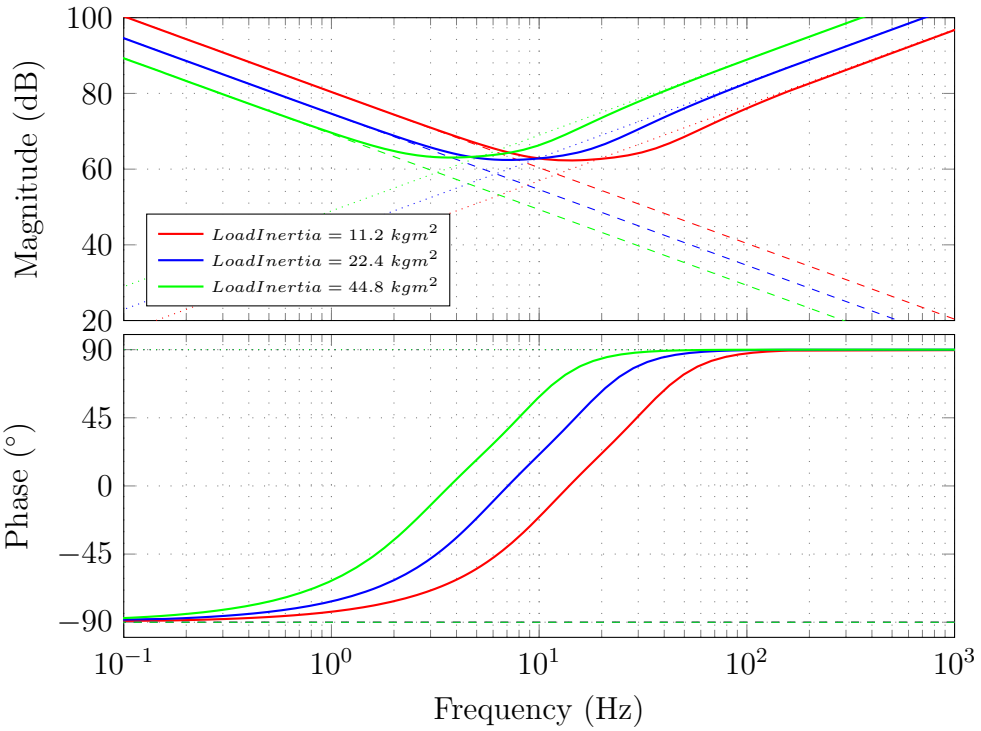


Figure 4.14: Load mass effect on impedance response (No time-delay, no derivative filtering). Dashed lines show the asymptotes of the virtual stiffnesses and dotted lines show the load asymptotes.

of the derivative filtering and time-delay can be observed at low frequencies.

## 4.6 Experiments

The proposed gain selection method significantly reduces the time and effort that spent on gain selection procedure for the cascaded PD-type controllers. Once the phase-margin surface is created by using the system parameters, the highest feedback gains for the desired phase-margin can easily be selected. Since it is a simple procedure to implement the proposed method, I applied it

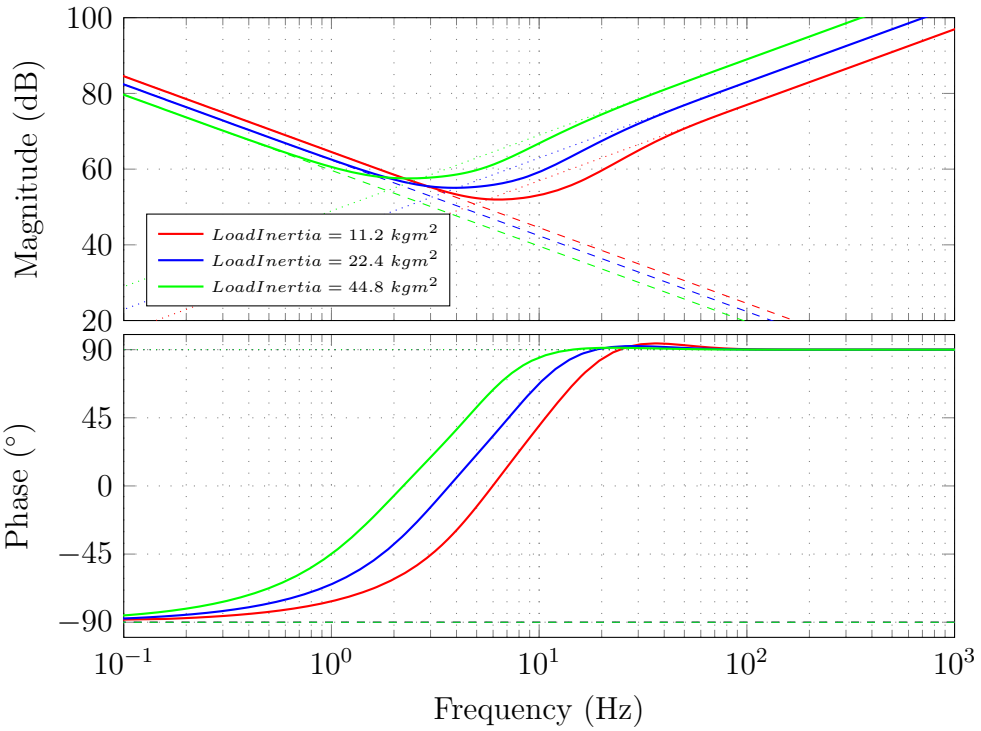


Figure 4.15: Load mass effect on impedance response ($T_f = T_i = 0.5$ ms, $f_f = 100$ Hz, $f_i = 50$ Hz).

to multiple SEAs. The results presented in this section proves the functionality of the proposed concept and validate the proposed method.

The model used in this study is a linear model. The load is also modeled to be moving linearly. However, the SEAs we have in Human Centered Robotics Laboratory have nonlinear kinematic structures. In order to overcome the possible issues due to the nonlinearity in the joint mechanism, I calculated the nominal moment arm length when the load arm is parallel to the ground and implemented the frequency response and step response tests around this point. Also, I used gravity compensation in order to reduce the

effect of the nonlinearity in joint mechanism.

### 4.6.1 Experiments on the UT-SEA

The proposed feedback gain selection method is explained by using the model of the UT-SEA. Therefore, in order to test the applicability of the proposed methodology on a real hardware, I implemented step and frequency response experiments on the UT-SEA. Using the procedure explained in Section 4.3 and the system parameters given in Table 4.1, I created the phase-margin surface for the UT-SEA. Table 4.2 shows the automatically calculated feedback gains for the desired phase-margin values. I directly used these calculated feedback gains without any adjustments.

Table 4.1: Actuator and load parameters of the UT-SEA.

| **Parameter** | **Value** |
|---|---|
| $m$ | 360 kg |
| $b$ | 2200 Ns/m$^2$ |
| $k$ | 350000 N/m |
| $I_j$ | 22.4 kg |
| $b_j$ | 160 Ns/m$^2$ |

Figure 4.16 shows the step response of the actuator for the desired phase-margins. This experimental result clearly shows that phase-margin dependent automatic gain selection algorithm works as expected. Reducing the phase-margin reduces the rise time but causes overshoot. High phase-margin reduces the overshoot but settling time increases. With the selected feedback gains for the phase-margin value 55°, the actuator is unable to prevent

Table 4.2: Automatically selected feedback gains for the UT-SEA. $f_f$ and $f_i$ are the natural frequencies of the force and impedance control loops, respectively. The units of the feedback gains are: $K_f$ (A/Nm), $B_f$ (As/Nm), $K_i$ (Nm/rad) and $B_i$ (Nms/rad).

| **Phase-Margin** | $f_f$ (Hz) | $f_i$ (Hz) | $K_f$ | $B_f$ | $K_i$ | $B_i$ |
|---|---|---|---|---|---|---|
| 55° | 11.6 | 6.8 | 0.021 | 0.0007 | $0.737 \times 10^3$ | $1.589 \times 10^4$ |
| 50° | 16.0 | 9.5 | 0.045 | 0.0009 | $1.130 \times 10^3$ | $3.086 \times 10^4$ |
| 45° | 22.4 | 13.0 | 0.093 | 0.0014 | $1.481 \times 10^3$ | $5.924 \times 10^4$ |
| 40° | 30.3 | 17.4 | 0.174 | 0.0019 | $1.958 \times 10^3$ | $1.076 \times 10^5$ |

steady-state error.

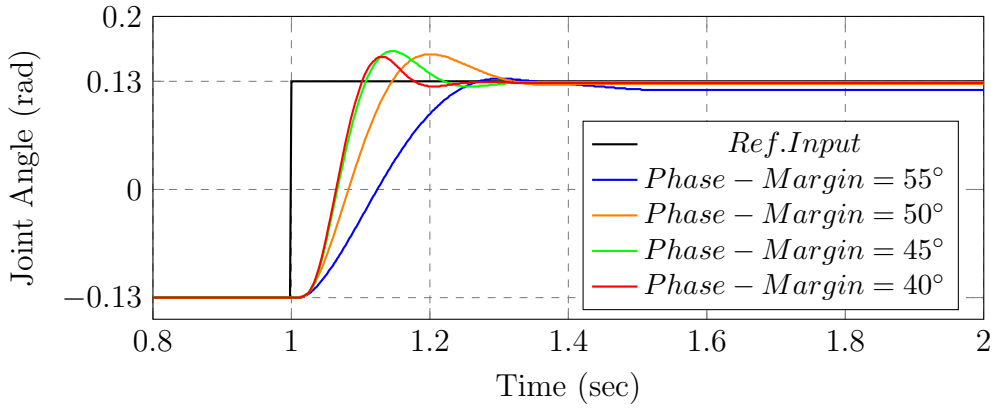


Figure 4.16: Joint position step responses with the automatically selected feedback gains for the UT-SEA.

The main goal of the proposed gain selection method is to increase the bandwidth of the impedance controllers. In order to see the effectiveness of the gain selection method on the impedance bandwidth, I implemented frequency response experiments on the UT-SEA. Figure 4.17 shows the results of these experiments.

As expected, the automatically selected feedback gains for the decreas-

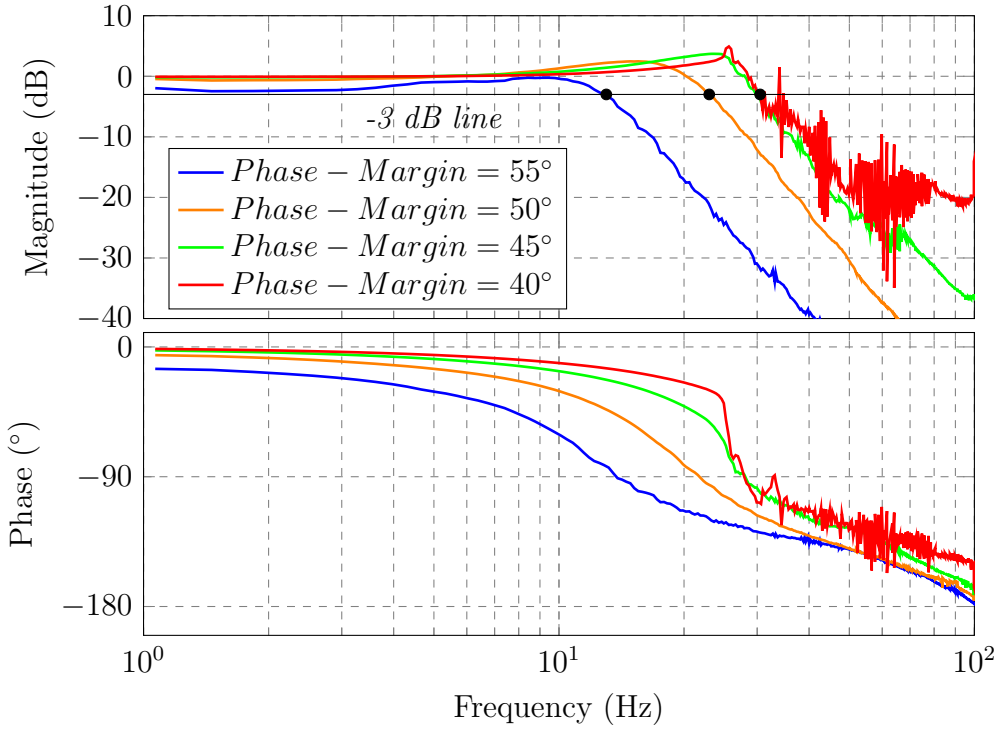


Figure 4.17: Bode plots of the gain selection experiments on the UT-SEA.

ing phase-margins increase the bandwidth of the impedance controller. These results show that, once the phase-margin surface is created for the actuator, the time and effort spent on feedback gain selection can be drastically reduces by using this gain selection approach. Using the proposed gain selection method, I was able achieve 30 Hz bandwidth on the impedance controller of the UT-SEA which has never been achieved before. The highest impedance control bandwidth reported so far about the UT-SEA is below 11 Hz (Zhao et al. (2014)).

### 4.6.2 Experiments on the SA-SEA

After proving the concept on the UT-SEA, I applied the proposed method to the SA-SEA in order to show the reproducibility of this method. After creating the phase-margin surface, natural frequencies of the inner and outer loops are selected according to multiple desired phase-margin values. After this step, the corresponding feedback gains are calculated with the formulated gain selection equations. Table 4.3 shows the calculated feedback gains for selected phase-margin values. Since the servo motor on the SA-SEA is modeled as a torque source and conversions from desired actuator force to desired motor torque handled in the code, the force feedback gains are unitless. Similarly, the desired joint torque to desired spring force conversion for the gravity compensation is handled in the code. Therefore, the feedback gains for the impedance control loop are also unitless.

Table 4.3: Automatically selected feedback gains for the SA-SEA. $f_f$ and $f_i$ are the natural frequencies of the force and impedance control loops, respectively. The gains are unitless.

| **Phase-Margin** | $f_f$ (Hz) | $f_i$ (Hz) | $K_f$ | $B_f$ | $K_i$ | $B_i$ |
|---|---|---|---|---|---|---|
| 65° | 8.6 | 5.2 | 1.012 | 0.056 | 1.934 | 56.359 |
| 60° | 10.4 | 6.3 | 1.942 | 0.071 | 2.448 | 67.772 |
| 55° | 13.0 | 8.2 | 4.181 | 0.101 | 3.065 | 93.217 |
| 50° | 18.6 | 10.9 | 8.412 | 0.142 | 3.993 | 146.181 |
| 45° | 24.9 | 14.3 | 15.869 | 0.197 | 4.985 | 240.112 |

Using the feedback gains shown on Table 4.3, I performed step response tests on the SA-SEA. The results for 65°, 55° and 45° phase-margins are shown on Figure 4.18. The plots on this graph confirm that reducing the

desired phase-margin value allows higher feedback gains but results in more oscillatory behavior. This experiment is the first step to check the correctness of the proposed approach and to check the stability of the system for the selected feedback gains.

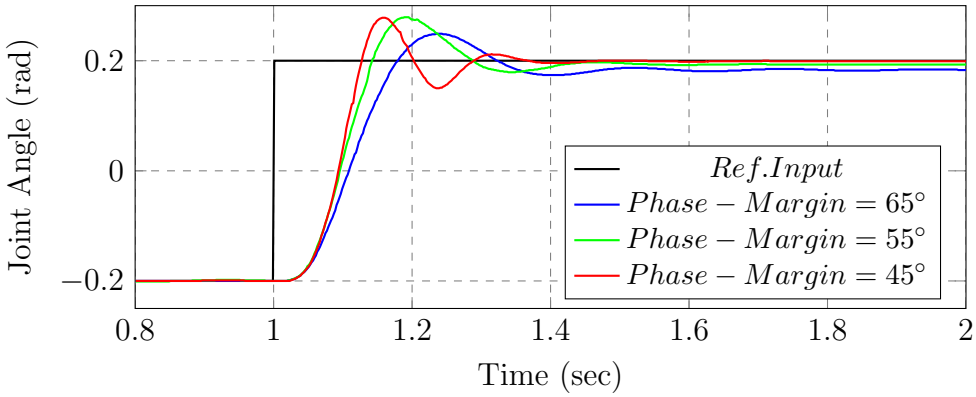


Figure 4.18: Joint position step responses with the automatically selected feedback gains for the SA-SEA.

As the next step, I applied exponential frequency sweep on the actuator with the selected feedback gains. The expected behavior is to have larger bandwidth for lower phase-margin values. Figure 4.19 shows that when the desired-phase margin is reduced from 65° to 45°, the bandwidth of the impedance controller increases gradually but since the stability is reduced, resonant peak becomes steeper.

The experimental results from the SA-SEA show the performance limitations of this low-cost actuator and its simplified controller. Better impedance control bandwidth results can be achieved by implementing more detailed system identification in order to have more accurate system model.

The quality of the plots in Figure 4.17 and in Figure 4.19 are disparate.

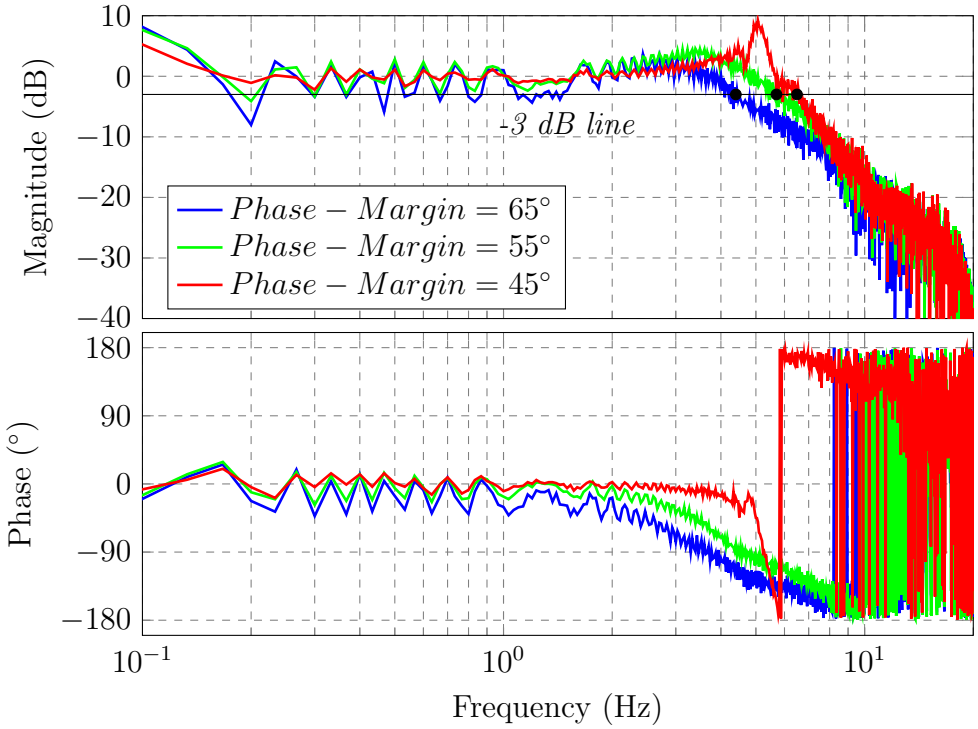


Figure 4.19: Bode plots of the gain selection experiments on the SA-SEA ($f = 0.1 - 20\ Hz$).

The Bode plots in Figure 4.19 are created by using a fast Fourier transform-based identification whereas the Bode plots in Figure 4.17 are generated by stepped sign and the single period phasor transform (Thomas & Sentis (2017)).

## 4.7 Advantages and Shortcomings of the Developed Method

The main advantage of the proposed method is that it significantly reduces the time and effort spent on gain selection for the cascaded PD-type controllers.

Also, this method reduces the number of parameters to be adjusted for a desired stability level on the system. The user can create the phase-margin surface for the system once and the necessary natural frequency values, and thus the necessary feedback gains, for any desired stability level can easily be selected. The gain selection process considers the time-delay and derivative filtering effects and finds the feedback gains accordingly. Therefore, if the system model is accurate, there should not be major difference between the simulation results and the hardware results.

The main drawback of the proposed methodology is that it depends on an overdetermined system of equations for the impedance control feedback gains. In the set of equations (4.12), the second and the third equations are used, which include all the necessary parameters for gain selection. The damping gain of the impedance control loop ($B_i$) is selected using the second equation in this set of equations and it is plugged into the third equation in order to find the stiffness gain of the impedance control loop ($K_i$). It is possible to find $K_i$ first using the fourth equation and then $B_i$ using the third equation. However, in this approach, the desired damping ratio ($\zeta$) has no effect on the stiffness gain. Therefore, in the proposed approach and in the simulations, the second and the third equations are used for finding the stiffness and damping gains of the impedance controller. Figures 4.20 and 4.21 show the difference on the selected impedance control gains when the aforementioned methods used. $B_i$ gains do not show significant difference depending on the selected equation order. However, $K_i$ gains show a difference in the region where force natural

frequency is low and impedance natural frequency is high. This difference does not affect the selected gains significantly since in the stable region the difference in gains is negligible.

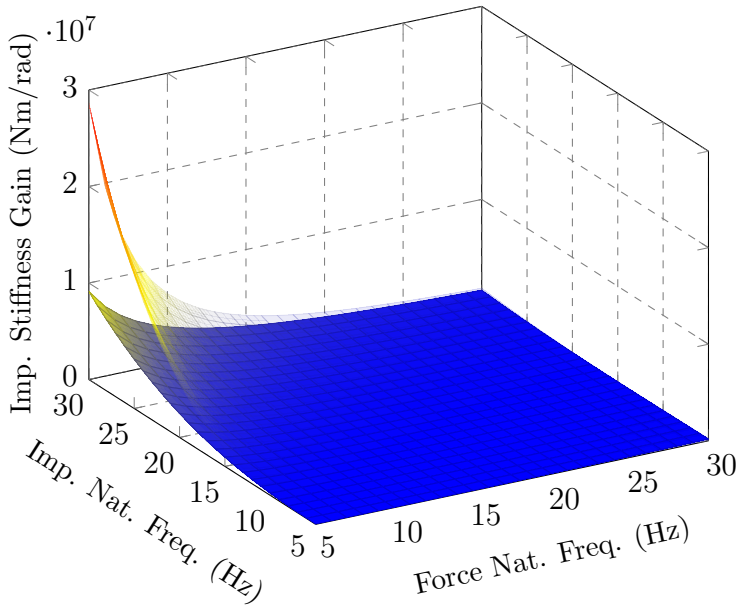


Figure 4.20: Comparison of $K_i$ gains for different gain calculation order. In the stable region, where the force natural frequency is larger than the impedance natural frequency, the difference on the stiffness gains is negligible.

The problem of having an overdetermined system of equations can be treated by using methods such as the least squares approach. Since the necessary gains are selected using the simulated result of the system which satisfies the desired system behavior, optimizing the gains over the range of possible gain selections is left out of the scope of this study and considered as future work.

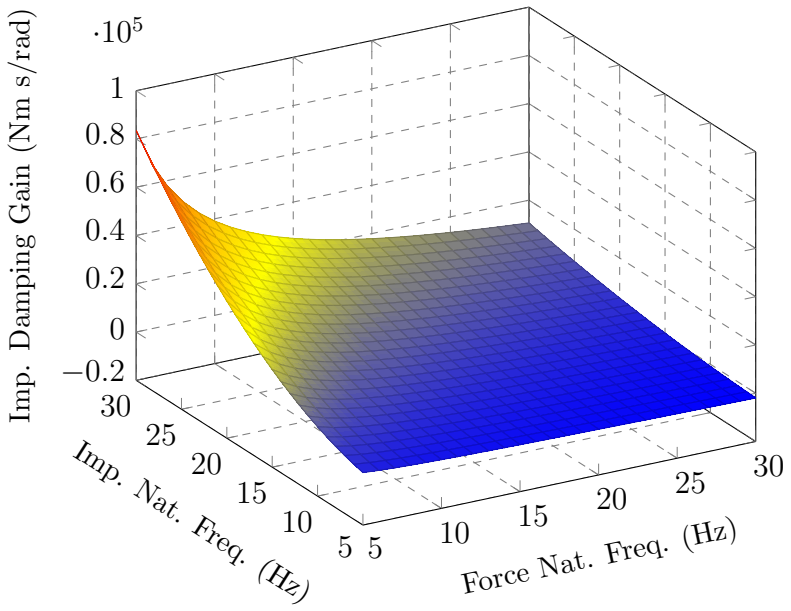


Figure 4.21: Comparison of $B_i$ gains for different gain calculation order. The surfaces are indistinguishable. The plot shows that at the region where the force natural frequency is very high and impedance natural frequency is very low, the damping gains are negative. However, this is out of the region where the feedback gains are selected.

# Chapter 5

# Motion Planning for Agility

## 5.1 Problem Statement

Animals and humans use the elasticity of tendons for energy storage. Depending on the desired goal, the stored energy is used either for energy efficiency such as in locomotion, or increasing joint velocity such as in a throwing motion. When we want to throw an object as fast as we can, we first windup and store energy in our tendons and then use the combined energy coming from the muscles and tendons in order to maximize the arm velocity. This aspect of energy storage property of SEAs rarely investigated in the literature (See Section 2.3 for a literature review). The existing studies on this topic either focus completely on achieving the maximum possible joint velocity without practical use scenarios or focus on developing optimal controllers which tailored for a specific SEA type. In this study, model of a prismatic actuator used for the simulations of the proposed approach. However, this approach

can be used for rotational actuators as well.

Passive energy storage capability of SEAs is mostly used in locomotion applications for energy efficiency purpose. The energy stored in the elastic element when the robot takes a step is used to lift the robot body during the next step. Using this approach, the energy efficiency of robot locomotion can be improved. However, this approach is most easily applied when there is a cyclic motion which designed by considering the eigenfrequency of the actuator spring stiffness and the load on the actuator. If the spring dynamics are not considered during the trajectory planning (if the steps are not synchronized with the eigenfrequency), then the release of the spring energy will act as a disturbance to the controller.

Robot systems usually have nonlinearities in their kinematics, and could potentially have nonlinear elastic elements as well. Excepting gravity compensated or planar robots, gravitational force is an additional nonlinear effect for the vast majority of robots. Therefore, development of a velocity enhancement methodology which exploits the energy storage capability of SEAs and tackles the nonlinearities in the system is imperative for maximizing the joint velocity of actuators and robots with nonlinearities.

The energy storage and release of a SEA depends on the followed joint position and velocity trajectories as well as deflection rate of the elastic element. Therefore, joint velocity enhancement problem is actually an optimal motion planning problem. Unlike other studies on joint velocity enhancement, in this study, we focus on creating optimal motion trajectories to maximize

the joint velocity. These trajectories can then be tracked by using any desired control approach.

Motion trajectories can be created by using convex optimization method for linear systems. However, in order to tackle the effect of nonlinearities in the system, sequential convex optimization should be used. This method has not been used in the literature for maximizing the joint velocity of SEAs. Software libraries (Grant et al. (2008)) exists for this method, which allows the user to employ this method in the embedded level. Using this method on real hardware is one of the future works of this study.

## 5.2 State-Space Model of the Series Elastic Actuator

In this section, a state-space model of the P170 Orion actuator from Apptronik Systems Inc. (See Figure 5.1) is presented. This actuator has a nonlinear kinematic structure which converts the actuator force output to joint torque. In the opposite direction, the gravitational torque, which is already nonlinear due to vertical rotational motion, and the load dynamics are transferred to the ball-screw mechanism through this nonlinear kinematic structure. In order to contain all the nonlinearities in one expression in the model, the effect of the nonlinear toque due to load dynamics and gravitational force are expressed with $F_{ext}$. Figure 5.2 shows the model of the P170 Orion with its three subsystems, namely motor subsystem, actuator subsystem and load subsystem.

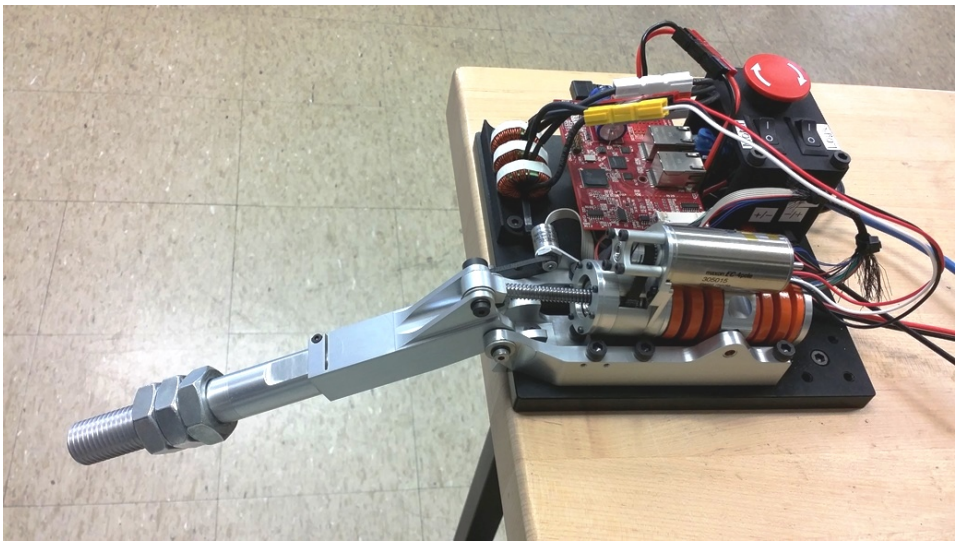

Figure 5.1: P170 Orion SEA from Apptronik Systems Inc.

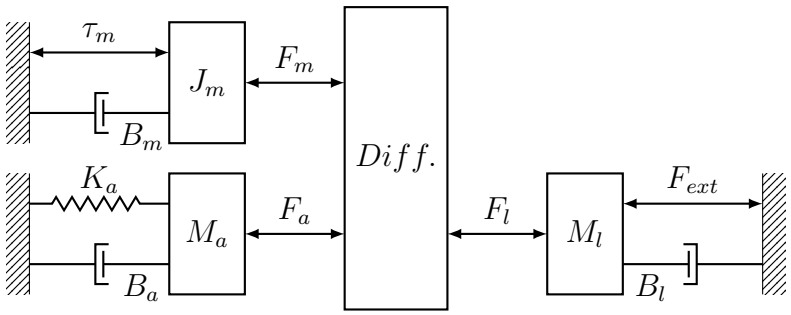


Figure 5.2: The detailed lumped model of the P170 Orion actuator. In this model, $\tau_m$ is the motor torque, $B_m$ is the motor damping, $J_m$ is the rotor inertia of the motor, $F_m$ is the back-drive force affecting the motor, $K_a$ is the spring stiffness, $B_a$ is the viscous friction in the actuator hardware, $M_a$ is the sprung mass of the actuator, $F_a$ is the actuator force, $M_l$ is the load mass before the joint kinematic structure, $B_l$ is the load damping, $F_{ext}$ is the sum of all the load and gravitational effects after the joint kinematics and $F_l$ is the force on the ball-screw that is acting on the load.

In this model, $Diff.$ represents the gear train in P170 SEA, which includes the pulley system and the ball-screw mechanism. All the force-to-torque and torque-to-force conversions as well as rotational-to-linear and linear-to-

rotational motion conversions visualized with this differential box in order to simplify the system's representation. Motor torque to linear ball-bearing force conversion constant can be written as,

$$\beta = \frac{N_p \eta_p 2\pi \eta_{bs_f}}{l} \tag{5.1}$$

where $N_p$ is the pulley ratio, $\eta_p$ is the pulley system efficiency, $\eta_{bs_f}$ is the ball-screw mechanism's forward-drive efficiency and $l$ is the lead of the ball-screw.

For back-drive force, following equation shows the linear force to torque conversion constant,

$$\alpha = \frac{l}{N_p \eta_p 2\pi \eta_{bs_b}} \tag{5.2}$$

where $\eta_{bs_b}$ is the back-drive efficiency of the ball-screw mechanism.

For simplicity, the efficiencies of the components are assumed to be 100% in this study. This assumption allows us to use $\alpha$ for converting the angular position and velocity of the motor to linear position and velocity on the ball-screw mechanism. Similarly, $\beta$ converts the linear position and velocity of the ball-screw mechanism to rotational motion of the motor shaft.

Under the aforementioned assumptions, the dynamic equations for the three subsystems can be written as,

$$J_m \ddot{\theta}_m + B_m \dot{\theta}_m = k_m u - \alpha F_m \tag{5.3}$$

$$M_a \ddot{x}_a + B_a \dot{x}_a + K_a x_a = -F_a \tag{5.4}$$

$$M_l\ddot{x}_l + B_l\dot{x}_l = F_l - F_{ext} \tag{5.5}$$

where $\theta_m$ is the motor position, $x_a$ is the spring deflection, $x_l$ is the actuator output position, $k_m$ is the motor torque constant and $u$ is the motor current.

In these equations, under the 100% efficiency assumption for the drive-train elements, $F_m$, $F_a$ and $F_l$ are equal to each other since $F_a$ is the reaction force created on the load, $F_l$, and $F_m$ is the reaction force transmitted back to the motor with the linear-to-rotational motion conversion constant $\alpha$.

P170 Orion has three sources available for feedback. These are the motor angle, $\theta_m$, the spring deflection, $x_a$ and the joint angle, $\theta j$. The joint angle is dependent on the sum of motor angle and spring deflection. Therefore, the joint angle feedback is neglected. The actuator output position is calculated using the motor angle and spring deflection as,

$$x_l = x_a + \alpha\theta_m. \tag{5.6}$$

Combining the equations (5.5) and (5.6), the Equation (5.5) can be written as,

$$M_l(\ddot{x}_a + \alpha\ddot{\theta}) + B_l(\dot{x}_a + \alpha\dot{\theta}) = F_l - F_{ext}. \tag{5.7}$$

By combining the equations (5.3) and (5.7) and the equations (5.4) and (5.7), the following equations for the system dynamics can be written:

$$(M_a + M_l)\ddot{x}_a + \alpha M_l\ddot{\theta}_m + (B_a + B_l)\dot{x}_a + \alpha B_l\dot{\theta}_m + K_a x_a = -F_{ext} \qquad (5.8)$$

$$M_l\ddot{x}_a + (\alpha M_l + \frac{J_m}{\alpha})\ddot{\theta}_m + B_l\dot{x}_a + (\alpha B_l + \frac{B_m}{\alpha})\dot{\theta}_m = \frac{k_m}{\alpha}u - F_{ext} \qquad (5.9)$$

The equations (5.8) and (5.9) can be written in matrix form as,

$$\begin{bmatrix} 1 & 0 & 0 & 0 \\ 0 & M_a + M_l & 0 & \alpha M_l \\ 0 & 0 & 1 & 0 \\ 0 & M_l & 0 & \frac{J_m}{\alpha} + \alpha M_l \end{bmatrix} \begin{bmatrix} \dot{x}_a \\ \ddot{x}_a \\ \dot{\theta}_m \\ \ddot{\theta}_m \end{bmatrix} = \begin{bmatrix} 0 & 1 & 0 & 0 \\ -K_a & -(B_a + B_l) & 0 & -\alpha B_l \\ 0 & 0 & 0 & 1 \\ 0 & -B_l & 0 & -(\frac{B_m}{\alpha} + \alpha B_l) \end{bmatrix} \begin{bmatrix} x_a \\ \dot{x}_a \\ \theta_m \\ \dot{\theta}_m \end{bmatrix}$$
$$+ \begin{bmatrix} 0 \\ 0 \\ 0 \\ \frac{k_m}{\alpha} \end{bmatrix} u + \begin{bmatrix} 0 \\ -1 \\ 0 \\ -1 \end{bmatrix} F_{ext} \qquad (5.10)$$

If we represent this matrix equation

$$\mathbf{E}\dot{x} = \mathbf{A_0}x + \mathbf{B_0}u, \qquad (5.11)$$

the state-space equation in the standard form can be calculated:

$$\dot{x} = \mathbf{E^{-1}A_0}x + \mathbf{E^{-1}B_0}u = \mathbf{A}\dot{x} + \mathbf{B}u. \tag{5.12}$$

As mentioned previously, $F_{ext}$ encapsulates the effect of the load dynamics after the joint mechanism and the gravitational force. This nonlinear force can be written as,

$$F_{ext} = \frac{\tau_g(\theta_j) + J_l\ddot{\theta}_j}{d(\theta_j)} \tag{5.13}$$

where $J_l$ is the inertia of the load attached to the joint link, $\theta_j$ is the joint angle which is defined as $\theta_j = f(C_0, x_a, \theta_m)$ with $C_0$ representing the initial position of the actuator output. In this equation, $\tau_g(\theta_j)$ is defined as,

$$\tau_g(\theta_j) = m\ g\ l\ cos(\theta_j) \tag{5.14}$$

where $m$ is the load mass on the joint link, $l$ is the center of mass distance of the load mass to the joint, $g$ is the gravitational acceleration constant. $d(\theta_j)$ in the Equation (5.13) is the moment arm length between the actuator output force direction and the joint and defined as,

$$d(\theta_t) = \frac{b\ c\ sin(\theta_t)}{\sqrt{b^2 + c^2 - 2\ b\ c\ cos(\theta_t)}} \tag{5.15}$$

where $b$ and $c$ are lengths on the joint kinematic structure and $\theta_t$ is the inner angle shown in Figure 5.3.

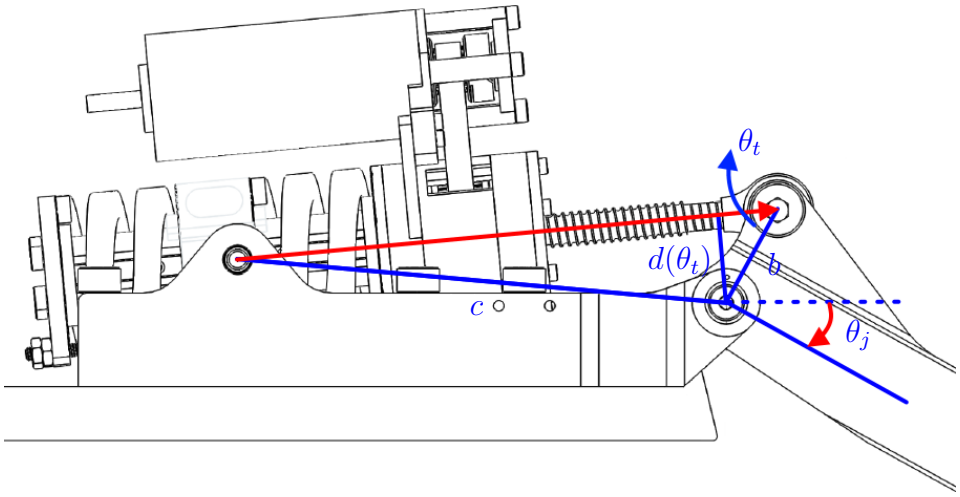


Figure 5.3: Joint kinematics of P170 Orion SEA.

## 5.3 Formulation of the Optimization Problem

Sequential convex optimization is an iteration-based optimization method for nonlinear systems. In this method, the non-convex optimization problem of optimal trajectory generation with a nonlinear model is reduced to a sequence of convex optimization problems for a series of ever more accurate linearizations of the dynamics. In this section, the formulation of the optimization problem for maximizing the joint velocity is presented.

The state-space model of the P170 Orion presented in Section 5.2 is a continuous-time model. In order to run the optimization process, this model should be discretized. There are multiple ways of discretization of a continuous-time system. In this study, we used zero-order hold method. By using the zero-order hold method, the continuous-time model of the system

given in Equation (5.12) can be discretized as,

$$\begin{aligned} \mathbf{A_d} &= e^{\mathbf{A}T} \\ \mathbf{B_d} &= \int_{\tau=0}^{T} e^{\mathbf{A}T} d\tau \mathbf{B} \end{aligned} \tag{5.16}$$

where $T$ is the sample time.

The state vector of the system is

$$x = [x_a \ \dot{x}_a \ \theta_m \ \dot{\theta}_m]' \tag{5.17}$$

where $x_a$ is the spring deflection, $\dot{x}_a$ is the spring deflection rate, $\theta_m$ is the motor position and $\dot{\theta}_m$ is the motor velocity. The actuator output velocity is calculated by using the spring deflection and the motor position as,

$$\dot{x}_l = \dot{x}_a + \alpha \dot{\theta}_m \tag{5.18}$$

The Equation (5.18) constitutes the objective function for maximization. Since the joint velocity, $\dot{\theta}_j$, is dependent on actuator output velocity, $\dot{x}_l$, through the joint kinematics, this objective function satisfies the goal of this optimization study which is maximization of joint velocity.

There are physical limitations in the system which should be taken into consideration for a realistic simulation of the system. The biggest limiting factor is the maximum motor current. The maximum motor current, thus the maximum motor torque, sets the limit of the maximum actuator output

velocity if a rigid actuator was being used.[1] In this study, the maximum actuator output velocity limit, which is set by the maximum motor torque, is increased by the storage and timely release of potential energy in the spring. However, there is a limit on the potential energy that can be stored in the spring. If no limit is set for the spring deflection, it is possible to damage the hardware by compressing the spring until its shut length. Also, joint position limits set the limits for actuator output position. These limitations were taken into consideration and they constitute inequality constraints of the optimization process.

The result of the sequential convex optimization process depends on the initial conditions. For this study, the system is assumed to be at rest with the joint angle equal to zero. This means that there is no deflection on the spring beyond that needed for gravity compensation and the motor angle is zero. This constraint constitutes the first equality constraint of the optimization process.

The desired final joint angle is zero where the joint arm is parallel to the ground. This constraint constitutes the second equality constraint of the optimization process. The joint velocity is aimed to be maximized at this point.

By considering the aforementioned objective function and constraints, the algorithm for joint velocity maximization can be summed up as following algorithm:

[1]On the real hardware, the maximum actuator output velocity is set by the speed limit of the ball-screw mechanism. In order to demonstrate the potential of the proposed methodology, this hardware limitation was ignored.

**Algorithm 2** Joint Velocity Maximization Algorithm

initializations
set state-space model
discretize state-space model
estimate the state trajectories
**for** $i \in \{1, \ldots, I\}$ **do**
  **for** $n \in \{1, \ldots, N\}$ **do**
    calculate joint kinematics at n
    calculate gravitational force at n
    linearize discrete state-space model at n
    linearize $F_{ext}$ at n
  **end for**

$$
\begin{aligned}
\max \quad & x(N:2) + x(N:4) + \epsilon \; sum(abs(u)) \\
\text{s.t.} \quad & -u_{max} \leq u \leq u_{max} \\
& -x_{l_{max}} \leq x_{l_a} \leq x_{l_{max}} \\
& \mathbf{x}_0 = 0 \\
& x(N:1) + x(N:3) = 0 \\
& \textbf{for } k \in \{2, \ldots, N\} \textbf{ do} \\
& \quad x_k = A_k x_{k-1} + B_k u_{k-1} \\
& \quad (\textit{constrain the system to obey the linearized dynamics}) \\
& \textbf{end for}
\end{aligned}
$$

**end for**

In Algorithm 2, $I$ is the number of the iteration of the optimization process, $N$ is the task time in milliseconds and also the number of sampling points in the state trajectories, $\epsilon$ is a small penalty coefficient for the control input, $u_{max}$ is the maximum motor current, $x_{a_{max}}$ is the maximum spring deflection, $\mathbf{x}_0$ is the vector of zero initial conditions, and $A_k$ and $B_k$ are the linearized system dynamics.

As shown in the Algorithm 2, the optimization process is iterative. Af-

ter each run, the result of that optimization process are used as the estimated state trajectories for the next iteration. In the objective function of the sequential convex optimization process, the control input is penalized with a small coefficient ($\epsilon$) in order to prevent extraneous joint motion.

After using the Algorithm 2, the joint trajectories can be plotted.

## 5.4 Simulation of the Methodology

In this section, the simulations of the optimization process explained in Section 5.3 are presented. The system model created in Section 5.2 purely relies on the datasheet values of the component properties and it is strictly connected with the system's structure. Our experience suggests that for a realistic system simulation which produces results that are similar to hardware experiments' results, using the datasheet values of the system parameters is not the best approach. Since this study is intended to be applied on a real hardware, in order to better predict the outcome of the experiments on hardware, results of a previous system identification study on the subsystems of the UT-SEA are used in the simulations in this section. A system identification study on P170 is in progress. It should be noted that since the purpose of the simulation part of this study is showing that sequential convex optimization method can be used in order to maximize the joint velocity of SEAs with nonlinearities, small errors on the system parameters does not impair the significance of the simulation results. Table 5.1 shows the system parameters' values used in this study.

Table 5.1: Actuator and load parameters of the SEA model.

| **Parameter** | **Value** |
|---|---|
| $J_m$ | 293 kg |
| $B_m$ | 1680 Ns/m$^2$ |
| $M_a$ | 1.7 kg |
| $B_a$ | 1100 Ns/m$^2$ |
| $K_a$ | 350000 N/m |
| $M_l$ | 29.4 kg |
| $B_l$ | 1100 Ns/m$^2$ |
| $k_m$ | 157 N/A |
| $u_{max}$ | 15 A |

The system identification on the motor subsystem helps us create a linearly moving mass-damper representation of the rotational motor subsystem. Using the identified system parameters simplifies the equations in the system model since the torque-to-force and force-to-torque conversion parameters can be eliminated. Figure 5.2 shows the model of the system as though it were all prismatic motion.

Before simulating the optimal state trajectories, it is necessary to calculate the maximum velocity of the rigid counterpart of the actuator. When the spring is removed from the model shown in Figure 5.2, the system can be further simplified to a mass-damper system. When we simulate this simplified system with highest current input and linearized nominal external force, the final value of the maximum velocity is higher than the result of optimal motion planning algorithm. However, when the joint limitations are applied to the rigid actuator as well, the maximum actuator output velocity is found as 0.215 m/s. This velocity sets the reference for the success of sequential convex

optimization algorithm output.

It should be noted that in this section, actuator output velocities are shown in the graphs. The joint velocity is related to actuator output velocity through the kinematic structure of the testbed.

There are multiple parameters and constraints affecting the result of the optimal motion planning algorithm. The effects of spring stiffness and load mass on load arm are analyzed in sections 5.4.1 and 5.4.2, respectively. Other than these two important system parameters, the input penalty, $\epsilon$, allowed total task time, $N$ (in ms), and constraints on the joint position significantly affect the final results.

Figure 5.4 shows the actuator position, actuator velocity, and motor current input for nominal system parameters. The windup and swing motion is completed in 130 ms. The reason for this small task time is the high spring stiffness. High spring stiffness results in quick energy release. If the task time is increased without increasing the penalty on current input, the system output shows oscillatory behavior and reaches higher output velocities. This output behavior is shown in Figure 5.5. When the task time is high enough and the penalty on the current input is increased, the actuator output stays in the proximity of the initial position first and performs the windup and swing motion towards the end of task time. This output behavior is shown in Figure 5.6. It was also observed that short task times produce one windup and swing motion. However, the achieved maximum joint velocity decreases with reduced task time.

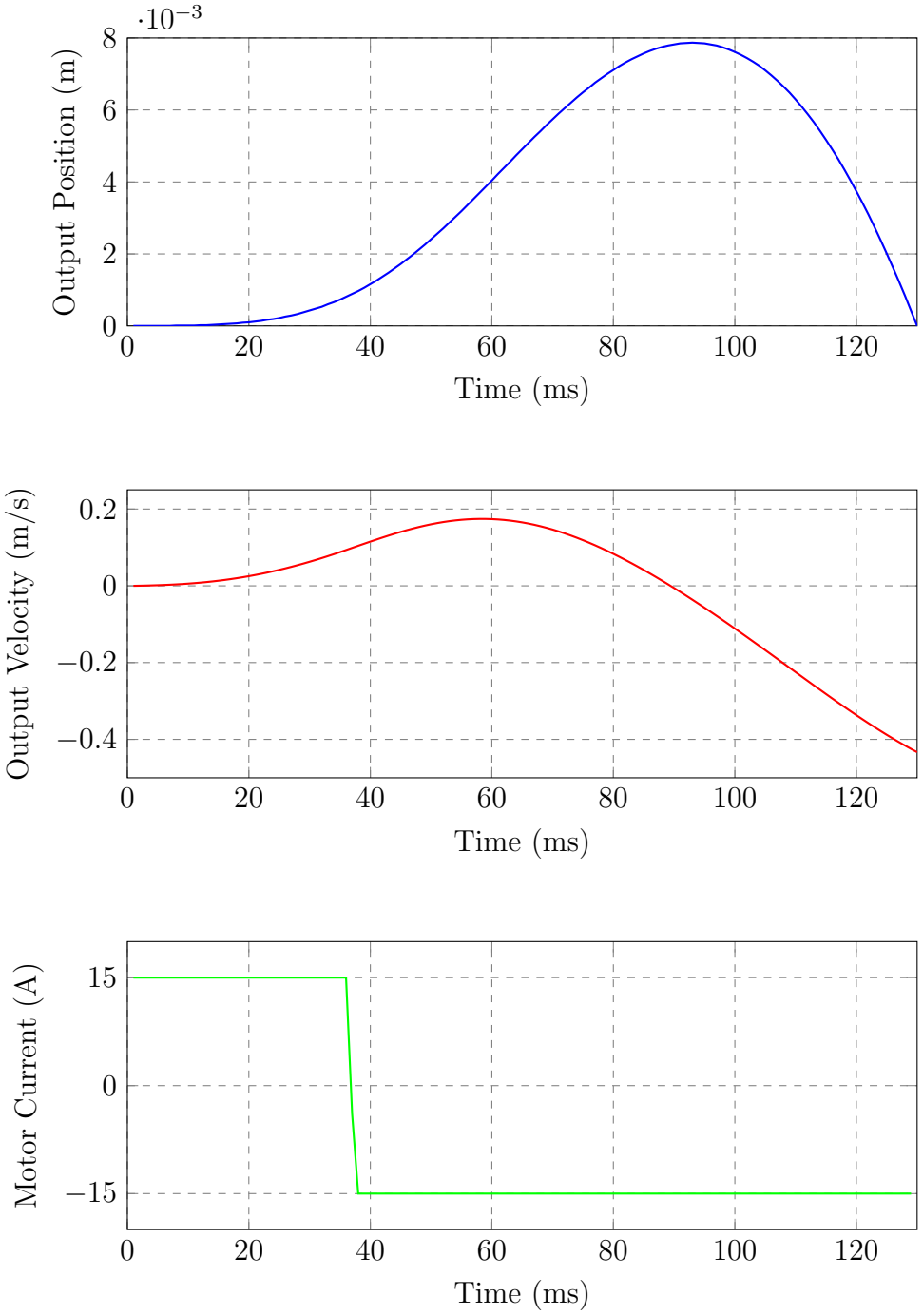


Figure 5.4: Simulation of joint velocity maximization for the nominal system.

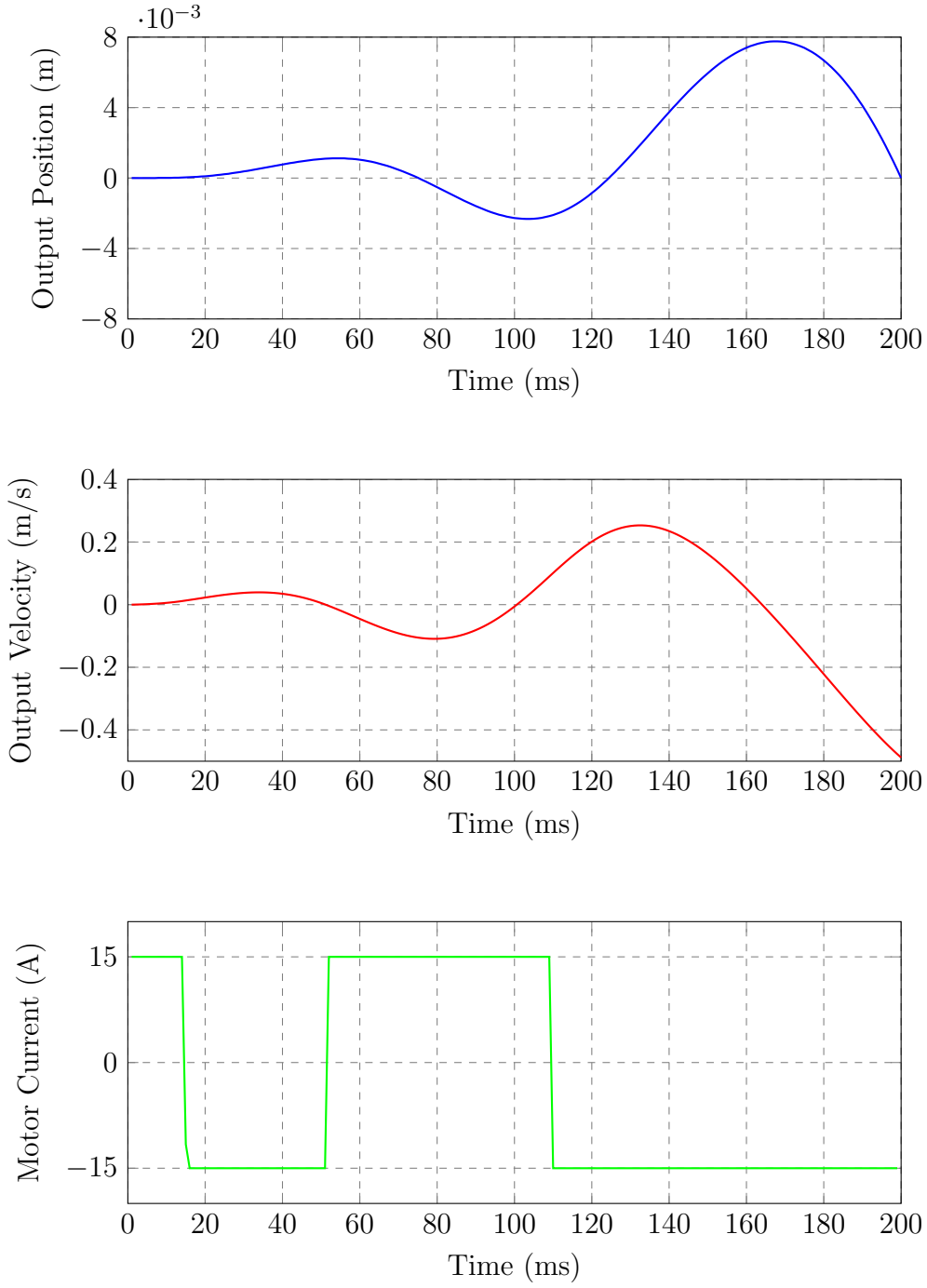


Figure 5.5: Simulation of the case with long task time and small penalty on the current input.

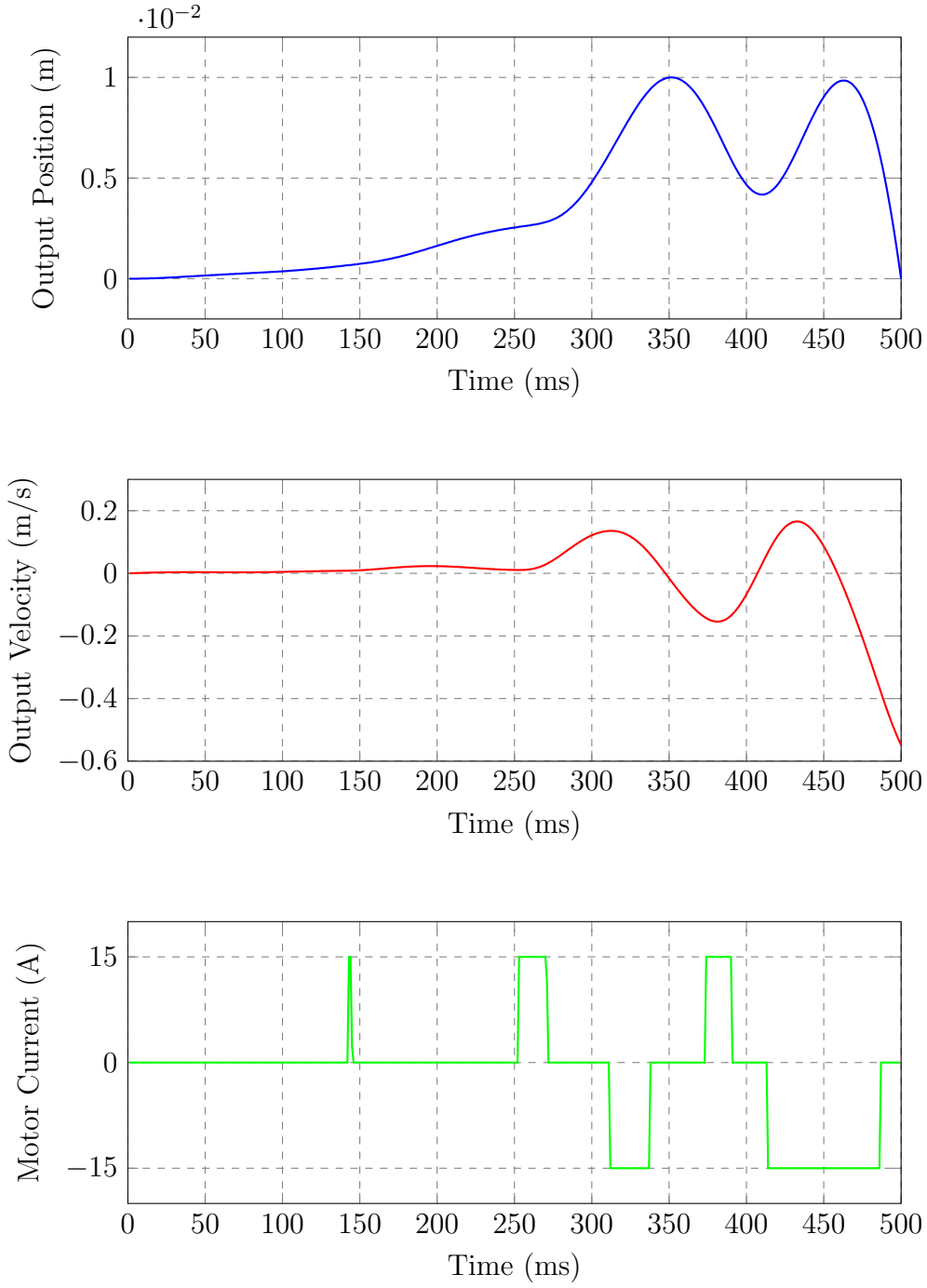


Figure 5.6: Simulation of the case with long task time and high penalty on the current input.

### 5.4.1 The Effect of the Spring Stiffness

As a hardware design parameter, spring stiffness plays an important role on maximizing the joint velocity of SEAs. Optimal spring stiffness for maximizing the joint velocity for SEAs (Paluska & Herr (2006a)) and VSAs (Garabini et al. (2011)) have been analyzed in the literature. In this study, the goal is finding the optimal state trajectories in order to maximize the joint velocity. However, it is beneficial to analyze the effect of spring stiffness on the optimization results. This analysis can serve as a reference for future SEA designs for which achieving maximum joint velocity is desired.

It is expected that low spring stiffness will result in low output velocity since the maximum potential energy that can be stored in the spring, considering the maximum spring deflection limit, will be limited. When the spring stiffness is increased, the maximum joint velocity should also increase. However, after a certain spring stiffness, the inertia of the load would not be able to load the spring to its maximum energy storage capacity. After this point, oscillatory behavior at the actuator output is expected. By oscillating the output at the eigenfrequency of the spring-load pair, resonating output can reach to much higher velocities than the velocities that can be achieved by one windup and swing motion.

In order to see the effect of spring stiffness on the optimal actuator output behavior, the nominal system parameters which produces the results shown in Figure 5.4 were taken, and by varying only the spring stiffness, the optimization algorithm was used. Figure 5.7 shows the actuator output

velocities for different spring stiffness values.

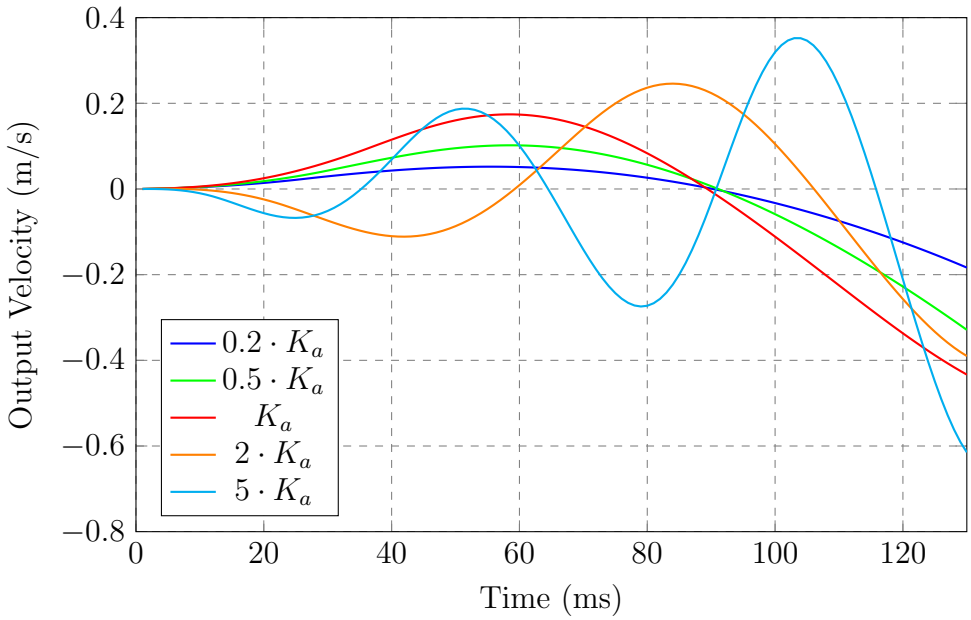


Figure 5.7: Optimal joint velocity trajectories for varying spring stiffness values.

As expected, reducing the spring stiffness reduces the maximum output velocity and increasing the spring stiffness forces the optimization algorithm to create oscillatory output in order to maximize the output velocity. It should be noted that the nominal spring stiffness looks as it is at the limit where increasing the spring stiffness creates oscillatory output. However this is true for the used task time. It is possible to have oscillatory output with a softer spring if the task time is increased or one windup and swing motion with a stiffer spring if the task time is reduced.

### 5.4.2 The Effect of the Load Mass

Similar to spring stiffness, the load mass is also expected to have a considerable effect on the maximum output velocity of the actuator. Intuitively, increasing the load mass should reduce the maximum actuator output velocity, at least for those masses which are already storing as much spring energy as possible. On the other hand, reducing the load mass should have a limit on the highest achievable actuator output because low load mass values cannot use load inertia to fully compress the spring. As the load mass is reduced, the contribution of the elastic element on the output velocity diminishes. Also, for the low load mass values, the damping in the system becomes dominant relative to load inertia. Therefore, further reducing the load mass cannot increase the actuator output.

Figure 5.8 shows the influence of the mass parameter on the optimal trajectory.

The simulation results shown in Figure 5.8 agree with the expected actuator velocity output behavior. Increasing the load mass reduces the maximum output velocity while there is a limit on the maximum output velocity for small load masses. These simulations also show that the selected nominal load is close to this low load mass limit. Therefore, further reducing the load mass cannot increase the output velocity.

The load mass, $m$, which was varied in Figure 5.8 is the load attached to the load arm. Therefore, the change on this mass affects the nonlinear force, $F_{ext}$, in the system. When the linear load is also reduced, the maximum

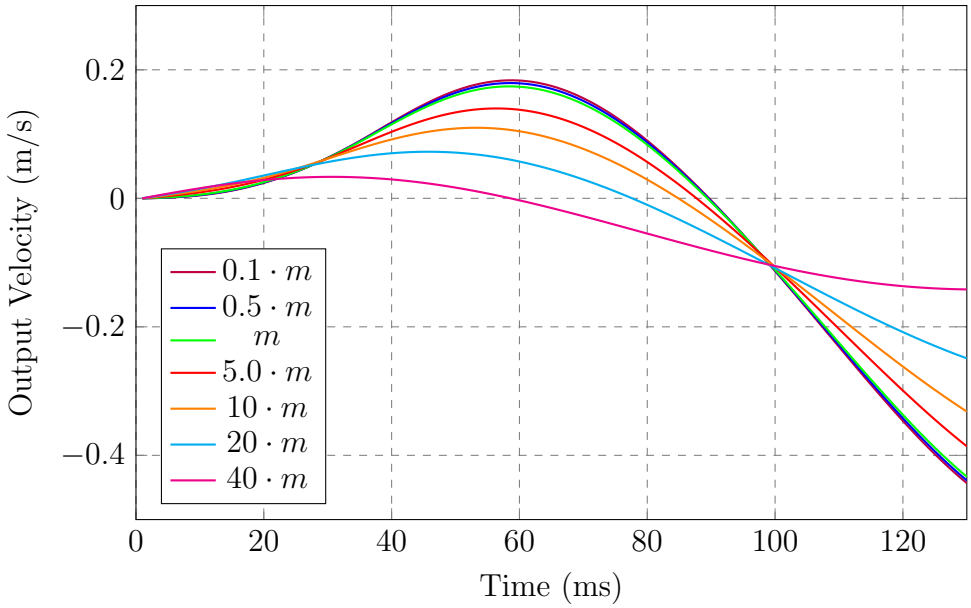


Figure 5.8: Simulation of load mass effect on joint velocity maximization. $m$ is the mass of the load attached to the load arm.

output velocity is expected to converge to the maximum velocity of the rigid counterpart of this actuator since the energy storage in the spring would be minimal with small load inertia.

# Chapter 6

# Conclusions and Future Work

The main purpose of this work is to increase the availability of SEAs to a broader range of users and researchers by reducing the cost and simplifying the use of these devices. SEAs are being used in many robotic applications related to safety, health-care, industry, military, etc. However, the hardware complexity of these mechatronic devices compared to rigid actuators significantly increases the manufacturing costs, and therefore it is an obstacle for the deployment of this technology to more robotic applications.

In order to demonstrate the possibility of low-cost realization of an industrial grade SEA while maintaining a high force and position control performance, a case study on low-cost design of an industrial grade SEA is presented in this dissertation. By reducing the number of custom parts, simplifying the assembly process, exploiting the low-cost labor and component market of China's Shenzhen region, a significant cost reduction on manufacturing of a high-performance SEA was achieved.

As a low-priority design parameter, the weight of the actuator also increased. There are two important reasons for the weight increase. Firstly, the bulkiness of the low-cost components increases the actuator weight. This is unavoidable for the low-cost design studies. Secondly, the industrial-grade design goal requires structural sturdiness and high expected service life. These design requirements increases the size and weight of the used components.

This study showed that using low-cost motors with high torque ripples do not significantly affect the force and position control performance of SEAs. It was observed that the low frequency torque ripples are eliminated by the force control loop and the high frequency torque ripples are filtered by the spring in the system. Therefore, the high torque ripples seen at the motor output does not affect the position control performance. This aspect of SEA dynamics can be further analyzed by adding artificial torque ripples to the motor output and checking its effect on the output position of the actuator when there is no position control loop. Analysis of torque ripple effect on output position is one of the future works of this study. The effect of individual components' performance on overall actuator performance can be analyzed in order to find possible cost reduction opportunities for future SEA designs.

The next step after the mechanical design of SEAs is the development of control architectures. SEA controllers mostly consist of PID-based cascaded control loops. Among the variations of the PID-based SEA controllers, PD-type control is the most common approach. The reasons behind this controller type selection are given in Section 2.2. Feedback gain selection of cascaded

controllers for high order systems is a time consuming tedious process. It is a common practice to fix the actuator output rigidly and set the feedback gains for the force controller first and then to work on the feedback gains of the outer control loop. However, this approach limits the achievable high control bandwidth of position and impedance controllers of SEAs. In this dissertation, an optimal feedback gain selection for the inner and outer control loops of the SEAs is presented. The proposed methodology takes advantage of independent scaling the inner and outer control loops' feedback gains and automatically trades off force control bandwidth for total closed loop impedance performance. By using the critically damped system output criterion, stiffness and damping gains are related to each other via natural frequencies. This reduces the search space of the optimal gain selection process. The proposed optimal gain selection method allows the users to automatically select the maximum stiffness and damping gains for the desired phase-margin values, as a proxy for allowable overshoot behavior. The gain selection approach includes the effects of derivative filtering and time-delay on feedback. Experimental results show significant improvement on the bandwidth of impedance controllers.

The actuator model used for this study is a simplified model of a SEA. For instance, the motor dynamics is not included in the model. Therefore, the system representation is limited which can lead to less than ideal control performance on the actuator. Also, even though it is a widely used approach, finding the feedback gains of the inner force controller with a fixed actuator output modeling is not the ideal approach. After releasing the actuator output

for position control, the pole locations of the inner controller changes. The feedback gains that are selected when the actuator output is grounded can easily lead the force controller to an unstable region when the load on the output is very small. In order to overcome the performance limitations due to the simplifications on the system model, designing a detailed optimal feedback gain selection for higher order systems is considered as a future work for this study.

The energy storage capability of SEAs offer great improvements on the maximum achievable joint velocity. The maximum achievable joint velocity of the rigid actuators depends mainly on the motor torque and load mass. On the other hand, the maximum achievable joint velocity of SEAs depends on maximum amount of energy that can be stored in the spring. By designing motion trajectories, potential energy can be stored and controllably released in order to increase the maximum achievable joint velocity. In this dissertation, a sequential convex optimization method is used in order to find the optimal state trajectories which maximizes the joint velocity. The significance of this method is that it is possible to include the nonlinearities in the system while performing the optimization algorithm. Since this is a motion planning approach. it does not depend on a specific controller architecture. The designed state trajectories can be used as references for any different controller approach.

The proposed methodology is simulated in MATLAB environment by using a detailed model of a SEA. Significant velocity improvements were

achieved compared to the rigid counterpart of the actuator. Also, the effect of the spring stiffness and the load mass was analyzed.

The future work of this study is the implementation of the proposed methodology on a real hardware. This can be done off-line by optimizing the state trajectories in MATLAB and using the output of this optimization as a reference for the controller on the hardware or the whole optimization process can be performed in the embedded controller of the actuator. C++ libraries for convex optimization exist (Grant et al. (2008)) and can be used for the latter option. Modern C++ libraries for convex optimization offer hope that this type of sequential algorithm could one day be run on the low-level embedded processor, in real-time.

# References

Accoto, D., Carpino, G., Sergi, F., Tagliamonte, N. L., Zollo, L., & Guglielmelli, E. (2013). Design and characterization of a novel high-power series elastic actuator for a lower limb robotic orthosis. *International Journal of Advanced Robotic Systems*, *10*(10), 359.

Agarwal, P., Fox, J., Yun, Y., OMalley, M. K., & Deshpande, A. D. (2015). An index finger exoskeleton with series elastic actuation for rehabilitation: Design, control and performance characterization. *The International Journal of Robotics Research*, *34*(14), 1747–1772.

Albu-Schäffer, A., Ott, C., & Hirzinger, G. (2007). A unified passivity-based control framework for position, torque and impedance control of flexible joint robots. *The International Journal of Robotics Research*, *26*(1), 23–39.

Ames, A. D., & Holley, J. (2014). Quadratic program based nonlinear embedded control of series elastic actuators. In *Decision and control (cdc), 2014 ieee 53rd annual conference on* (pp. 6291–6298).

Arumugom, S., Muthuraman, S., & Ponselvan, V. (2009). Modeling and application of series elastic actuators for force control multi legged robots. *Journal of Computing*, *1*(1), 26–33.

Bae, J., Kong, K., & Tomizuka, M. (2010). Gait phase-based smoothed sliding mode control for a rotary series elastic actuator installed on the knee joint. In *American control conference (acc), 2010* (pp. 6030–6035).

Calanca, A., Capisani, L., & Fiorini, P. (2014). Robust force control of series elastic actuators. In *Actuators* (Vol. 3, pp. 182–204).

Calanca, A., & Fiorini, P. (2014). Human-adaptive control of series elastic actuators. *Robotica*, *32*(08), 1301–1316.

Campbell, E., Kong, Z. C., Hered, W., Lynch, A. J., O'Malley, M. K., & McLurkin, J. (2011). Design of a low-cost series elastic actuator for multi-robot manipulation. In *Robotics and automation (icra), 2011 ieee international conference on* (pp. 5395–5400).

Catalano, M. G., Grioli, G., Garabini, M., Bonomo, F., Mancini, M., Tsagarakis, N., & Bicchi, A. (2011). Vsa-cubebot: A modular variable stiffness platform for multiple degrees of freedom robots. In *Robotics and automation (icra), 2011 ieee international conference on* (pp. 5090–5095).

Chen, L., Garabini, M., Laffranchi, M., Kashiri, N., Tsagarakis, N. G., Bicchi, A., & Caldwell, D. G. (2013). Optimal control for maximizing velocity of

the compact compliant actuator. In *Robotics and automation (icra), 2013 ieee international conference on* (pp. 516–522).

Colgate, J. E., & Brown, J. M. (1994). Factors affecting the z-width of a haptic display. In *Robotics and automation, 1994. proceedings., 1994 ieee international conference on* (pp. 3205–3210).

Curran, S., & Orin, D. E. (2008). Evolution of a jump in an articulated leg with series-elastic actuation. In *Robotics and automation, 2008. icra 2008. ieee international conference on* (pp. 352–358).

De Luca, A., & Flacco, F. (2012). Integrated control for phri: Collision avoidance, detection, reaction and collaboration. In *Biomedical robotics and biomechatronics (biorob), 2012 4th ieee ras & embs international conference on* (pp. 288–295).

Diftler, M. A., Mehling, J., Abdallah, M. E., Radford, N. A., Bridgwater, L. B., Sanders, A. M., ... others (2011). Robonaut 2-the first humanoid robot in space. In *Robotics and automation (icra), 2011 ieee international conference on* (pp. 2178–2183).

dos Santos, W. M., Caurin, G. A., & Siqueira, A. A. (2013). Torque control characterization of a rotary series elastic actuator for knee rehabilitation. In *Advanced robotics (icar), 2013 16th international conference on* (pp. 1–6).

dos Santos, W. M., Caurin, G. A., & Siqueira, A. A. (2015). Design and control of an active knee orthosis driven by a rotary series elastic actuator. *Control Engineering Practice*.

dos Santos, W. M., & Siqueira, A. A. (2014). Impedance control of a rotary series elastic actuator for knee rehabilitation. *IFAC Proceedings Volumes*, *47*(3), 4801–4806.

Edsinger-Gonzales, A., & Weber, J. (2004). Domo: A force sensing humanoid robot for manipulation research. In *Humanoid robots, 2004 4th ieee/ras international conference on* (Vol. 1, pp. 273–291).

Ellis, G. (2012). *Control system design guide: using your computer to understand and diagnose feedback controllers*. Butterworth-Heinemann.

Ettema, G. (1996). Mechanical efficiency and efficiency of storage and release of series elastic energy in skeletal muscle during stretch-shorten cycles. *Journal of Experimental Biology*, *199*(9), 1983–1997.

Fitzgerald, C. (2013). Developing baxter. In *Technologies for practical robot applications (tepra), 2013 ieee international conference on* (pp. 1–6).

Focchi, M., Medrano-Cerda, G. A., Boaventura, T., Frigerio, M., Semini, C., Buchli, J., & Caldwell, D. G. (2016). Robot impedance control and passivity analysis with inner torque and velocity feedback loops. *Control Theory and Technology*, *14*(2), 97–112.

Garabini, M., Passaglia, A., Belo, F., Salaris, P., & Bicchi, A. (2011). Optimality principles in variable stiffness control: The vsa hammer. In *Intelligent robots and systems (iros), 2011 ieee/rsj international conference on* (pp. 3770–3775).

Grant, M., Boyd, S., & Ye, Y. (2008). *Cvx: Matlab software for disciplined convex programming.*

Grebenstein, M., Albu-Schäffer, A., Bahls, T., Chalon, M., Eiberger, O., Friedl, W., ... others (2011). The dlr hand arm system. In *Robotics and automation (icra), 2011 ieee international conference on* (pp. 3175–3182).

Gregorio, P., Ahmadi, M., & Buehler, M. (1997). Design, control, and energetics of an electrically actuated legged robot. *IEEE Transactions on Systems, Man, and Cybernetics, Part B (Cybernetics)*, *27*(4), 626–634.

Groothuis, S., Carloni, R., & Stramigioli, S. (2014). A novel variable stiffness mechanism capable of an infinite stiffness range and unlimited decoupled output motion. In *Actuators* (Vol. 3, pp. 107–123).

Grün, M., Müller, R., & Konigorski, U. (2012). Model based control of series elastic actuators. In *Biomedical robotics and biomechatronics (biorob), 2012 4th ieee ras & embs international conference on* (pp. 538–543).

Haddadin, S., Albu-Schaffer, A., De Luca, A., & Hirzinger, G. (2008). Collision detection and reaction: A contribution to safe physical human-robot

interaction. In *Intelligent robots and systems, 2008. iros 2008. ieee/rsj international conference on* (pp. 3356–3363).

Haddadin, S., Laue, T., Frese, U., Wolf, S., Albu-Schäffer, A., & Hirzinger, G. (2009). Kick it with elasticity: Safety and performance in human–robot soccer. *Robotics and Autonomous Systems*, *57*(8), 761–775.

Haddadin, S., Özparpucu, M. C., & Albu-Schäffer, A. (2012). Optimal control for maximizing potential energy in a variable stiffness joint. In *Decision and control (cdc), 2012 ieee 51st annual conference on* (pp. 1199–1206).

Haddadin, S., Weis, M., Wolf, S., & Albu-Schäffer, A. (2011). Optimal control for maximizing link velocity of robotic variable stiffness joints. *IFAC Proceedings Volumes*, *44*(1), 6863–6871.

Haldane, D. W., Plecnik, M., Yim, J., & Fearing, R. (2016). Robotic vertical jumping agility via series-elastic power modulation. *Science Robotics*, *1*(1), eaag2048.

Hasankola, M. D., Dashkhaneh, A., Moghaddam, M. M., & Saba, A. M. (2013). Design of a rotary elastic actuator for use as torque-actuator in rehabilitation robots. In *Robotics and mechatronics (icrom), 2013 first rsi/ism international conference on* (pp. 505–510).

Hogan, N. (1985). Impedance control: An approach to manipulation: Part iiimplementation. *Journal of dynamic systems, measurement, and control*, *107*(1), 8–16.

Hogan, N., & Buerger, S. P. (2005). Impedance and interaction control. *Robotics and automation handbook*, *1*.

Holmberg, R., Dickert, S., & Khatib, O. (1993). A new actuation system for high-performance torque-controlled manipulators. In *Romansy 9* (pp. 285–292). Springer.

Hondo, T., & Mizuuchi, I. (2011). Analysis of the 1-joint spring-motor coupling system and optimization criteria focusing on the velocity increasing effect. In *Robotics and automation (icra), 2011 ieee international conference on* (pp. 1412–1418).

Hurst, J. W., Chestnutt, J. E., & Rizzi, A. A. (2010). The actuator with mechanically adjustable series compliance. *IEEE Transactions on Robotics*, *26*(4), 597–606.

Hutter, M. (2013). *Starleth & co.–design and control of legged robots with compliant actuation* (PhD Thesis). ETH Zurich.

Hutter, M., Remy, C. D., Hoepflinger, M. A., & Siegwart, R. (2011). Scarleth: Design and control of a planar running robot. In *Intelligent robots and systems (iros), 2011 ieee/rsj international conference on* (pp. 562–567).

Hutter, M., Remy, C. D., Hoepflinger, M. A., & Siegwart, R. (2013). Efficient and versatile locomotion with highly compliant legs. *IEEE/ASME Transactions on Mechatronics*, *18*(2), 449–458.

Hutter, M., Remy, C. D., & Siegwart, R. (2009). *Design of an articulated robotic leg with nonlinear series elastic actuation.* Eidgenössische Technische Hochschule Zürich, Autonomous Systems Lab.

Isik, K., He, S., Ho, J., & Sentis, L. (2017). Re-engineering a high performance electrical series elastic actuator for low-cost industrial applications. In *Actuators* (Vol. 6, p. 5).

Jafari, A., Tsagarakis, N. G., & Caldwell, D. G. (2013). A novel intrinsically energy efficient actuator with adjustable stiffness (awas). *IEEE/ASME Transactions on Mechatronics*, *18*(1), 355–365.

Katsumata, S., Ichinose, S., Shoji, T., Nakaura, S., & Sampei, M. (2009). Throwing motion control based on output zeroing utilizing 2-link underactuated arm. In *American control conference, 2009. acc'09.* (pp. 3057–3064).

Kaya, K. D., & Çetin, L. (2017). Adaptive state feedback controller design for a rotary series elastic actuator. *Transactions of the Institute of Measurement and Control*, *39*(1), 61-74.

Khatib, O. (1987). A unified approach for motion and force control of robot manipulators: The operational space formulation. *IEEE Journal on Robotics and Automation*, *3*(1), 43–53.

Kisliuk, E. (2015, Sep). *Valkyrie.* Retrieved 2017-03-06, from `http://www.nasa.gov/feature/valkyrie`

Kong, K., Bae, J., & Tomizuka, M. (2009). Control of rotary series elastic actuator for ideal force-mode actuation in human–robot interaction applications. *IEEE/ASME transactions on mechatronics*, *14*(1), 105–118.

Kong, K., Bae, J., & Tomizuka, M. (2012). A compact rotary series elastic actuator for human assistive systems. *IEEE/ASME transactions on mechatronics*, *17*(2), 288–297.

Kubo, K., Kawakami, Y., & Fukunaga, T. (1999). Influence of elastic properties of tendon structures on jump performance in humans. *Journal of applied physiology*, *87*(6), 2090–2096.

Kumpf, A. (2007). *Explorations in low-cost compliant robotics* (Master's Thesis). Massachusetts Institute of Technology.

Kwa, H. K., Noorden, J. H., Missel, M., Craig, T., Pratt, J. E., & Neuhaus, P. D. (2009). Development of the ihmc mobility assist exoskeleton. In *Robotics and automation, 2009. icra'09. ieee international conference on* (pp. 2556–2562).

Laffranchi, M., Chen, L., Kashiri, N., Lee, J., Tsagarakis, N. G., & Caldwell, D. G. (2014). Development and control of a series elastic actuator equipped with a semi active friction damper for human friendly robots. *Robotics and Autonomous Systems*, *62*(12), 1827–1836.

Lagoda, C., Schouten, A. C., Stienen, A. H., Hekman, E. E., & van der Kooij, H. (2010). Design of an electric series elastic actuated joint for robotic gait

rehabilitation training. In *Biomedical robotics and biomechatronics (biorob), 2010 3rd ieee ras and embs international conference on* (pp. 21–26).

Loughlin, C., Albu-Schäffer, A., Haddadin, S., Ott, C., Stemmer, A., Wimböck, T., & Hirzinger, G. (2007). The dlr lightweight robot: design and control concepts for robots in human environments. *Industrial Robot: an international journal*, *34*(5), 376–385.

Lu, J., Haninger, K., Chen, W., & Tomizuka, M. (2015). Design and torque-mode control of a cable-driven rotary series elastic actuator for subject-robot interaction. In *Advanced intelligent mechatronics (aim), 2015 ieee international conference on* (pp. 158–164).

Mathijssen, G., Cherelle, P., Lefeber, D., & Vanderborght, B. (2013). Concept of a series-parallel elastic actuator for a powered transtibial prosthesis. In *Actuators* (Vol. 2, pp. 59–73).

Mehling, J. S., Holley, J., & O'Malley, M. K. (2015). Leveraging disturbance observer based torque control for improved impedance rendering with series elastic actuators. In *Intelligent robots and systems (iros), 2015 ieee/rsj international conference on* (pp. 1646–1651).

Mooney, L., & Herr, H. (2013). Continuously-variable series-elastic actuator. In *Rehabilitation robotics (icorr), 2013 ieee international conference on* (pp. 1–6).

Mosadeghzad, M., Medrano-Cerda, G. A., Saglia, J. A., Tsagarakis, N. G., & Caldwell, D. G. (2012). Comparison of various active impedance control approaches, modeling, implementation, passivity, stability and trade-offs. In *Advanced intelligent mechatronics (aim), 2012 ieee/asme international conference on* (pp. 342–348).

Niiyama, R., Nagakubo, A., & Kuniyoshi, Y. (2007). Mowgli: A bipedal jumping and landing robot with an artificial musculoskeletal system. In *Robotics and automation, 2007 ieee international conference on* (pp. 2546–2551).

Niiyama, R., Nishikawa, S., & Kuniyoshi, Y. (2010). Athlete robot with applied human muscle activation patterns for bipedal running. In *Humanoid robots (humanoids), 2010 10th ieee-ras international conference on* (pp. 498–503).

Okada, M., Ban, S., & Nakamura, Y. (2002). Skill of compliance with controlled charging/discharging of kinetic energy. In *Robotics and automation, 2002. proceedings. icra'02. ieee international conference on* (Vol. 3, pp. 2455–2460).

Ortlieb, A., Olivier, J., Bouri, M., & Bleuler, H. (2016). Series elastic actuation for assistive orthotic devices: Case study of pneumatic actuator. In *New trends in medical and service robots* (pp. 113–125). Springer.

Ott, C. (2008). *Cartesian impedance control of redundant and flexible-joint robots*. Springer.

Özparpucu, M. C., & Albu-Schäffer, A. (2014). Optimal control strategies for maximizing the performance of variable stiffness joints with nonlinear springs. In *Decision and control (cdc), 2014 ieee 53rd annual conference on* (pp. 1409–1416).

Paine, N., Oh, S., & Sentis, L. (2014). Design and control considerations for high-performance series elastic actuators. *IEEE/ASME Transactions on Mechatronics*, *19*(3), 1080–1091.

Paine, N., & Sentis, L. (2015). A closed-form solution for selecting maximum critically damped actuator impedance parameters. *Journal of Dynamic Systems, Measurement, and Control*, *137*(4), 041011.

Paluska, D., & Herr, H. (2006a). The effect of series elasticity on actuator power and work output: Implications for robotic and prosthetic joint design. *Robotics and Autonomous Systems*, *54*(8), 667–673.

Paluska, D., & Herr, H. (2006b). Series elasticity and actuator power output. In *Proceedings 2006 ieee international conference on robotics and automation, 2006. icra 2006.* (pp. 1830–1833).

Parmiggiani, A., Metta, G., & Tsagarakis, N. (2012). The mechatronic design of the new legs of the icub robot. In *Humanoid robots (humanoids), 2012 12th ieee-ras international conference on* (pp. 481–486).

Petit, F., & Albu-Schäffer, A. (2011). State feedback damping control for a multi dof variable stiffness robot arm. In *Robotics and automation (icra), 2011 ieee international conference on* (pp. 5561–5567).

Pott, P. P., Graefenstein, H., Fischer, J., Mueller, R., Schlaak, H. F., & Abele, E. (2013). Series elastic actuators for man-machine cooperation. In *Innovative small drives and micro-motor systems, 2013. 9. gmm/etg symposium* (pp. 1–5).

Pratt, G. A., & Williamson, M. M. (1995). Series elastic actuators. In *Intelligent robots and systems 95.'human robot interaction and cooperative robots', proceedings. 1995 ieee/rsj international conference on* (Vol. 1, pp. 399–406).

Pratt, G. A., Willisson, P., Bolton, C., & Hofman, A. (2004). Late motor processing in low-impedance robots: Impedance control of series-elastic actuators. In *American control conference, 2004. proceedings of the 2004* (Vol. 4, pp. 3245–3251).

Pratt, J., & Pratt, G. (1998). Intuitive control of a planar bipedal walking robot. In *Robotics and automation, 1998. proceedings. 1998 ieee international conference on* (Vol. 3, pp. 2014–2021).

Pratt, J. E., & Krupp, B. T. (2004). Series elastic actuators for legged robots. In *Defense and security* (pp. 135–144).

Quigley, M., Asbeck, A., & Ng, A. (2011). A low-cost compliant 7-dof robotic manipulator. In *Robotics and automation (icra), 2011 ieee international conference on* (pp. 6051–6058).

Ragonesi, D., Agrawal, S., Sample, W., & Rahman, T. (2011). Series elastic actuator control of a powered exoskeleton. In *Engineering in medicine and biology society, embc, 2011 annual international conference of the ieee* (pp. 3515–3518).

Raibert, M., Blankespoor, K., Nelson, G., Playter, R., & Team, T. B. (2008). Bigdog, the rough-terrain quadruped robot. In *Proceedings of the 17th world congress* (Vol. 17, pp. 10822–10825).

Raibert, M. H., & Craig, J. J. (1981). Hybrid position/force control of manipulators. *Journal of Dynamic Systems, Measurement, and Control*, *102*(127), 126–133.

Roberts, T. J. (2002). The integrated function of muscles and tendons during locomotion. *Comparative Biochemistry and Physiology Part A: Molecular & Integrative Physiology*, *133*(4), 1087–1099.

Rouse, E. J., Mooney, L. M., & Herr, H. M. (2014). Clutchable series-elastic actuator: Implications for prosthetic knee design. *The International Journal of Robotics Research*, *33*(13), 1611-1625.

Sariyildiz, E., Yu, H., Nozaki, T., & Murakami, T. (2016). Robust force control of series elastic actuators using sliding mode control and disturbance

observer. In *Industrial electronics society, iecon 2016-42nd annual conference of the ieee* (pp. 619–624).

Semini, C., Tsagarakis, N. G., Guglielmino, E., & Caldwell, D. G. (2010). Design and experimental evaluation of the hydraulically actuated prototype leg of the hyq robot. In *Intelligent robots and systems (iros), 2010 ieee/rsj international conference on* (pp. 3640–3645).

Semini, C., Tsagarakis, N. G., Guglielmino, E., Focchi, M., Cannella, F., & Caldwell, D. G. (2011). Design of hyq–a hydraulically and electrically actuated quadruped robot. *Proceedings of the Institution of Mechanical Engineers, Part I: Journal of Systems and Control Engineering*, *225*(6), 831–849.

Sensinger, J. W., Burkart, L. E., Pratt, G. A., et al. (2013). Effect of compliance location in series elastic actuators. *Robotica*, *31*(08), 1313–1318.

Sensinger, J. W., et al. (2006). Unconstrained impedance control using a compact series elastic actuator. In *Mechatronic and embedded systems and applications, proceedings of the 2nd ieee/asme international conference on* (pp. 1–6).

Sensinger, J. W., & Weir, R. F. F. (2006, Aug). Improvements to series elastic actuators. In *2006 2nd ieee/asme international conference on mechatronics and embedded systems and applications* (p. 1-7).

Sergi, F., Accoto, D., Carpino, G., Tagliamonte, N. L., & Guglielmelli, E. (2012). Design and characterization of a compact rotary series elastic actuator for knee assistance during overground walking. In *Biomedical robotics and biomechatronics (biorob), 2012 4th ieee ras & embs international conference on* (pp. 1931–1936).

Slovich, M., Paine, N., Kemper, K., Metzger, A., Edsinger, A., Weber, J., & Sentis, L. (2012). Hume: A bipedal robot for human-centered hyper-agility. In *Dynamic walking conference.*

Taylor, M. D. (2011). *A compact series elastic actuator for bipedal robots with human-like dynamic performance* (Master's Thesis). Citeseer.

Thomas, G. C., & Sentis, L. (2017, May). Mimo identification of frequency-domain unreliability in seas. In *(to appear in) 2017 american control conference (acc).*

Thorson, I., & Caldwell, D. (2011). A nonlinear series elastic actuator for highly dynamic motions. In *Intelligent robots and systems (iros), 2011 ieee/rsj international conference on* (pp. 390–394).

Tonietti, G., Schiavi, R., & Bicchi, A. (2005). Design and control of a variable stiffness actuator for safe and fast physical human/robot interaction. In *Robotics and automation, 2005. icra 2005. proceedings of the 2005 ieee international conference on* (pp. 526–531).

Torres-Jara, E., & Banks, J. (2005). *A simple and scalable force actuator* (Tech. Rep.). DTIC Document.

Tsagarakis, N. G., Laffranchi, M., Vanderborght, B., & Caldwell, D. G. (2009). A compact soft actuator unit for small scale human friendly robots. In *Robotics and automation, 2009. icra'09. ieee international conference on* (pp. 4356–4362).

Vallery, H., Ekkelenkamp, R., Van Der Kooij, H., & Buss, M. (2007). Passive and accurate torque control of series elastic actuators. In *Intelligent robots and systems, 2007. iros 2007. ieee/rsj international conference on* (pp. 3534–3538).

Van Ham, R., Vanderborght, B., Van Damme, M., Verrelst, B., & Lefeber, D. (2007). Maccepa, the mechanically adjustable compliance and controllable equilibrium position actuator: Design and implementation in a biped robot. *Robotics and Autonomous Systems*, *55*(10), 761–768.

Veneman, J. F., Ekkelenkamp, R., Kruidhof, R., van der Helm, F. C., & van der Kooij, H. (2006). A series elastic-and bowden-cable-based actuation system for use as torque actuator in exoskeleton-type robots. *The international journal of robotics research*, *25*(3), 261–281.

Wakefield, J. (2016, May). Foxconn replaces '60,000 factory workers with robots'. *BBC News*. Retrieved 2016-11-04, from `http://www.bbc.com/news/technology-36376966`

Wang, M., Sun, L., Yin, W., Dong, S., & Liu, J. (2015). A novel sliding mode control for series elastic actuator torque tracking with an extended disturbance observer. In *Robotics and biomimetics (robio), 2015 ieee international conference on* (pp. 2407–2412).

Wilson, A. M., Watson, J. C., & Lichtwark, G. A. (2003). Biomechanics: a catapult action for rapid limb protraction. *Nature*, *421*(6918), 35–36.

Wolf, S., & Hirzinger, G. (2008). A new variable stiffness design: Matching requirements of the next robot generation. In *Robotics and automation, 2008. icra 2008. ieee international conference on* (pp. 1741–1746).

Wyeth, G. (2008). Demonstrating the safety and performance of a velocity sourced series elastic actuator. In *Robotics and automation, 2008. icra 2008. ieee international conference on* (pp. 3642–3647).

Zhao, Y., Paine, N., & Sentis, L. (2014). Feedback parameter selection for impedance control of series elastic actuators. In *Humanoid robots (humanoids), 2014 14th ieee-ras international conference on* (pp. 999–1006).

Zheng, H., Wu, M., & Shen, X. (2016). Pneumatic variable series elastic actuator. *Journal of Dynamic Systems, Measurement, and Control*, *138*(8), 081011.

Zhu, J., Wang, Q., & Wang, L. (2010). Pantoe 1: Biomechanical design of powered ankle-foot prosthesis with compliant joints and segmented foot.

In *Advanced intelligent mechatronics (aim), 2010 ieee/asme international conference on* (pp. 31–36).

Ziegler, J. G., & Nichols, N. B. (1942). Optimum settings for automatic controllers. *trans. ASME*, *64*(11).

Zinn, M., Roth, B., Khatib, O., & Salisbury, J. K. (2004). A new actuation approach for human friendly robot design. *The international journal of robotics research*, *23*(4-5), 379–398.

# Vita

Kenan Isik received his Bachelor of Engineering (B.E.) degrees in Mechatronics Engineering from Hochschule Bochum, Germany and Kocaeli University, Turkey in 2007 and 2008, respectively. He received his Master of Science (M.S.) degree in Mechanical Engineering from Carnegie Mellon University in 2011. Since then, he has been pursuing his PhD degree at The Human Centered Robotics Laboratory in the Mechanical Engineering Department at The University of Texas at Austin, Texas, USA. Upon graduating with a doctoral degree, he plans to pursue his research as a faculty in Karabuk University in Turkey.

Contact Email: kisik@utexas.edu

This dissertation was typeset with LaTeX 2$_\varepsilon$[1] by the author.

[1] LaTeX 2$_\varepsilon$ is an extension of LaTeX. LaTeX is a collection of macros for TeX. TeX is a trademark of the American Mathematical Society. The macros used in formatting this dissertation were written by Dinesh Das, Department of Computer Sciences, The University of Texas at Austin, and extended by Bert Kay, James A. Bednar, and Ayman El-Khashab.